Numerical Modeling of Nonlinear Problems in Hydraulic Fracturing: Fracture Propagation, Proppant Transport, and Shear Dilation

by

Endrina Rivas

A thesis
presented to the University of Waterloo
in fulfillment of the
thesis requirement for the degree of
Doctor of Philosophy
in
Civil Engineering

Waterloo, Ontario, Canada, 2020

Examining Committee Membership

The following served on the Examining Committee for this thesis. The decision of the Examining Committee is by majority vote.

External Examiner:	Dr. C. Armando Duarte Professor, Dept. of Civil and Environmental Engineering, University of Illinois at Urbana-Champaign
Supervisor:	Dr. Robert Gracie Associate Professor, Dept. of Civil and Environmental Engineering, University of Waterloo
Internal-External Member:	Dr. Maurice B. Dusseault Professor, Dept. of Earth and Environmental Sciences, University of Waterloo
Internal Member:	Dr. Dipanjan Basu Associate Professor, Dept. of Civil and Environmental Engineering, University of Waterloo
Internal Member:	Dr. James R. Craig Associate Professor, Dept. of Civil and Environmental Engineering, University of Waterloo

Author's Declaration

This thesis consists of material all of which I authored or co-authored: see Statement of Contributions included in the thesis. This is a true copy of the thesis, including any required final revisions, as accepted by my examiners.

I understand that my thesis may be made electronically available to the public.

Statement of Contributions

This thesis consists in part of three manuscripts written for publication. Exceptions to sole authorship of material are as follows:

Sections 1.2, 2, and 5.1 are based on the following journal article:

Rivas, E. *et al.*, A two-dimensional extended finite element method model of discrete fracture networks, *International Journal for Numerical Methods in Engineering*, vol. 117, no. 13, pp. 1263–1282, 2019

In this journal article, I was the first author and was responsible for the writing of the article; the paper was edited by Dr. Robert Gracie. The computer code for simulating a single hydraulic fracture with the extended finite element method was created by Dr. Matin Parchei-Esfahani. I developed the mathematical formulation and implemented the computer code for simulation of multiple fractures and shear-dilation. This chapter addresses objective 1 of the thesis.

Sections 1.3, 3, and 5.1 are based on the following journal article:

Rivas, E. and Gracie, R., Numerical considerations for the simulation of proppant transport through fractures, *Journal of Petroleum Science and Engineering*, 2019

In this journal article, I was the first author and was responsible for the writing of the article; the paper was edited by Dr. Robert Gracie. I developed the mathematical formulation, implemented the computer code, and ran the simulations. This chapter addresses the second objective of the thesis.

Sections 1.4, 4, and 5.1 are based on the following journal article:

Rivas, E. and Gracie, R., A monolithic coupled hydraulic fracture model with proppant transport, *Manuscript submitted for publication*, 2020

In this journal article, I was the first author and was responsible for the writing of the article; the paper was edited by Dr. Robert Gracie. I developed the mathematical formulation, implemented the computer code for the coupled system of equations, and ran the simulations. The computer code for fracture propagation is based on the work of Dr. Matin Parchei-Esfahani. This chapter addresses the last objective of the thesis.

Abstract

Hydraulic fracturing is a stimulation technique in which fluid is injected at high pressure into low-permeability reservoirs to create a fracture network for enhanced production of oil and gas. It is the primary purpose of hydraulic fracturing to enhance well production. The three main mechanisms during hydraulic fracturing for oil and gas production which largely impact the reservoir production are: (1) fracture propagation during initial pad fluid injection, which defines the extent of the fracture; (2) fracture propagation during injection of proppant slurry (fluid mixed with granular material), creating a propped reservoir zone; and (3) shear dilation of natural fractures surrounding the hydraulically fractured zone, creating a broader stimulated zone. The thesis has three objectives that support the simulation of mechanisms that lead to enhanced production of a hydraulically-fractured reservoir.

The first objective is to develop a numerical model for the simulation of the mechanical deformation and shear dilation of naturally fractured rock masses. In this work, a two-dimensional model for the simulation of discrete fracture networks (DFN) is developed using the extended finite element method (XFEM), in which the mesh does not conform to the natural fracture network. The model incorporates contact, cohesion, and friction between blocks of rock. Shear dilation is an important mechanism impacting the overall nonlinear response of naturally fractured rock masses and is also included in the model—physics previously not simulated within an XFEM context. Here, shear dilation is modeled through a linear dilation model, capped by a dilation limiting displacement. Highly nonlinear problems involving multiple joint sets are investigated within a quasi-static context. An explicit scheme is used in conjunction with the dynamic relaxation technique to obtain equilibrium solutions in the face of the nonlinear constitutive models from contact, cohesion, friction, and dilation. The numerical implementation is verified and its convergence illustrated using a shear test and a biaxial test. The model is then applied to the practical problem of the stability of a slope of fractured rock.

The second objective is to develop a numerical model for the simulation of proppant transport through planar fractures. This work presents the numerical methodology for simulation of proppant transport through a hydraulic fracture using the finite volume method. Proppant models commonly used in the hydraulic fracturing literature solve the linearized advection equation; this work presents solution methods for the nonlinear form of the proppant flux equation. The complexities of solving the nonlinear and heterogeneous hyperbolic advection equation that governs proppant transport are tackled, particularly handling shock waves that are generated due to the nonlinear flux function and the spatially-varying width and pressure gradient along the fracture. A critical time step is derived for the proppant transport problem solved using an explicit solution strategy. Additionally, a predictor-corrector algorithm is developed to constrain the proppant from exceeding the physically admissible range. The model can capture the mechanisms of proppant bridging occurring in sections of narrow fracture width, tip screen-out occurring when fractures become saturated with proppant, and flushing of proppant into new fracture segments.

The results are verified by comparison with characteristic solutions and the model is used to simulate proppant transport through a KGD fracture.

The final objective is to develop a numerical model for the simulation of proppant transport through propagating non-planar fractures. This work presents the first monolithic coupled numerical model for simulating proppant transport through a propagating hydraulic fracture. A fracture is propagated through a two-dimensional domain, driven by the flow of a proppant-laden slurry. Modeling of the slurry flow includes the effects of proppant bridging and the subsequent flow of fracturing fluid through the packed proppant pack. This allows for the simulation of a tip screen-out, a phenomenon in which there is a high degree of physical interaction between the rock deformation, fluid flow, and proppant transport. Tip screen-out also leads to shock wave formation in the solution.

Numerical implementation of the model is verified and the model is then used to simulate a tip screen-out in both planar and non-planar fractures. An analysis of the fracture aperture, fluid pressure, and proppant concentration profiles throughout the simulation is performed for three different coupling schemes: monolithic, sequential, and loose coupling. It is demonstrated that even with time step refinement, the loosely-coupled scheme fails to converge to the same results as the monolithic and sequential schemes. The monolithic and sequential algorithms yield the same solution up to the onset of a tip screen-out, after which the sequential scheme fails to converge. The monolithic scheme is shown to be more efficient than the sequential algorithm (requiring fewer iterations) and has comparable computational cost to the loose coupling algorithm. Thus, the monolithic scheme is shown to be optimal in terms of computational efficiency, robustness, and accuracy. In addition to this finding, a robust and more efficient algorithm for injection-rate controlled hydraulic fracturing simulation based on global mass conservation is presented in the thesis.

Acknowledgements

This thesis could not have been possible without the support of many individuals along the way. First, I express my appreciation to the committee members for reviewing my work and providing an interesting discussion.

I am deeply grateful to Dr. Robert Gracie for his motivation and continued support throughout this research. He has provided me with technical insight throughout my studies, the freedom to explore my academic interests, and opportunities to meet other researchers in my field. This thesis is greatly enhanced by his explanation of an Oxford comma.

I extend my sincere thanks to Dr. Thomas-Peter Fries and the members of his institute, who hosted me at TU Graz. I also thank my fellow members of the Computational Mechanics research group. While the work of writing a thesis can be quite solitary, discussions about research and support during the tedious debugging process have kept me sane. I am grateful to Eleanor Mak and Mike Yetisir for their company in (and out of) the office.

To all the friends who laughed with me, explored the world with me, gave me a place to crash, pushed me to be a better squash player, and generally distracted me from the day-to-day grind of research, I cannot thank you enough. A special mention goes to Laura Thacker, Vova Golubin, and the Thacker family, who have been a tremendous support throughout my studies. I am also grateful to Theo Ortega, whom I can always count on to help me "figure it out".

Finally, I thank my family, who has kept me grounded throughout my graduate studies. During the ups and downs of research, I've been uplifted witnessing Nia's perceptiveness, Beto's spirit, Ñaño's playfulness and wisdom, Dad's unrelenting love of life, and Mom's contagious laughter. Seeing each of them face and overcome their challenges has been one of the biggest motivators throughout the making of this thesis. I strived to complete my studies so that they are equally as motivated to pursue their own goals (and to give them some bragging rights when I become a Doctor).

Thank you all

Table of Contents

List of Tables **xii**

List of Figures **xiii**

List of Symbols **xvii**

List of Symbols in Chapter 2 xvii

List of Symbols in Chapter 3 xx

List of Symbols in Chapter 4 xxii

1 Introduction **1**

1.1 Introduction to hydraulic fracturing simulations 1

1.2 Shear dilation 4

1.3 Proppant transport 6

1.4 Coupled problems 8

1.5 Motivations 9

1.6 Research objectives and methodologies 10

1.6.1 Objective 1: Develop a numerical model for the simulation of the mechanical deformation and shear dilation of naturally fractured rock masses 10

1.6.2 Objective 2: Develop a numerical model for the simulation of proppant transport through planar fractures 10

1.6.3 Objective 3: Develop a numerical model for the simulation of proppant transport through propagating non-planar fractures 11

2 A two-dimensional extended finite element method model of discrete fracture networks 12

2.1 Introduction . . . 12
2.2 Governing equations . . . 13
2.3 Interface constitutive models . . . 15
2.3.1 Contact and cohesive forces . . . 15
2.3.2 Friction . . . 17
2.3.3 Shear dilation . . . 18
2.4 XFEM discretization . . . 19
2.4.1 Explicit and implicit definition of fracture network . . . 20
2.4.2 Approximation . . . 21
2.4.3 Identification of enriched nodes . . . 23
2.4.4 Enrichment function . . . 24
2.4.5 Discretization . . . 25
2.5 Solution method . . . 26
2.5.1 Dynamic relaxation scheme . . . 27
2.6 Numerical results . . . 29
2.6.1 Shear test . . . 29
2.6.2 Biaxial test of a rock mass with a DFN . . . 32
2.6.3 Stability of a rock slope containing a DFN . . . 35

3 Numerical considerations for the simulation of proppant transport through fractures 40

3.1 Introduction . . . 40
3.2 Governing equations . . . 41
3.2.1 Slurry equations . . . 41
3.2.2 Proppant equation . . . 43
3.2.3 Flux functions . . . 44
3.2.4 Initial and boundary conditions . . . 46
3.3 Finite volume discretization . . . 47

3.3.1 Characteristic speed of proppant . . . 48
3.3.2 Critical time step for proppant transport . . . 51
3.3.3 Shock waves in proppant transport problems . . . 52
3.3.4 Approximation of proppant fluxes . . . 55
Godunov method . . . 55
Lax-Wendroff method . . . 56
High resolution method . . . 57
3.3.5 Boundary conditions . . . 58
3.3.6 Proppant concentration constraints . . . 59
3.4 Numerical results . . . 61
3.4.1 Injection and growth of propped fractures . . . 61
3.4.2 Plug formation and growth . . . 62
3.4.3 Inject into an elliptical fracture with constant pressure gradient . . . 64
3.4.4 Injection into KGD fracture . . . 67

4 A monolithic coupled hydraulic fracture model with proppant transport 72
4.1 Introduction . . . 72
4.2 Governing equations . . . 73
4.2.1 Governing equations for the deformation of solid rock mass . . . 74
Interface constitutive model . . . 76
4.2.2 Governing equations for the flow of proppant-laden slurry . . . 78
Constitutive model of slurry flow . . . 80
4.3 Numerical methodology . . . 83
4.3.1 Discretization . . . 83
4.3.2 XFEM approximation of the rock deformation . . . 84
4.3.3 FEM approximation of the fluid flow . . . 86
4.3.4 FVM approximation of proppant transport . . . 86
Concentration constraints . . . 88
4.3.5 Coupled system of equations . . . 88

4.4 Solution strategies . . . 89
4.4.1 Coupled solution algorithm (inner loop) . . . 91
Monolithic coupling . . . 91
Sequential and loose coupling . . . 93
4.4.2 Injection rate-controlled boundary: Global mass conservation (outer loop) 94
New iterative method for injection control . . . 96
4.4.3 Fracture propagation . . . 98
4.4.4 Adaptive time steps . . . 99
4.5 Numerical results . . . 100
4.5.1 Slurry flow through a pre-defined fracture . . . 101
4.5.2 Comparison of coupling schemes during tip screen-out . . . 102
4.5.3 Non-planar fracture propagation . . . 106
Verification of non-planar fracture propagation . . . 107
Slurry flow through non-planar fracture . . . 109
4.6 Discussion . . . 113

5 Conclusions **115**
5.1 Concluding remarks . . . 115
5.2 Significant contributions . . . 117
5.3 Directions for future study . . . 119

References **121**

Appendices **132**

A Verification of planar fracture propagation **133**
A.1 Toughness-dominated planar fracture propagation . . . 134
A.2 Viscosity-dominated planar fracture propagation . . . 135
A.3 Slurry-driven planar fracture propagation . . . 135

List of Tables

2.1 Material properties for simulations of discrete fracture networks 29

3.1 Expressions of effective viscosity as a function of proppant concentration, $\mu(\phi)$. 45
3.2 Stagnation point for various effective viscosity functions 50
3.3 Material properties for simulations of proppant transport through planar fractures 61
3.4 Injection rate used to maintain injection concentration of $\phi_{inj} = 0.1$ for various expressions of effective viscosity 66

4.1 Material properties for simulations of proppant transport in propagating fractures 100

A.1 Material properties for planar fracture propagation simulations 133

List of Figures

1.1 Fracture network stimulation 2
1.2 Shear dilation of a rough joint 5

2.1 Domain of fractured rock mass 13
2.2 Constitutive law for normal tractions on fracture surface 17
2.3 Constitutive law for tangential tractions on fracture surface 18
2.4 Linear dilation constitutive model 19
2.5 Enriched nodes on XFEM mesh with multiple fractures 20
2.6 Global crack separation 21
2.7 Erroneous detection of enriched element with criteria based on level-set functions 23
2.8 Enrichment functions for an element with intersecting fractures 25
2.9 Schematic of shear test specimen and horizontal displacement contour on deformed mesh 30
2.10 Shear stress and dilation along crack throughout shear test 31
2.11 Critical shear stress vs. normal stress for shear test specimen 31
2.12 Schematic of biaxial test on jointed rock specimen and horizontal displacement contour on structured mesh 32
2.13 Slip along fractures at various loading stages of a rock mass with a DFN 33
2.14 Shear dilation along fractures at various loading stages of a rock mass with a DFN 34
2.15 Differential stress vs vertical strain of the fractured rock specimen during biaxial loading for various mesh sizes 35
2.16 Horizontal displacement contours for various mesh sizes during a biaxial test . . 36
2.17 Schematic of loading on fractured rock slope and vertical displacement contours on deformed unstructured mesh 37

2.18 Stress contours on rock slope under gravitational loading and just before failure . 38
2.19 Contours of slip and dilation along fractures of the slope just before failure 39

3.1 Domain of interest for a proppant transport model along a horizontal plane of a vertical fracture 41
3.2 Proppant flux over a range of normalized proppant concentrations 46
3.3 Finite Volume mesh for discretization of proppant advection 47
3.4 Variation in the approximate characteristic speed over a range of normalized proppant concentrations 49
3.5 Visualization of characteristic curves during the formation of shock waves propagating due to discontinuity in the solution at a cell edge 53
3.6 Visualization of characteristic curves during formation of compression and rarefaction waves 54
3.7 Corrected cell edge fluxes for cells in set S^+ 60
3.8 Corrected cell edge fluxes for cells in set S^- 60
3.9 Proppant concentration spreading at the fracture inlet over time 63
3.10 Theoretical characteristic speed patterns for rarefaction waves 64
3.11 Proppant concentration backing up at a plug over time 65
3.12 Theoretical characteristic speed patterns for compression waves 66
3.13 Proppant injection into an elliptical fracture with constant pressure gradient over time 68
3.14 Width and pressure along the length of a KGD fracture 69
3.15 Proppant injection into a KGD fracture over time 70
3.16 Proppant concentration at $t = 1800$ s using various effective viscosity formulas with and without concentration constraints 71

4.1 Two-dimensional domain of interest for a model of a hydraulic fracture driven by a proppant-laden slurry 74
4.2 Solid rock mass domain 75
4.3 Traction-separation law 77
4.4 Slurry domain 78
4.5 Fluid flux for varying fracture apertures as a function of proppant concentration . 82

4.6 Proppant flux for varying fracture apertures as a function of proppant concentration 83
4.7 Discretized rock, fluid, and proppant domains 84
4.8 Finite volume cells 87
4.9 Solution algorithm flowchart 90
4.10 Stored data points for slope estimate 97
4.11 Cohesive zone model and fracture propagation criterion 99
4.12 Schematic and mesh for a model of slurry flow through a pre-defined fracture . . 101
4.13 Proppant concentration, fluid pressure, and fracture aperture for a planar, slurry-driven fracture over time 103
4.14 Proppant concentration, fluid pressure, and fracture aperture for a planar, slurry-driven fracture undergoing a tip screen-out at various times 105
4.15 Proppant concentration along half of the fracture length over time for the loose coupling scheme 106
4.16 Schematic and mesh used to simulate slurry-driven non-planar fracture propagation from a wellbore 107
4.17 Fracture propagation resulting from an initial fracture of 2 cm length oriented at varying angles from the horizontal 108
4.18 Wellbore aperture, wellbore pressure, and fracture length over time for fractures with varying initial orientations 109
4.19 Proppant concentration, fluid pressure, and fracture aperture for a non-planar slurry-driven fracture over time 110
4.20 Maximum proppant concentration and proppant front location over time 111
4.21 Wellbore aperture, wellbore pressure, and fracture length over time for a fracture initially oriented 20° from the horizontal 112
4.22 Time step size over simulation time 113
4.23 Number of Jacobian calculations 114

A.1 Schematic of domain for model of planar fracture propagation 134
A.2 Wellbore aperture, wellbore pressure, and fracture half-length over time for a fracture propagating in the toughness-dominated regime 135
A.3 Wellbore aperture, wellbore pressure, and fracture half-length over time for a fracture propagating in the viscosity-dominated regime 136

A.4 Proppant concentration of injected slurry over time 136
A.5 Proppant concentration along the fracture over time 137
A.6 Wellbore aperture, wellbore pressure, and fracture half-length for planar fracture propagation driven by a proppant-laden slurry 138

List of Symbols in Chapter 2

Greek

Γ	Boundary of the two-dimensional domain
Γ_c	Internal boundary of the domain along the surface of fracture name c
Γ_c^-	Internal boundary of the domain along the negative face of fracture c
Γ_c^+	Internal boundary of the domain along the positive face of fracture c
Γ_t	Neumann boundary
Γ_u	Dirichlet boundary
Δt	Time step size
$\Delta \bar{t}_y$	External load increment applied to top of the rock slope
$\delta \mathbf{u}(\mathbf{x})$	Test function
ϵ_r	Threshold value for determining convergence of the system with a residual-based criterion
ϵ_u	Threshold value for determining convergence of the system with a displacement-based criterion
$\boldsymbol{\varepsilon}$	Infinitesimal strain
$\boldsymbol{\varepsilon}^h(\mathbf{x}, t)$	Approximation of the strain field
$\varepsilon_x, \varepsilon_y, \varepsilon_{xy}$	Components of strain in Cartesian coordinates: horizontal strain, vertical strain, and shear strain
ν	Poisson's ratio
ρ	Rock density
$\boldsymbol{\sigma}$	Cauchy stress tensor
σ_1, σ_3	Principal stresses
$\sigma_{11}, \sigma_{22}, \sigma_{12}$	Components of stress: two normal components and a shear component
$\sigma_x, \sigma_y, \sigma_{xy}$	Components of stress in Cartesian coordinates: horizontal stress, vertical stress, and shear stress
$\boldsymbol{\sigma}^-$	Stress on the negative face of a fracture
$\boldsymbol{\sigma}^+$	Stress on the positive face of a fracture
σ_u	Compressive strength of the rock
$\{\boldsymbol{\sigma}\}$	Cauchy stress in Voigt notation
τ_{crit}	Shear strength of the rock
ϕ	Angle of friction of the natural fractures
$\phi_c(\mathbf{x})$	Level set function defining the normal signed distance between a location $\mathbf{x}$ and the tip of the fracture, $\mathbf{x}_{\Gamma_c}^{tip}$
φ	Dilation angle
$\psi_c(\mathbf{x})$	Level set function defining the tangential signed distance between a location $\mathbf{x}$ and the tip of the fracture, $\mathbf{x}_{\Gamma_c}^{tip}$

$\Psi_I^c(\mathbf{x})$	Enrichment function for node I in the set S_c
Ω	Domain of the naturally fractured rock mass
ω_{max}	Highest natural frequency of the system
ω_{min}	Minimum natural frequency of the system
∇	Differential operator
∇^s	Differential operator for the strain definition defined as $\frac{1}{2}(\nabla + \nabla^\top)$

Latin

$\hat{\mathbf{a}}(t)$	Column matrix of displacements on the enriched degrees of freedom for all fractures
$\tilde{\mathbf{a}}_I^c(t)$	Vector of nodal displacements on the enriched degrees of freedom of node I in the set S_c
$\mathbf{b}(\mathbf{x})$	Body forces
$\mathbf{B}(\mathbf{x})$	Matrix of shape function derivatives for both standard and enriched degrees of freedom
$\mathbf{B}_a(\mathbf{x})$	Matrix of shape function derivatives corresponding to the enriched degrees of freedom for all fractures
$\mathbf{B}_u(\mathbf{x})$	Matrix of shape function derivatives corresponding to the standard degrees of freedom
c	Damping parameter
$\mathbf{C}$	Damping matrix
c_f	Shear strength of the rock due to cohesion
$\mathbf{D}$	Two-dimensional plane-strain elasticity matrix
$\mathbf{d}(t)$	Column matrix of displacements on all degrees of freedom
$\dot{\mathbf{d}}(t)$	Column matrix of velocities on all degrees of freedom
$\ddot{\mathbf{d}}(t)$	Column matrix of accelerations on all degrees of freedom
E	Young's modulus
$\hat{\mathbf{e}}_{\Gamma_c}(\mathbf{x})$	Tangential vector to the internal boundary along the surface of fracture c
$\mathbf{F}^{damp}$	Column matrix of damping forces
$\mathbf{F}^{ext}$	Column matrix of external forces
$\mathbf{F}^{int}$	Column matrix of internal forces
$\mathbf{F}^{kin}$	Column matrix of kinetic forces
$\mathbf{F}^c$	Column matrix of forces along the fractures
f_u	Yield strength of the rock
G_{Ic}	Mode I fracture energy
H^1	Space of functions with square integral derivatives
$H_c(\mathbf{x})$	Heaviside step function that differentiates between the two sides of fracture c
$J_c(\mathbf{x})$	Junction enrichment function for fracture c

K	Ratio of horizontal and vertical stresses
k_1	Positive slope of the traction separation curve in opening state
k_2	Negative slope of the traction separation curve in opening state
$\mathbf{K}$	Stiffness matrix
$\bar{\mathbf{K}}$	Stiffness matrix approximation
k_n	Contact stiffness
k_t	Frictional stiffness
L_c	Fracture length
$\mathbf{M}$	Mass matrix
$\mathbf{N}(\mathbf{x})$	Matrix of shape functions for both the standard and enriched degrees of freedom
$\mathbf{N}_a(\mathbf{x})$	Matrix of shape functions corresponding to the enriched degrees of freedom for all fractures
$\mathbf{N}_u(\mathbf{x})$	Matrix of shape functions corresponding to the standard degrees of freedom
$\hat{\mathbf{n}}(\mathbf{x})$	Normal vector to the external boundary of the domain
$\hat{\mathbf{n}}_{\Gamma_c}(\mathbf{x})$	Normal vector to the internal boundary, defined as the outward normal vector to the negative face of fracture c
$\hat{\mathbf{n}}^-_{\Gamma_c}(\mathbf{x})$	Outward normal vector to the negative face of fracture c
$\hat{\mathbf{n}}^+_{\Gamma_c}(\mathbf{x})$	Outward normal vector to the positive face of fracture c
$N_I(\mathbf{x})$	Standard finite element shape functions for node I
$\mathbf{r}$	Residual of the quasi-static system defined as the sum of the transient terms
S_c	Set of fractures in the domain
S_m	Set of all main fractures in the domain
S_{mc}	Set of main fractures that cut secondary fracture c
S_n	Set of all nodes in each element
S_{nc}	Set of nodes that have a nodal support cut by fracture c
S_s	Set of all secondary fractures in the domain
t	Time
$\bar{t}^{coh}$	Magnitude of cohesive forces
$\bar{t}^{con}$	Magnitude of contact forces
$\bar{t}^{fric}$	Magnitude of friction forces
$\bar{t}_y$	External load applied to the top surface of the rock specimen during shear test
$\bar{\mathbf{t}}$	External traction
$\bar{\mathbf{t}}_c$	Traction acting on the surface of fracture c
$\bar{\mathbf{t}}_{cn}$	Traction acting normal to the surface of fracture c
$\bar{\mathbf{t}}_{ct}$	Traction acting tangential to the surface of fracture c
U	Space of admissible solutions
U_0	Space of admissible test functions
$\mathbf{u}(\mathbf{x}, t)$	Displacement

$\mathbf{u}_0(\mathbf{x})$	Initial displacement
$\bar{\mathbf{u}}(\mathbf{x}, t)$	Prescribed displacement
$\dot{\mathbf{u}}\,(\mathbf{x}, t)$	Velocity
$\dot{\mathbf{u}}_0(\mathbf{x})$	Initial velocity
$\ddot{\mathbf{u}}\,(\mathbf{x}, t)$	Acceleration
$\mathbf{u}^h(\mathbf{x}, t)$	Approximation of the displacement field
$\hat{\mathbf{u}}(t)$	Column matrix of displacements on the standard degrees of freedom
$[\![\mathbf{u}(\mathbf{x})]\!]$	Jump in displacement
$\mathbf{u}(\mathbf{x}^-)$	Displacement on the negative face of a fracture
$\mathbf{u}(\mathbf{x}^+)$	Displacement on the positive face of a fracture
$\tilde{\mathbf{u}}_I(t)$	Vector of nodal displacements on the standard degrees of freedom of node I
u_x, u_y	Displacement components: horizontal displacement and vertical displacement
u_n	Fracture aperture, or normal jump in displacement at the fracture surface
u_n^d	Dilation
u_n^{max}	Fracture aperture corresponding to the maximum cohesive forces
u_n^{sep}	Fracture aperture at which the fracture is fully separated
u_t	Tangential jump in displacement at the fracture surface
u_t^{crit}	Critical shear displacement at which the dilation growth is capped
u_t^{peak}	Shear displacement at which fracture surface undergoes shear yielding
$\mathbf{x}$	Spatial coordinate
$\mathbf{x}_c$	Arbitrary point along the secondary fracture c
$\mathbf{x}_{\Gamma_c}^{tip}$	Location of the fracture tip

Superscripts

n	Pertaining to the start of time step n
$n+1$	Pertaining to the end of time step n
$n+\frac{1}{2}$	Pertaining to the midpoint between the start and end of time step n

List of Symbols in Chapter 3

Greek

β	Coefficient used in Krieger-Dougherty-type expressions of effective viscosity
$\Delta(\phi w)$	Jump in propped fracture aperture
Δq	Jump in the proppant volumetric flux
Δt	Length of a time step
Δx	Length of evenly-spaced finite volume cells

ϵ_s	Threshold value to determine whether the jump in ϕw is approaching zero
$\mu(\phi)$	Effective slurry viscosity
μ_0	Viscosity of the carrier fluid
ρ	Slurry density
ρ_f	Fluid density
ρ_p	Proppant density
$\varphi(r)$	Limiter function
$\phi_0(x)$	Initial proppant concentration at the start of the simulation
$\phi(x,t)$	Average volumetric concentration of proppant particles across the fracture width
ϕ_{inj}	Volumetric concentration of slurry injected at the wellbore
$\phi_{i,p}^{n+1}$	Predicted concentration for the end of time step t_n at cell i before applying proppant concentration constraints
ϕ_m	Saturated proppant concentration
ϕ_s	Stagnation point–concentration at which the characteristic speed changes sign

Latin

a	Average proppant radius
B, B_1, B_2, B_3	Coefficients used in expressions of effective viscosity
H	Heaviside step function
N	Number of evenly-spaced finite volume cells
p	Fluid pressure
Q	Slurry mass flux per unit height of fracture
q	Proppant volumetric flux per unit height of fracture
$q_{correct}^{-}$	Correction for the approximation of the proppant flux for cells which have a negative proppant concentration
$q_{correct}^{+}$	Correction for the approximation of the proppant flux for cells which have a concentration over the saturation value, ϕ_m
Q_f	Fluid mass flux per unit height of fracture
Q_{inj}	Mass flux of slurry per unit area of fracture injected at the wellbore
Q_p	Proppant mass flux per unit height of fracture
q_s	Proppant volumetric flux corresponding to the stagnation point
Q_{sink}	Mass flux of slurry per unit area of fracture leaking off into the formation
q_{inj}	Volumetric flux of proppant per unit area of fracture injected at the wellbore
r	Slope ratio–ratio of upwind concentration gradient to the gradient at the cell edge
s_R	Shock speed defined using the Rankine Hugoniot jump condition
s	Proppant characteristic speed
S^-	Set of cells with a proppant concentration below the minimum ($\phi = 0$)

S^+	Set of cells with a proppant concentration above the maximum (ϕ_m)
s^n_{max}	Maximum proppant characteristic speed in the domain at time t_n
t	Time
v	Slurry velocity
v_p	Proppant velocity
v^{slip}	Slip velocity–difference in velocity of the proppant and the slurry
$w(x)$	Fracture width
x	Distance along the length of the fracture
x_0	Location of fracture inlet
x_{tip}	Location of fracture tip
y	Distance along the fracture width

Superscripts

c	Corrected approximation using the proppant concentration constraints
G	Pertaining to the Godunov approximation method
LW	Pertaining to the correction term of the Lax-Wendroff method
n	Pertaining to beginning of time step n
$n+1$	Pertaining to the end of time step n

Subscripts

i	Pertaining to the center of cell i
$i \pm 1$	Pertaining to the center of the cells directly adjacent to cell i
$i \pm 1/2$	Pertaining to the edges of cell i

List of Symbols in Chapter 4

Greek

Γ_c	Internal boundary pertaining to the fracture surface on the solid rock mass
Γ_c^-	Negative face of the fracture surface boundary
Γ_c^+	Positive face of the fracture surface boundary
Γ_f	Boundary of the slurry domain
Γ_p	Dirichlet boundary of the slurry domain
Γ_q	Neumann boundary of the slurry domain
Γ_s	Boundary of the solid rock mass
Γ_t	Neumann boundary on the solid rock mass
Γ_u	Dirichlet boundary on the solid rock mass

$\Delta\mathbf{F}^a$	Column matrix of change in proppant flux at the cell edges
δp	Test function multiplied by the conservation of fluid mass to derive weak form
Δs	Length of a finite volume cell
Δt	Time step
Δt_{prop}	Largest time step permissible to meet the CFL stability condition
$\delta\mathbf{u}$	Test function multiplied by the equation of rock equilibrium to derive weak form
$\frac{\partial p}{\partial s}$	Pressure gradient of the slurry along the fracture length
$\epsilon_{tol,a}$	Threshold tolerance for determining convergence of the coupled system based on a residual-based criterion
$\epsilon_{tol,b}$	Threshold tolerance for determining convergence of the coupled system based on a normalized residual-based criterion
$\epsilon_{tol,global}$	Threshold tolerance for determining convergence of the global mass conservation
$\boldsymbol{\varepsilon}$	Infinitesimal strain
$\boldsymbol{\varepsilon}^h(\mathbf{x})$	Approximation of strain in the rock mass
λ	Partial derivative of wellbore pressure with respect to the injection rate
μ_0	Fracturing fluid viscosity
$\mu(\phi)$	Effective slurry viscosity
ν	Poisson's ratio
ρ	Slurry density
ρ_f	Fluid density
ρ_p	Proppant density
$\boldsymbol{\sigma}_0$	Initial stress state in the solid domain
σ_1, σ_3	Principal stresses
$\boldsymbol{\sigma}$	Cauchy stress tensor
σ_H	Maximum horizontal *in-situ* stress
σ_h	Minimum horizontal *in-situ* stress
$\boldsymbol{\sigma}^+, \boldsymbol{\sigma}^-$	Stress on the positive and negative face of a fracture, respectively
σ_v	Vertical *in-situ* stress
θ	Initial fracture orientation with respect to the horizontal direction
ϕ	Average volumetric proppant concentration along the fracture width
$\boldsymbol{\phi}$	Column matrix of proppant concentration at each finite volume cell
ϕ_{inj}	Proppant concentration of the injected slurry
ϕ_m	Fully saturated proppant concentration
$\boldsymbol{\psi}$	Column matrix of independent variables (rock displacements, fluid pressures, and proppant concentrations)
$\Psi_J(\mathbf{x})$	Enrichment function at enriched node J
Ω_c	Domain of the slurry
Ω_s	Domain of the solid rock mass
∇	Differential operator

∇^s	Differential operator for the strain definition defined as $\frac{1}{2}(\nabla + \nabla^\top)$

Latin

a	Average proppant particle radius
$\mathbf{a}$	Nodal displacements on the enriched degrees of freedom for a given element
$\tilde{\mathbf{a}}_J$	Nodal displacements on the enriched degrees of freedom for node J
$B(w)$	Bridging function defined as a Heaviside step function that is positive when the aperture is greater than stipulated number of proppant diameters
$\mathbf{b}$	Body forces applied on the solid domain
$\mathbf{B}(\mathbf{x})$	Vector of derivative of shape functions corresponding to both standard and enriched degrees of freedom
$\mathbf{B}_a$	Vector of derivative of shape functions corresponding to enriched degrees of freedom
$\mathbf{B}_f(\mathrm{s})$	Matrix of shape function derivatives used for approximating the pressure gradient
$\mathbf{B}_u$	Vector of derivative of shape functions corresponding to standard degrees of freedom
c_L	Carter leak-off coefficient
$\mathbf{D}$	two-dimensional plane-strain elasticity matrix
$\mathbf{d}$	Vector of displacements corresponding to both standard and enriched degrees of freedom
E	Young's modulus
F	Set of elements in the fluid domain
$\mathbf{F}^{advect}$	Column matrix of advection fluxes of the propped aperture
$\mathbf{F}^c$	Vector of cohesive forces on the fracture surface
$\mathbf{F}^d$	Vector of diffusive forces in the fluid domain
$\mathbf{F}^{ext}$	Vector of external forces acting on the rock mass
$\mathbf{F}^f$	Vector of applied fluxes on the fluid boundary
$\mathbf{F}^{int}$	Vector of internal forces in the rock mass
$\mathbf{F}^l$	Vector of leak-off fluxes
$\mathbf{F}^p$	Vector of pressure forces on the fracture surface
$\mathbf{F}^{ps}$	Column matrix of proppant storage fluxes
$\mathbf{F}^s$	Vector of forces corresponding to change in fracture storage on the fluid domain
f_u	Material tensile strength
G_{Ic}	Mode I fracture energy
$H(\mathbf{x})$	Heaviside step function that differentiate between the two sides of the fracture
$\mathbf{J}$	Jacobian matrix containing the partial derivatives of the residual components with respect to the independent variables
$\mathbf{J}_{seq}$	Jacobian matrix containing the partial derivatives of the residual components with respect to the independent variables

$\mathbf{K}_c$	Partial derivative of interface forces with respect to rock displacement
$\mathbf{K}_{dd}$	Partial derivative of internal forces with respect to rock displacement
$\mathbf{K}_{dp}$	Partial derivative of pressure forces with respect to fluid pressure
$\mathbf{K}_{pd}$	Partial derivative of diffusive fluxes with respect to rock displacement
$\mathbf{K}_{\phi d}$	Partial derivative of proppant storage fluxes with respect to rock displacement
$\mathbf{K}_{\phi\phi}$	Partial derivative of proppant storage fluxes with respect to proppant concentration
$\mathbf{K}_{pp}$	Partial derivative of diffusive fluxes with respect to fluid pressure
$\mathbf{K}_{p\phi}$	Partial derivative of internal forces with respect to proppant concentration
$\mathbf{K}_{sd}$	Partial derivative of fluid storage fluxes with respect to rock displacement
$\mathbf{K}_{s\phi}$	Partial derivative of fluid storage fluxes with respect to proppant concentration
k_f	Fluid conductivity within the fracture
k_p	Proppant conductivity within the fracture
L	Fracture length
N	Number of finite volume cells
$\mathbf{N}(\mathbf{x})$	Matrix of shape functions corresponding to both standard and enriched degrees of freedom
$\mathbf{N}_a$	Matrix of shape functions corresponding to enriched degrees of freedom
$\mathbf{N}_f(\mathrm{s})$	Matrix of shape functions used for approximating the fluid pressure
$\mathbf{N}_u$	Matrix of shape functions corresponding to standard degrees of freedom
n_{dia}	Number of proppant diameters that define the threshold aperture for bridging
$\hat{\mathbf{n}}$	Outward normal vector to boundary of solid rock mass
$\hat{\mathbf{n}}_{\Gamma_c}$	Inward normal vector to the positive boundary of the fracture surface
$\hat{\mathbf{n}}_{\Gamma_c^+}$	Outward normal vector to the positive boundary of the fracture surface
$\hat{\mathbf{n}}_{\Gamma_c^-}$	Outward normal vector to the negative boundary of the fracture surface
N_I	Standard finite element shape functions for node I
p	Fluid pressure
$\mathbf{p}(t)$	Vector of nodal fluid pressures in each element
$\bar{p}$	Prescribed pressure on the Dirichlet boundary of the fluid domain
$p^h(s,t)$	Approximation of fluid pressure
$p^h_{,s}(s,t)$	Approximation of fluid pressure gradient
p_{lim}	Factor used to limit the change in wellbore pressure within the global mass conservation loop
p_w	Wellbore pressure
q	Volumetric flux of the slurry mixture
$\bar{q}_f$	Prescribed fluid flux on the Neumann boundary of the fluid domain
$\bar{q}_{p0}(s)$	Initial proppant concentration profile at time $t = 0$
q_f	Volumetric fluid flux
Q_{inj}	Volumetric flux of fluid per unit area of fracture injected into fracture
Q_{leak}	Volumetric flux of fluid per unit area of fracture leaking off into the formation

q_p	Volumetric proppant flux
$\tilde{Q}$	Injection rate determined through global mass conservation
$\mathbf{R}$	Column matrix of residuals for the coupled system of equations
$\mathbf{R}_d$	Residual of the governing equation for rock deformation
$\mathbf{R}_p$	Residual of the governing equation for fluid flow at time t^n
$\mathbf{R}_\phi$	Residual of the governing equation for proppant transport
R_w	Wellbore radius
S	Set of all solid elements
s_0	Location of fracture inlet
s	Coordinate system along the length of the fracture
S_c	Set of nodes that have a nodal support cut by fracture c
S_n	Set of all nodes in each element
$t_0(s)$	Time at which the fracturing fluid reaches the location s along the fracture
t	Time
$\bar{\mathbf{t}}$	Applied tractions on the Neumann boundary of the solid domain
t_c	Magnitude of the tractions due to contact and cohesive forces on the fracture interface
t_{end}	Time at which the simulation ends
$\mathbf{u}(\mathbf{x})$	Rock deformation
$\mathbf{u}$	Nodal displacements on the standard degrees of freedom for a given element
$\bar{\mathbf{u}}$	Prescribed displacements on the Dirichlet boundary of the solid domain
$\mathbf{u}^h(\mathbf{x})$	Approximation of rock displacement
$[\![\mathbf{u}]\!]$	Jump in the displacement field
$\tilde{\mathbf{u}}_I$	Nodal displacements on the standard degrees of freedom for node I
$\bar{v}$	Average slurry velocity along the fracture width
$\bar{v}_c$	Velocity of laminar Newtonian slurry between two parallel plates
$\bar{v}_d$	Velocity of fracturing fluid through packed proppant particles
$\bar{v}_f$	Average fluid velocity along the fracture width
$\bar{v}_p$	Average proppant velocity along the fracture width
$\mathbf{W}$	Diagonal matrix in which the diagonal terms are the fracture aperture at the center of each finite volume cell
w	Fracture aperture
w_c	Aperture at which the fracture is fully separated
w_f	Fracture aperture for slurry flow
w_0	Wellbore aperture
w_{res}	Residual fracture aperture
w_w	Aperture at which the cohesion in the fracture weakens
$\mathbf{x}$	Spatial coordinate
$\mathbf{x}_{tip}$	Location of the tip of the fracture

Superscripts

n	Pertaining to beginning of time step n
$n+1$	Pertaining to the end of time step n

Subscripts

i	Pertaining to the center of cell i
$i \pm 1$	Pertaining to the center of the cells directly adjacent to cell i
$i \pm 1/2$	Pertaining to the edges of cell i
k	Pertaining to an iteration of the Newton-Raphson scheme (outer loop) for solving the global mass conservation to determine the wellbore pressure
m	Pertaining to an iteration of the Newton-Raphson scheme (inner loop) for solving the coupled system of equations

Chapter 1

Introduction

1.1 Introduction to hydraulic fracturing simulations

Hydraulic fracturing is the process by which fluid is injected at a high pressure into the earth to create a network of fractures [4]. This process is most commonly associated with oil and gas production but is also used in enhanced geothermal systems [5] and hydraulic fracturing occurs naturally such as in the creation of magma-driven dikes [6]. This thesis is focused on the use of hydraulic fracturing in oil and gas production as a stimulation technique for reservoirs with low permeability in which conventional means cannot be used to extract resources. Currently, hydraulic fracturing treatments are predominantly being used in shale reservoirs. The combination of horizontal drilling and hydraulic fracturing has allowed for large volumes of shale reservoirs to be stimulated for production, leading to a 50% increase in natural gas production in the United States over the past decade [7].

During hydraulic fracturing, a mixture of fluid, chemicals, and proppant, called *fracking fluid*, is injected into the subsurface in various stages to create fractures along a well. A horizontal plan view of a rock mass undergoing injection from the center of the domain is depicted in Figure 1.1, where the well is oriented perpendicular to the image. A treatment cycle begins with the injection of a "pad" of clean fluid to create and propagate the fracture network. Afterward, a slurry mixture of fluid and proppant (small solid particles, such as sand) is injected, creating a propped reservoir zone. The role of the proppant is to hold open any fractures after the fluid injection ceases (shut-in). The propped zone represents the volume of reservoir that remains open after shut-in, shown in blue in Figure 1.1. During the treatment cycle, changes in the stress state cause pre-existing natural fractures in the surrounding area to shear and remain self-dilated due to the roughness of the natural fracture surfaces. Shear dilation of natural fractures creates a broader stimulated zone, as shown in orange in Figure 1.1. Once the proppant has been distributed throughout the fracture network, the pumping is stopped and the fracture network finds a new

unpressurized equilibrium. During this time, the fluid inside the fracture can leak-off into the reservoir or flow back to the surface through the well where it is collected for disposal and/or reuse. Once the fracture has closed, the hydrocarbons within the reservoir are produced. The treatment can last from tens of minutes to hours, depending on the treatment design [4].

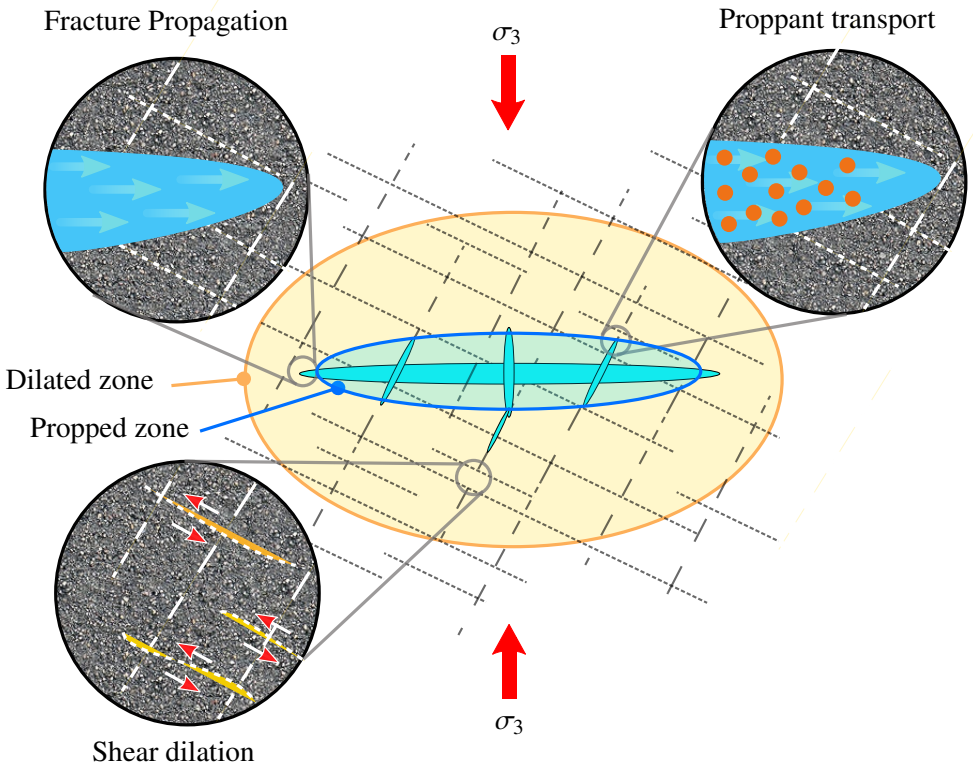

Figure 1.1: Fracture network stimulation: Propagation due to pad flow (top-left), proppant transport through the fracture (top-right), and shear-dilation in surrounding natural fractures (bottom-left). Figure modified from Dusseault [8]

In oil and gas production, permeability and conductivity, which are closely related properties of a rock mass, are the principal factors that govern the effectiveness of the hydraulic fracturing treatment. The permeability of a reservoir is a function of the degree of interconnection between the fracture network, and conductivity is a measure of how easily a given fluid can flow through the fracture network. These factors affect the amount of hydrocarbon fluids that can be pumped out of a formation [9].

The primary objective of hydraulic fracturing in oil and gas production is to enhance well production. For this reason, researchers discuss increased well performance in terms of stimulated reservoir volume (SRV), drainage area, or effective permeability. SRV is the volume of failed rock,

typically defined using microseismic analysis [10]; drainage area is the area of the formation in contact with the wellbore [4], and; effective permeability is a measure of the ability of the fractured rock mass to transmit fluids. Increasing each of these quantities is achieved through the creation of conductive pathways (fractures) that are self-propped or held open by proppant. The three main mechanisms during hydraulic fracturing for oil and gas production which largely impact the reservoir production are the shear dilation, fracture propagation, and proppant transport. The design of a hydraulic fracturing treatment includes the selection of well location, fluid mixture properties, proppant properties, fracture spacing, and pump schedule (volume, duration, and rate) to optimize the generated reservoir production [4].

Due to the lack of visual observation of the fracturing outcomes, companies use the limited data they have to hypothesize about the mechanisms taking place (diagnostic) and use basic rock mechanics principles and analytical models to design the fracturing procedure (predictive). Many basic questions remain unanswered, such as: what is the geometry of the fracture network? how much permeability enhancement will this treatment provide? what are the stimulated reservoir volume (SRV) and the effective propped volume (EPV)? Hydraulic fracturing is also of public interest due to the awareness of its potential environmental risks. There is concern about contamination of groundwater sources from the fracturing fluids, the large consumption of valuable water resources, and the generation of seismic activity by altering the stress state near active faults. More information is required to understand and mitigate the risks associated with hydraulic fracturing while optimizing its effectiveness.

To more accurately answer questions about hydraulic fracturing and its impacts on the environment, there is a need for improvement in all aspects of the problem domain: experimental research, data collection, and modeling. Hydraulic fracturing operations span kilometers of subsurface, the scale of which cannot be reproduced in a laboratory. The sparsely distributed logging wells in the treatment area also limit data collection due to the difficulty with reaching the source and taking samples that are representative of the scale and heterogeneity of the material. The models developed using the behavioral laws observed in experimental research and calibrated using data collected on-site are used to predict the results of the hydraulic fracturing treatment. Due to the complex mechanisms taking place, models require high computational effort and many simplifications/approximations to obtain a solution. The uncertainty that exists throughout all aspects of the problem domain is what makes hydraulic fracturing one of the most difficult engineering challenges. The focus of this project is on enhancing the knowledge in numerical modeling of hydraulic fracturing. Numerical models aid in the understanding, design, and optimization of treatments.

There are few analytical models of hydraulic fracturing currently available. The two most commonly used analytical models are based on the Khristianovic-Geertsma-de Klerk (KGD) geometry [11] and the Perkins-Kern-Nordgren (PKN) geometry [12, 13]. These are quasi-three dimensional constant-height models that depend on a stipulated fracture height. The PKN model applies to long fractures of limited height, and the KGD model applies to short fractures where

one can assume plane strain constitutive behavior along horizontal sections. A three-dimensional radial (or penny-shaped) model developed by Sneddon [14] is also available, which applies to homogeneous reservoirs with a point source injection. Without limiting assumptions, the set of governing equations that govern hydraulic fracturing are too complex to be solved analytically and therefore approximations are used to obtain the solutions. Numerical models are better equipped for solving the complex mechanisms simultaneously.

A large challenge in hydraulic fracture modeling is in coupling the various mechanisms in play to develop a robust tool that captures the complexities of the treatment process. While it is common to describe hydraulic fracturing as involving only three processes: the mechanical deformation induced by the fluid pressure on the fracture surfaces, the flow of fluid within the fracture, and the fracture propagation [15], in reality, modern operations are much more complex. There are many other important mechanisms involved in hydraulic fracturing, such as fracture initiation, fluid flow through the reservoir, interaction of hydraulic fractures with natural fractures and various rock strata, dilational effects of shearing natural fractures, effects of shear and temperature on fracturing fluid rheology, proppant transport through fractures, and fracture closure. Each of these mechanisms has been studied to various degrees by the scientific community since the 1950s. However, numerical modeling of each of these mechanisms has been developed primarily in isolation and most models currently available cannot capture their combined complexity robustly.

There is no hydraulic fracturing model currently available that incorporates all of the aforementioned mechanisms that lead to enhanced production. Such a model would be an invaluable tool for making operational decisions, such as optimization of the fracturing fluid properties and injection rates to achieve greater well performance. Although the focus is on oil and gas production, this model also has applications in massive slurried solid waste disposal, where the objective is to ensure no flow-back of the slurried waste [16]. Ultimately, numerical models of hydraulic fracturing are tools that provide a more fundamental understanding of hydraulic fracturing.

1.2 Shear dilation

Simulation of rock masses is complex due to the existence of discontinuities at many scales, from fissures at the microscale, bedding planes and natural fractures at the centimeter to meter scale, to faults at the reservoir scale. The behavior of a rock mass is determined by the interaction of these discontinuities. At depth, the surfaces of natural fractures are often cohesively sealed [17]. When naturally fractured rock is subjected to differential compressive stresses, the natural fractures are reactivated and mixed-mode fracture behavior and frictional sliding follows. As fracture surfaces slip relative to one another, asperities along the fracture surfaces can cause gaps in the normal displacement that persist even after loads are removed [17]. This mechanism is called shear dilation and is depicted in Figure 1.2.

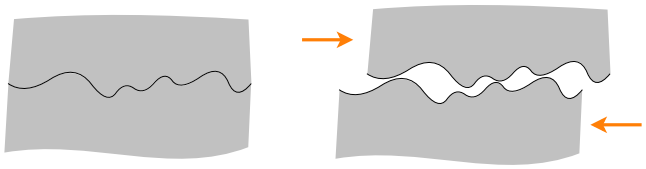

Figure 1.2: Shear dilation of a rough joint; mated fracture (left) and dilated fracture (right)

Shear dilation is an important mechanism in rock mechanics because it explains the counter-intuitive notion that rock can increase in volume as it is being compressed. Furthermore, in the context of hydraulic stimulation of reservoirs for oil and gas or geothermal applications, shear dilation of natural fractures is a key mechanism for permeability enhancement. Understanding and quantifying the conditions which cause an increase in permeability is necessary for the design of efficient stimulation treatments [18].

Experimental studies of rock joint deformation and shear dilation were first performed in the 1960s and led to the establishment of first-order constitutive models [17, 19–21]. It was understood early on that dilation is most prevalent at low confining effective stresses. As the confining stresses increase, an increase in the resistance to the normal displacement of fracture surfaces causes a decrease in dilatancy. Dilation is completely suppressed when the average normal stress to the fracture surfaces is of the order of magnitude of the unconfined compressive strength of the asperities and the shear strength of the fracture is dominated by the strength of the asperities [17]. Initial behavioral models, such as those by Goldstein *et al.* [20], Patton [21], and Newland and Allely [22], included this as a part of the shear strength characteristics of the material as opposed to a completely separate dilation model. Later, Barton *et al.* [19] used experimental observations to define a parabolic empirical expression for the amount of dilation as a function of surface roughness, weathering of the surface, shear displacement and normal stress, known as the Barton-Bandis joint model. Another approach is to model the dilation as a linear function of shear displacement [23], as used in this study. This model resembles a perfect plasticity model in that the dilation does not begin until the peak shear strength is reached and it remains constant after a critical shear displacement.

Naturally fractured rock masses have been simulated previously using various numerical approaches. Continuum models using the finite difference and finite element methods, which introduce the effect of frictional dilation through an equivalent constitutive model of the material have been used [24–26]. Discontinuum models simulate rock joints explicitly, and include the effect of shear dilation as a constitutive model along each joint [18, 23, 27–29].

Discontinuum models can be further classified into models that rely on meshes that conform to the discontinuities and models that enrich the approximation space so that the discontinuities can be modeled independently of the mesh. A type of discontinuum model with conforming mesh is the discrete element method (DEM), which has been used to model rock joints explicitly [30–32].

Enriched methods based on the concept of a partition of unity have become popular tools for simulating propagating fractures when the fracture path is not known *a priori* (e.g. Belytschko and Black [33], Moës *et al.* [34], Sukumar *et al.* [35], Duarte *et al.* [36], Gravouil *et al.* [37], Zi *et al.* [38], Areias and Belytschko [39], Gupta and Duarte [40, 41], and Remij [42]). A key feature of enriched methods is that the discontinuity is represented independently of the mesh and so no remeshing is required with propagation. A partition of unity is a set of functions in a domain such that the sum of the functions at any point in the domain is equal to one. This concept forms the basis of the extended finite element method (XFEM) and the generalized finite element method (GFEM), which exploit the fact that any function can be reproduced by a product of the partition of unity functions to add enriched shape functions to the polynomial approximation space. The shape functions are customized to capture the discontinuities along fractures. An overview of the XFEM/GFEM can be found in the works of Karihaloo and Xiao [43], Abdelaziz and Hamouine [44], Mohammadi [45], Belytschko *et al.* [46], Rabczuk *et al.* [47], Fries and Belytschko [48], and Khoei [49]. The XFEM and GFEM are identical methods but will be referred to as the XFEM in the remainder of the paper.

A fracture can propagate in an opening mode due to tension (I), sliding mode due to in-plane shear (II), and tearing mode due to out-of-plane shear (III). Hydraulic fracturing models within the XFEM community have primarily focused on Mode I dominated fracture propagation. The XFEM has been successfully applied to fatigue fracture [34, 50, 51], the dynamic propagation of cohesive fractures [52, 53], and shear-band evolution [54–56]. However, the target applications have not focused on shear yield under compressive loads, in which friction, contact, and shear dilation are of importance.

Researchers have studied lateral and frictional contact by means of various techniques such as Latin method [57], penalty method [58], augmented Lagrange multipliers [58–60] and others [61] using the XFEM. Nevertheless, the effect of shear dilation has not yet been studied in these models.

1.3 Proppant transport

In hydraulic fracturing treatments, proppant (granular material, typically sand) is injected into the formation to keep the fracture network open after pumping ceases. Proppant usage worldwide has increased drastically since 2009, with close to 92 billion pounds of proppant pumped in 2013 [62]. The final position of the slurry–the mixture of wellbore fluids and proppant–in the fracture network following injection plays a large role in determining the final permeability of the treated volume. A review of the geomechanics and numerical methods used in modeling hydraulic fracturing is provided by Adachi *et al.* [15], Detournay [63], Hattori *et al.* [64], and Lecampion *et al.* [65].

An extensive review of the fluid mechanics associated with multiphase flow in hydraulic fracturing has been given by Osiptsov [66]. Early researchers tackled the problem of modeling proppant

transport using simplified models to find the position of proppant over time through a stationary channel and focused on the mechanism of proppant settling towards the bottom of the channel [67, 68]. Mixture models, which solve for the conservation of mass of the slurry and the proppant to advance the proppant concentration [15, 69–72], have also been used. These models assume that the phases are fully mixed and treat the slurry as a fluid with a modified viscosity and density based on the concentration of proppant. The fluid and proppant are assumed to be incompressible and the fracture width is assumed to be small enough compared to the other fracture dimensions that lubrication theory holds. The most basic form of the mixture model assumes that the slurry components (fluid and proppant particles) travel at the same velocity. The difference in velocity between the slurry and the proppant particles has been considered by some authors, but in most models only slip along the height of the fracture due to convection and settlement is accounted for. A notable exception is the model by Dontsov and Peirce [73], which provides a slip related to the Darcy flow of fluid through the proppant pack once the proppant concentration reaches a saturated level. Two-phase modeling of proppant transport has also been approached by Boronin and Osiptsov [74], in which both the conservation of momentum and mass are solved for the fluid and the proppant particles. This type of model provides a deeper understanding of the interaction between the two phases but is computationally expensive.

A mixture model is considered in this thesis due to its efficiency and ease of implementation with other reservoir models. Three governing equations are typically solved for in hydraulic fracturing simulations: (I) conservation of momentum governing rock deformation, (II) conservation of mass governing slurry flow, and (III) conservation of mass governing proppant flow. The second equation inherently incorporates the conservation of mass of the carrier fluid. These three equations are used to solve for the rock mass displacement, fluid pressure, and proppant concentration, respectively. All equations are functions of the three independent variables and are strongly coupled in terms of the physical processes involved.

The continuity equation that governs the proppant flow through the fracture is a nonlinear hyperbolic advection equation. The advection equation has been solved in hydraulic fracture models using the finite volume method [70, 71, 75–77], the finite difference method [72, 78], and the finite element method [69]. Most models are solved using an Eulerian frame of reference, but a solution using a Lagrangian frame of reference is also possible [79]. The coupled mixture models in the literature assume a constant slurry velocity during the proppant transport update, which often leads to a linear advection equation. Finite volume schemes have been used to solve nonlinear advection of proppant in a hydraulic fracture [71, 75], although the slurry velocity is also held constant during the solution of the proppant transport equation in these models. Finite volume schemes have also been used by various researchers to model nonlinear hyperbolic equations in similar fields, such as the work by Varadarajan and Hammond [80] in modeling gas migration and Lorentzen and Fjelde [81] in modeling multiphase hydrocarbon flow in pipelines.

Numerically, solving the nonlinear equation presents additional challenges due to the shock waves created in the solution that must be considered in the approximation. Oscillations may be intro-

duced into the solution if the characteristic speed at the cell edges is not properly approximated. An entropy correction must be included in the formulation to handle rarefaction waves. Additionally, proppant concentration constraints must be imposed on the solution so that the approximation does not lead to results that are outside the physically possible limits since this is not handled naturally by the governing equation. The complexities of solving the nonlinear heterogeneous hyperbolic equation that governs proppant transport have not been properly addressed in the literature.

1.4 Coupled problems

In its most basic form, a hydraulic fracturing model contains three processes: (1) deformation of the solid rock mass, (2) flow of fluid through the fracture, and (3) fracture propagation [15]. The majority of work on models that simulate hydraulic fracturing have focused on the three processes mentioned above. A fourth process is required in hydraulic fracturing models, (4) the transport of proppant through the fracture. These four physical processes directly affect each other in a nonlinear way. There is higher fluid pressure in areas of a fracture with increased proppant concentration. Consequently, the increased fluid pressure leads to larger fracture apertures. A build-up of proppant may also prevent fluid from entering the fracture tip which limits fracture propagation, a phenomenon commonly known as a tip screen-out [4, 82].

There has been limited research on the coupling of slurry transport with fracture propagation (e.g. Zhou *et al.* [70], Shiozawa and McClure [71], Vahab and Khalili [72], Dontsov and Peirce [75], Kong *et al.* [78], and Shi *et al.* [83]). Solving the nonlinear coupled system of equations may be done monolithically or using a staggered scheme. In a monolithic scheme (also known as a fully-coupled scheme), the equations that govern the rock deformation, fluid flow, and proppant transport are all solved simultaneously. In a staggered scheme, the equations are solved sequentially by making assumptions about the independent variables as each equation is solved and iterating to ensure convergence of all equations [84]. A loosely-coupled scheme (also known as a one-pass method) is a type of staggered scheme in which no iteration is performed after sequentially solving the equations. It has been shown by Gordeliy and Peirce [85] and Parchei Esfahani and Gracie [86] that some staggered schemes for hydro-mechanically coupled systems may cause spurious oscillations and fail to converge; monolithic schemes are more robust and are generally expected to have the highest convergence rate.

In current hydraulic fracturing models, proppant transport has only been loosely-coupled as an update at the end of a time step (e.g. Adachi *et al.* [15], Zhou *et al.* [70], Shiozawa and McClure [71], Dontsov and Peirce [75], Kong *et al.* [78], and Shi *et al.* [83]). A loosely-coupled model consists of getting a converged solution for the first three processes (solid deformation, fluid flow, and fracture propagation) in a time step, and then computing the proppant concentration at the end without iteration to confirm convergence. The convergence and robustness of loosely-coupled

schemes need to be addressed. A study of the stability and convergence of coupling schemes with proppant transport is not yet available in the literature.

1.5 Motivations

The purpose of a hydraulic fracturing treatment is to enhance the production of oil and gas from a reservoir. Production is impacted by (1) fracture growth which defines the extent of the connected fracture network, (2) the proppant distribution within the fracture network which determines the extent of the fractures which remain open after pumping is stopped, and (3) shear dilation of the surrounding natural fractures which allows for opening of a broader reservoir volume. The goal of this thesis is to simulate the mechanisms that lead to improved reservoir productivity due to hydraulic fracturing treatments: fracture propagation, proppant transport, and shear dilation.

Several gaps in the literature have been identified that need to be addressed in the realization of the main goal:

- failure of fractured rock masses in which Mode II fracture propagation, frictional contact, and shear dilation are all simultaneously active has not yet been incorporated into a numerical model within the framework of the XFEM;
- solution of the nonlinear and heterogeneous advection equation that governs proppant transport and the shock waves in the solution that are inherent in this nonlinear problem have not yet been addressed in the literature;
- finally, the coupling of proppant transport into hydraulic fracturing models has not been previously studied. Models currently available in the literature have only loosely coupled the proppant transport equation to the equations governing rock deformation and fluid flow. Convergence and robustness of this loose coupling strategy are questionable and require further study.

The nonlinear and non-smooth nature of the system of equations is expected to cause numerical instability and convergence issues. Deformation of the solid rock mass is nonlinear due to the cohesive tractions present at the tip of the fracture, and non-smooth due to the piecewise nature of the tractions due to frictional contact and shear-dilation. The fluid flow through a hydraulic fracture also exhibits a non-smooth behavior as the proppant concentration reaches a saturation point and the flow transitions from Poiseuille flow through the fracture walls to Darcy flow through packed proppant particles. The equation that governs proppant transport through a hydraulic fracture is a nonlinear hyperbolic equation which creates shock waves in the solution that must be appropriately accounted for. Unlike the works of previous hydraulic fracture models in the literature which model only linear advection of proppant, the nonlinear form is required

to capture the build-up of proppant packs and subsequent flushing. Constraints must also be imposed on the proppant concentration so that the approximation does not lead to results that are outside the physically-possible limits. As the fracture propagates, the domain along which the equations exist is modified, introducing an additional source of non-smoothness. Solution methods to address this complex nonlinear and non-smooth behavior are addressed in this thesis. Careful consideration of the coupling strategy is required to ensure that the model is robust enough to model a variety of scenarios (such as a tip screen-out) without compromising accuracy.

1.6 Research objectives and methodologies

Given the aforementioned background, the overarching objectives of this thesis are presented in this section, along with the methodologies used to accomplish each of the objectives.

1.6.1 Objective 1: Develop a numerical model for the simulation of the mechanical deformation and shear dilation of naturally fractured rock masses

The extended finite element method is used to model the deformation of a fractured reservoir. Using this method, a fracture network is modeled using junction enrichment functions at nodes that neighbor fracture intersections. The model incorporates frictional contact and shear dilation along the fracture network. A linear shear dilation model capped by a dilation limiting displacement is applied on the fracture surfaces. To study the Mode II fracturing behavior in a quasi-static context, a dynamic relaxation scheme with explicit time integration is used. The numerical model is verified through the simulation of a shear test, and convergence is shown through the simulation of a biaxial test on a fractured rock specimen. The completed objective is described in Chapter 2 of the thesis, which is based on the following article:

Rivas, E. *et al.*, A two-dimensional extended finite element method model of discrete fracture networks, *International Journal for Numerical Methods in Engineering*, vol. 117, no. 13, pp. 1263–1282, 2019

1.6.2 Objective 2: Develop a numerical model for the simulation of proppant transport through planar fractures

The finite volume method is used to model the nonlinear heterogeneous hyperbolic equation that governs proppant transport through a fracture. A mixture model of the slurry is used which assumes that the fluid and proppant phases are fully mixed. The nonlinear advection of proppant

is simulated in this work using the Godunov approximation with an entropy fix and a high-resolution correction using slope limiters. The constitutive model incorporates the mechanism of proppant bridging along narrow sections of a fracture. Additionally, a predictor-corrector algorithm is implemented to impose constraints on the proppant concentration to ensure that it does not exceed physically permissible limits. Using the aforementioned methodology, this model is used to simulate a tip screen-out. The numerical model is verified through a comparison with characteristic solutions. The completed objective is described in Chapter 3 of the thesis, which is based on the following article:

Rivas, E. and Gracie, R., Numerical considerations for the simulation of proppant transport through fractures, *Journal of Petroleum Science and Engineering*, 2019

1.6.3 Objective 3: Develop a numerical model for the simulation of proppant transport through propagating non-planar fractures

A numerical model which couples rock deformation, fluid flow, and proppant transport is developed. The XFEM, FEM, and FVM are used to model rock deformation, fluid flow, and proppant transport, respectively. Proppant bridging and the transition from Poiseuille flow of slurry through the fracture to Darcy flow of fluid through a proppant pack are included in the constitutive law of the slurry. An injection-rate controlled simulation is performed by imposing global mass conservation on the system with an iterative scheme. A cohesive zone model in conjunction with the maximum circumferential stress criterion is used to propagate fractures. Propagation of a planar fracture is verified against analytical solutions for KGD fractures and non-planar fracture propagation from a wellbore is also verified. A comparison of monolithic, sequential, and loose coupling schemes is performed. The completed objective is described in Chapter 4 of the thesis, which is based on the following article:

Rivas, E. and Gracie, R., A monolithic coupled hydraulic fracture model with proppant transport, *Manuscript submitted for publication*, 2020

Chapter 2

A two-dimensional extended finite element method model of discrete fracture networks

2.1 Introduction

In this chapter, the framework and formulation for including the mechanism of shear dilation in the extended finite element method (XFEM) are developed. While a fractured rock mass has been modeled with the XFEM before [87–89], the focus in XFEM models of hydraulic fracturing has mainly been on the simulation of a single fracture (or very few) under Mode I propagation. The failure of fractured rock masses under compressive regimes in which Mode II fracture, shear dilation, and frictional contact are all simultaneously active has not been investigated to date. Here, an XFEM model including the physics of frictional contact, cohesive fracture, and, most notably, shear dilation is presented. This chapter is focused on modeling discontinuities stemming from the natural fracture network; however, the methodology can be applied to other types of discontinuities. In this model, fluid flow within the fracture network is ignored and the rock mass is assumed to be impervious. As such, the model is not able to simulate the production of hydrocarbons due to shear dilation. The scope is limited to modeling the shear dilation in fractured rock masses.

The governing equations and XFEM approximation are discussed in Section 2.2. The constitutive interface models are described in Section 2.3, and the XFEM discretization is described in section 2.4. Finally, at the end of this chapter, the XFEM model is verified using a shear test of a single joint under various confining stresses, and the convergence of the model is demonstrated using a biaxial test involving a Discrete Fracture Network (DFN). The XFEM model is then used to evaluate the stability of an XFEM-DFN simulation of a naturally fractured rock mass slope.

2.2 Governing equations

The governing equations of a naturally fractured medium are derived in this section. Consider the motion of a two-dimensional body Ω. The domain of the body is illustrated in Figure 2.1, with an external boundary denoted by Γ, which has a normal vector $\hat{\mathbf{n}}$. The boundary is divided into mutually exclusive sets Γ_u and Γ_t, corresponding to the Dirichlet and Neumann boundaries, respectively. The body also contains internal boundaries, which are considered natural fractures, denoted by Γ_c. These internal boundaries have normal and tangential base vectors $\hat{\mathbf{n}}_{\Gamma_c}(\mathbf{x})$ and $\hat{\mathbf{e}}_{\Gamma_c}(\mathbf{x})$ defined along their lengths. Each fracture has two faces, denoted by Γ_c^+ and Γ_c^-. The normal and tangential base vectors are defined on the positive face of the fracture, pointing into the domain. The displacement of a material point, $\mathbf{x}$, at time t is denoted by $\mathbf{u}(\mathbf{x}, t)$. This formulation is derived under the assumption of small deformations, and as such, there is no differentiation between material points in the deformed and undeformed configurations. The deformation of the natural fractures is small, on the scale of millimeters, compared to the volume of a rock mass which is on the scale of hundreds of square meters. The deformation of a smaller rock specimen may also be studied using this assumption as long as the deformation remains small compared to the size of the specimen, as is the case under externally-applied confining stresses.

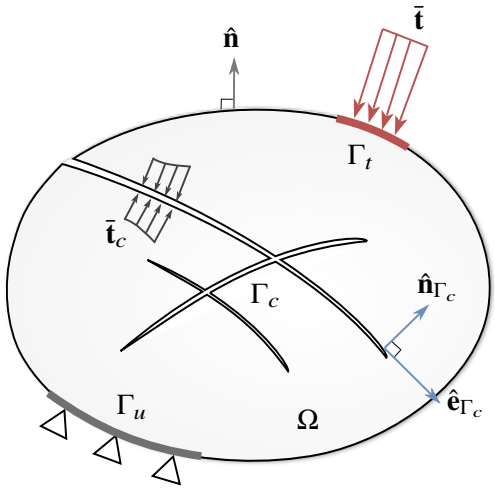

Figure 2.1: Domain of fractured rock mass

The motion of the domain is governed by conservation of momentum

$$\nabla \cdot \boldsymbol{\sigma} + \mathbf{b} = \rho \ddot{\mathbf{u}}, \quad \forall\, \mathbf{x} \in \Omega,\ t \geq 0 \tag{2.1}$$

in which $\ddot{\mathbf{u}}(\mathbf{x}, t)$ denotes the second partial derivative of the displacement field (acceleration), ρ

is the density of the medium, and $\boldsymbol{\sigma}$ is the Cauchy stress tensor. The body is subjected to a body force, $\mathbf{b}$.

The initial conditions on the domain are represented as

$$\begin{aligned} \mathbf{u}(\mathbf{x}, 0) &= \mathbf{u}_0(\mathbf{x}), \quad \forall\, \mathbf{x} \in \Omega \\ \dot{\mathbf{u}}(\mathbf{x}, 0) &= \dot{\mathbf{u}}_0(\mathbf{x}), \quad \forall\, \mathbf{x} \in \Omega \end{aligned} \tag{2.2}$$

in which $\mathbf{u}_0(\mathbf{x})$ and $\dot{\mathbf{u}}_0(\mathbf{x})$ are the initial displacement and velocity fields, respectively.

The boundary is subjected to an external traction, $\bar{\mathbf{t}}$, along Γ_t, a prescribed displacement, $\bar{\mathbf{u}}$, along Γ_u, and a traction, $\bar{\mathbf{t}}_c$, along the fracture interface, Γ_c. The boundary conditions on the external and internal boundaries are

$$\begin{aligned} \mathbf{u} &= \bar{\mathbf{u}}, \quad \forall\, \mathbf{x} \in \Gamma_u \\ \boldsymbol{\sigma} \cdot \hat{\mathbf{n}} &= \bar{\mathbf{t}}, \quad \forall\, \mathbf{x} \in \Gamma_t \\ \boldsymbol{\sigma} \cdot \hat{\mathbf{n}}_{\Gamma_c} &= \bar{\mathbf{t}}_c, \quad \forall\, \mathbf{x} \in \Gamma_c \end{aligned} \tag{2.3}$$

The boundary conditions and constitutive laws governing the traction acting along the fracture, $\bar{\mathbf{t}}_c$, due to cohesion and frictional contact are described in detail in Section 2.3.

Multiplying the governing equation (2.1) by a test function, $\delta\mathbf{u}(\mathbf{x}) \in U_0$, and integrating over the domain Ω, the weak form of equilibrium is derived to allow for an approximation that is a function of a weaker continuity:

Find $\mathbf{u}(\mathbf{x}, t) \in U$ such that

$$\int_\Omega \delta\mathbf{u}^\top \rho \ddot{\mathbf{u}} d\Omega + \int_\Omega (\boldsymbol{\nabla}^s \delta\mathbf{u})^\top \boldsymbol{\sigma} d\Omega - \int_\Omega \delta\mathbf{u}^\top \mathbf{b} d\Omega - \oint_{\Gamma_t} \delta\mathbf{u}^\top \bar{\mathbf{t}} d\Gamma - \oint_{\Gamma_c} [\![\delta\mathbf{u}]\!]^\top \bar{\mathbf{t}}_c d\Gamma = 0 \quad \forall\, \delta\mathbf{u} \in U_0 \tag{2.4}$$

in which the space of admissible solutions, U, and admissible test functions, U_0, are defined on the space of functions with square integrable derivatives, H^1, as:

$$\begin{aligned} U &= \{\mathbf{u}(\mathbf{x}, t) |\, \mathbf{u}(\mathbf{x}, t) \in H^1, \mathbf{u}(\mathbf{x}, 0) = \mathbf{u_0}(\mathbf{x}),\ \mathbf{u} = \bar{\mathbf{u}} \text{ on } \Gamma_u,\ \mathbf{u} \text{ discontinuous on } \Gamma_c\} \\ U_0 &= \{\delta\mathbf{u}(\mathbf{x}) |\, \delta\mathbf{u}(\mathbf{x}) \in H^1,\ \delta\mathbf{u} = 0 \text{ on } \Gamma_u,\ \delta\mathbf{u} \text{ discontinuous on } \Gamma_c\} \end{aligned} \tag{2.5}$$

Voigt notation is assumed for all equations after this point. In this notation, the Cauchy stress is $\boldsymbol{\sigma}^\top = \begin{bmatrix} \sigma_{11} & \sigma_{22} & \sigma_{12} \end{bmatrix}$. A linear constitutive law of the form $\boldsymbol{\sigma} = \mathbf{D}\boldsymbol{\varepsilon}$ is assumed, in which $\mathbf{D}$ is the two-dimensional plane-strain elasticity matrix, and $\boldsymbol{\varepsilon} = \nabla^s \mathbf{u}$ is the infinitesimal strain.

2.3 Interface constitutive models

The traction acting along the fracture comprises frictional contact and cohesive forces. Contact and cohesive forces act normal to the fracture surfaces, and frictional forces act tangential to the fracture surfaces. While frictional contact has been implemented by various authors [57, 58, 60], this work is the first to include dilation of the rock joint, which modifies the constitutive model for contact. The total traction acting along the fracture is defined with respect to the components normal and tangential to the fracture face, $\bar{\mathbf{t}}_{cn}$ and $\bar{\mathbf{t}}_{ct}$, respectively, as

$$\begin{aligned} \bar{\mathbf{t}}_c &= \left(\bar{t}^{con} + \bar{t}^{coh}\right) \hat{\mathbf{n}}_{\Gamma_c} + \left(\bar{t}^{fric}\right) \hat{\mathbf{e}}_{\Gamma_c} \\ &= \bar{\mathbf{t}}_{cn} + \bar{\mathbf{t}}_{ct} \end{aligned} \tag{2.6}$$

The magnitude of the contact, cohesion, and friction forces are denoted by $\bar{t}^{con}$, $\bar{t}^{coh}$, and $\bar{t}^{fric}$, respectively. The constitutive models for the tractions along the fracture are defined in terms of the jump in the displacement field across the fracture. This jump is represented as $[\![\mathbf{u}(\mathbf{x})]\!] = \mathbf{u}(\mathbf{x}^+) - \mathbf{u}(\mathbf{x}^-)$ on Γ_c, in which $\mathbf{u}(\mathbf{x}^+)$ and $\mathbf{u}(\mathbf{x}^-)$ are the displacements on the positive and negative side of the fracture boundary, respectively. The jump can be decomposed into the normal and tangential jump in displacement, $u_n(\mathbf{x})$ and $u_t(\mathbf{x})$, respectively, such that

$$\begin{aligned} u_n(\mathbf{x}) &= [\![\mathbf{u}(\mathbf{x})]\!] \cdot \hat{\mathbf{n}}_{\Gamma_c}(\mathbf{x}) \\ u_t(\mathbf{x}) &= [\![\mathbf{u}(\mathbf{x})]\!] \cdot \hat{\mathbf{e}}_{\Gamma_c}(\mathbf{x}) \end{aligned} \tag{2.7}$$

The normal vector, $\hat{\mathbf{n}}_{\Gamma_c}$, is defined as the outward normal to the negative face, pointing in the direction of the positive face of the fracture. Using this convention, a negative normal jump signifies an overlap of the fracture faces, whereas a positive normal jump signifies a separation of the fracture faces. In this study, forces at the fracture are applied under the assumption of small deformations. This eliminates the need for a contact search algorithm and reduces the computational cost of the simulation. For large deformation problems, this assumption is not valid, and a contact search algorithm should be implemented [90].

2.3.1 Contact and cohesive forces

Contact and cohesive forces act normal to the fracture surfaces. Contact forces are applied to prevent the non-physical overlap of fracture surfaces. Natural fractures are typically sealed due to the effect of cementation over time under confining stresses. Cohesive forces that impede the opening of fracture surfaces are applied to model the naturally sealed fractures.

Contact is applied along the fracture surface using the penalty method, and the governing equations, (2.1), must be satisfied under the constraints that the normal jump in displacement must be

greater than the dilation along the fracture, u_n^d, and that the traction acting on the positive side of the fracture must be equal and opposite to the traction acting on the negative side of the fracture.

$$\begin{aligned} u_n(\mathbf{x}) &\geq u_n^d, && \forall\, \mathbf{x} \in \Gamma_c \\ \boldsymbol{\sigma}^+ \cdot \hat{\mathbf{n}}_{\Gamma_c}^+ &= -\boldsymbol{\sigma}^- \cdot \hat{\mathbf{n}}_{\Gamma_c}^-, && \forall\, \mathbf{x} \in \Gamma_c \end{aligned} \tag{2.8}$$

These constraints are imposed by applying equal and opposite tractions on either side of the fracture. The magnitude of the traction is obtained from the left side of the traction-separation curve, as shown in Figure 2.2a. The traction-separation law is defined as

$$\bar{t}^{con} = \begin{cases} k_n(u_n - u_n^d), & u_n \leq u_n^d \\ 0, & \text{otherwise} \end{cases} \tag{2.9}$$

The penalty method is equivalent to placing springs on either side of the fracture. Although an overlap of the fracture surfaces is not physically possible, it is used numerically to compute the magnitude of traction required to prevent the overlap. In this context, the contact stiffness, k_n, is physically equivalent to the elasticity of the springs. The main difficulty in using the penalty method for contact as described in this section is the selection of this stiffness parameter [90, 91], which is problem-dependent. As the parameter goes to infinity, the solution converges to the exact solution. However, the solution faces stability issues if this parameter is too high. Some strategies to limit the penalty parameter include keeping the penalty parameter in the same range as the stiffness terms of the surrounding domain and to estimate the contact stiffness based on the stable time step [92].

A bilinear intrinsic cohesive model, similar to the one proposed by Geubelle and Baylor [93], is used in this study. The magnitude of the traction is depicted on the right side of the traction-separation curve in Figure 2.2a. The traction-separation law is defined as

$$\bar{t}^{coh} = \begin{cases} k_1(u_n - u_n^d), & u_n^d < u_n \leq u_n^{max} \\ f_u - k_2(u_n - u_n^{max}), & u_n^{max} < u_n \leq u_n^{sep} \\ 0 & \text{otherwise} \end{cases} \tag{2.10}$$

This model is characterized by an elastic range, in which the traction increases until it reaches a maximum value. The stiffness of the cohesive model during this elastic section is matched with the contact stiffness of the fracture, $k_1 = k_n$. The maximum cohesive traction is set equal to the yield strength of the material, f_u. Finally, there is a softening behavior until the fracture is completely separated. The aperture at which the fracture is fully separated, u_n^{sep}, is selected based on the fracture energy of the material, such that the area under the traction-separation law is equal to the Mode I fracture energy [93].

$$G_{Ic} = \frac{1}{2} f_u \left(u_n^{sep} - u_n^d \right) \tag{2.11}$$

The traction-separation curve used in this chapter is non-smooth at u_n^{max} and u_n^{sep}. Another source of non-smoothness is the amount of dilation in the fracture, u_n^d. As the dilation changes, the x-intercept of the traction-separation curve moves and creates an entirely new traction-separation law. While a smooth traction-separation curve is also possible and leads to well-defined derivatives along the curve, it does not remove the non-smoothness that arises from the dilation in the system.

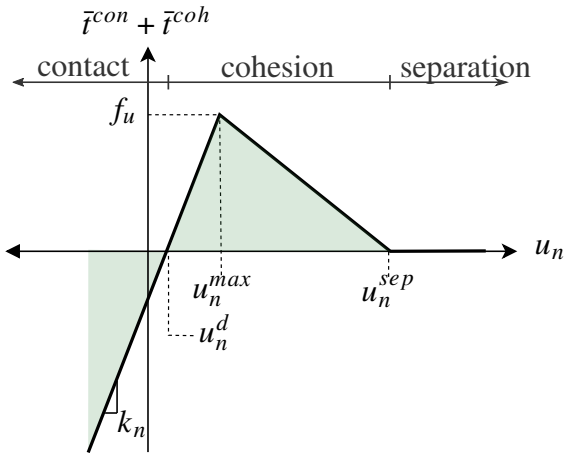

(a) Constitutive law for contact and cohesive tractions acting normal to the fracture interface

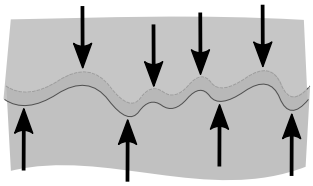

(b) Contact forces acting on fracture surface

Figure 2.2: Traction-separation curve and sketch of contact forces on rough fracture surface

2.3.2 Friction

Frictional forces are also modeled along the fracture when the faces are in contact. An elasto-plastic formulation of Coulomb friction is used, as shown by the shear traction-separation curve in Figure 2.3a. The relationship between frictional traction and shear displacement is defined when the fracture is in contact (the first case in the equation below corresponds to Figure 2.3a), and there is no friction when the fracture is in a separation state

$$|\bar{t}^{fric}| = \begin{cases} |k_t u_t| \leq \tau_{crit}, & u_n \leq u_n^d \\ 0, & \text{otherwise} \end{cases} \tag{2.12}$$

The frictional stiffness, k_t, is also a problem-specific parameter. A predictor-corrector algorithm,

similar to the implementation used in classical plasticity, is used to model the yielding of the frictional traction along the fracture. The fracture is initially in a “stick” state, in which the shear displacement is limited by a linearly proportional shear traction, similar to contact in the normal direction. When the traction reaches the shear strength of the material, it moves into a “slip" state, in which the fracture surface has yielded. A linear Coulomb failure criterion is used to define the shear strength of the material as

$$\tau_{crit} = c_f + |\bar{t}^{con}| \tan(\phi) \tag{2.13}$$

in which c_f is the shear strength due to cohesion and ϕ is the angle of friction of the fractures.

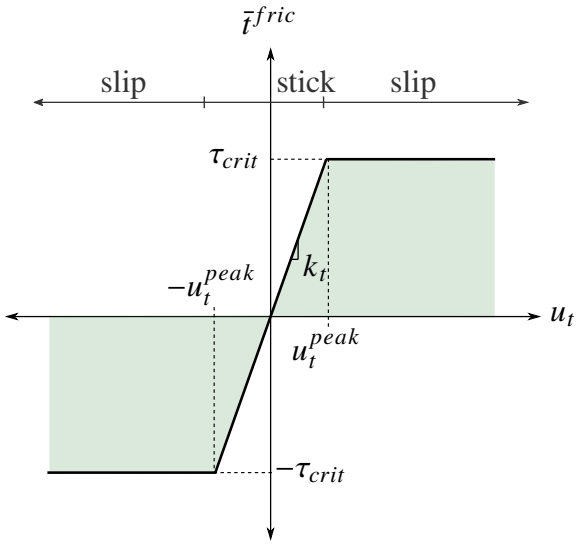

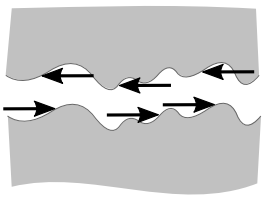

(a) Constitutive model for frictional tractions acting tangential to fracture surface

(b) Friction forces acting on fracture surface

Figure 2.3: Friction constitutive model and sketch of frictional forces acting on rough fracture surface

2.3.3 Shear dilation

The dilation in the system is dependent on the relative tangential displacement and the normal traction acting on the fracture. This mechanism has not yet been included in an XFEM model reported in the literature and is responsible for a permeability increase in the fractured medium. A linear constitutive law is used for dilation when the fracture is in contact (i.e., when $u_n \leq u_n^d$),

defined as [94]

$$u_n^d = \begin{cases} (|u_t| - u_t^{peak}) \tan(\varphi) & u_t^{peak} < |u_t| < u_t^{crit} \\ (u_t^{crit} - u_t^{peak}) \tan(\varphi) & |u_t| > u_t^{crit} \\ 0 & \text{otherwise} \end{cases} \tag{2.14}$$

In this model, the fracture begins to dilate after it slips, and the amount of dilation increases proportionally to the amount of slip with a dilation angle, φ, as shown in Figure 2.4a. The dilation growth is capped at a critical shear displacement, u_t^{crit}. In this study, the critical shear displacement is defined as the peak shear displacement for a normal load equivalent to the unconfined compressive strength of the material, σ_u.

$$u_t^{crit} = \frac{\sigma_u \tan(\phi) + c_f}{k_t} \tag{2.15}$$

Note that if the critical shear displacement is not greater than the peak shear displacement (i.e. $|\bar{t}^{con}| > \sigma_u$), the dilation will be set to zero. An additional assumption is that the dilation along a joint is irreversible after slip. Therefore, the dilation at a rock joint will remain constant after a certain shear displacement is exceeded.

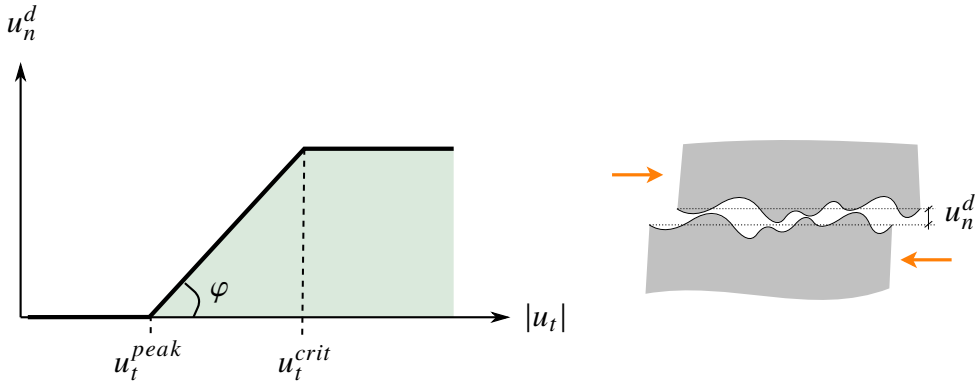

(a) Dilation constitutive model (b) Average dilation along fracture surface

Figure 2.4: Linear dilation constitutive model and sketch of average dilation, u_n^d, along rough fracture surface

2.4 XFEM discretization

The extended finite element method (XFEM) is used in this study to discretize natural fractures separately from the solid rock mass. This method simplifies meshing of the solid rock matrix

around arbitrary fracture geometries, reduces mesh dependency on the fracture network, and eliminates the need for remeshing as fractures grow. The discontinuous displacement field is approximated by adding additional degrees of freedom in the solid mesh at nodes surrounding the fractures.

In this work, the fracture network is known *a priori*. In practice, where the fracture network is not available, a fracture network must be simulated using available data so that the generated fractures represent the real reservoir conditions. This may be based on knowledge of fracture density and preferential fracture orientation from cores. Work on fracture network characterization has been performed by various researchers [95, 96].

2.4.1 Explicit and implicit definition of fracture network

The solid domain is discretized into quadrilateral elements, and the fractures are defined using linear segments that span between edges of the solid mesh elements, as depicted in Figure 2.5. These fracture segments are each defined by separate normal, $\hat{\mathbf{n}}_{\Gamma_c}$ and tangential vectors, $\hat{\mathbf{e}}_{\Gamma_c}$.

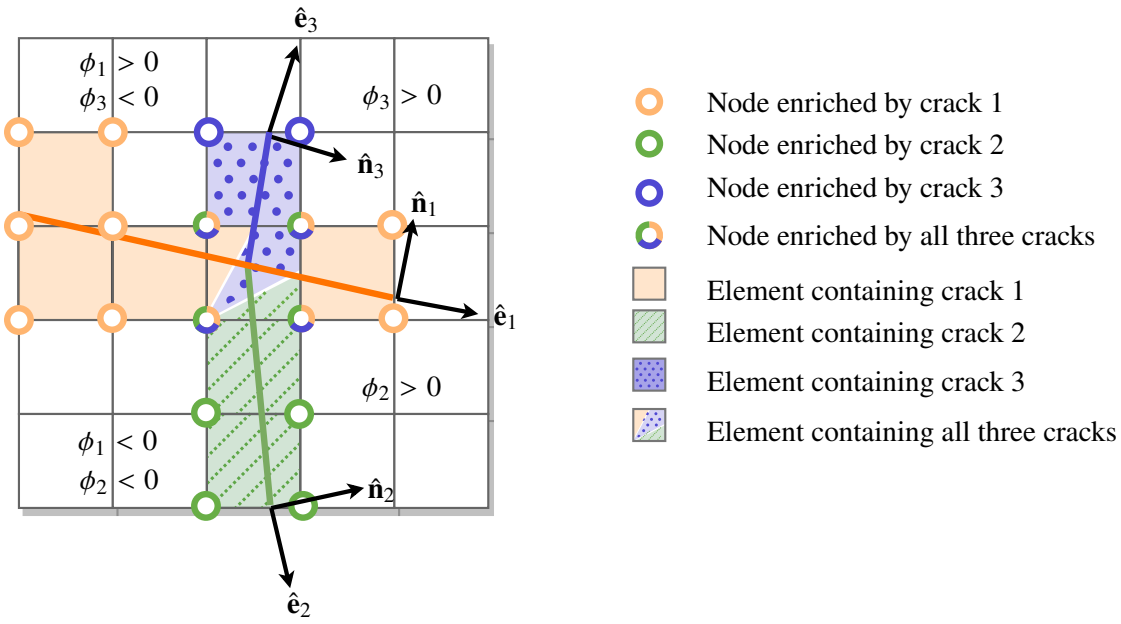

Figure 2.5: Enriched nodes on XFEM mesh with multiple fractures

To facilitate the enrichment of intersecting fractures (as described in Section 2.4.4), fractures must be separated into main fractures (which extend through an intersection), and secondary fractures (which are cut along an intersection). This is done by looping through each fracture, and successively separating it into two parts at the junction if it is cut by any of the preceding

fractures processed in the loop. Each of these fractures is then stored in memory, along with its normal and tangential vectors, fracture tip, and length. An example of a fracture network and its separation into main and secondary fractures is depicted in Figure 2.6.

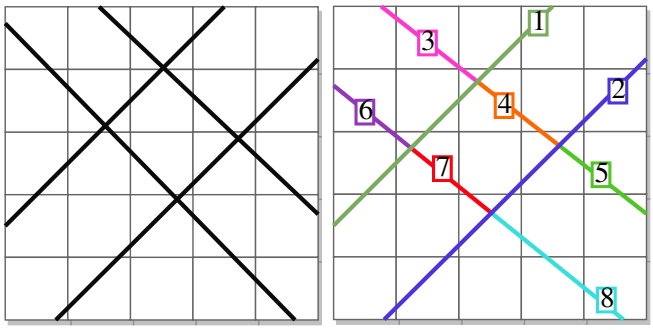

Figure 2.6: Global crack separation

Using the explicit definition of the fracture, an implicit description of the fracture network is defined in the solid domain by two level-set functions for each fracture, ϕ_c and ψ_c. The level-set functions define the signed distance between a location along the domain, $\mathbf{x}$, and the tip of the discontinuity, $\mathbf{x}^{tip}_{\Gamma_c}$, in the direction normal and tangential to the fracture, respectively. These level-set functions are evaluated at each of the solid mesh nodes to simplify the definition of the enriched nodes and enrichment functions, as described in Section 2.4.3.

$$\begin{aligned} \phi_c(\mathbf{x}) &= \left(\mathbf{x} - \mathbf{x}^{tip}_{\Gamma_c}\right) \cdot \hat{\mathbf{n}}_{\Gamma_c} \\ \psi_c(\mathbf{x}) &= \left(\mathbf{x} - \mathbf{x}^{tip}_{\Gamma_c}\right) \cdot \hat{\mathbf{e}}_{\Gamma_c} \end{aligned} \tag{2.16}$$

2.4.2 Approximation

The displacement field is approximated by a discontinuous function, defined by enriching the shape functions at nodes that are adjacent to fractures in the domain. For each element, the approximation of the displacement field is expressed as

$$\begin{aligned} \mathbf{u}^h(\mathbf{x},t) &= \sum_{I\in S_n} N_I(\mathbf{x})\tilde{\mathbf{u}}_I(t) + \sum_{c\in S_c}\left(\sum_{J\in S_{nc}} N_J(\mathbf{x})\Psi^c_J(\mathbf{x})\tilde{\mathbf{a}}^c_J(t)\right) \\ &\equiv \mathbf{N}_u(\mathbf{x})\hat{\mathbf{u}}(t) + \mathbf{N}_a(\mathbf{x})\hat{\mathbf{a}}(t) \\ &\equiv \begin{bmatrix}\mathbf{N}_u(\mathbf{x}) & \mathbf{N}_a(\mathbf{x})\end{bmatrix}\begin{bmatrix}\hat{\mathbf{u}}(t)\\ \hat{\mathbf{a}}(t)\end{bmatrix} = \mathbf{N}(\mathbf{x})\mathbf{d}(t) \end{aligned} \tag{2.17}$$

in which S_n is the set of all nodes in each element, S_c is the set of fractures in the domain, and S_{nc} is the set of nodes that have a nodal support cut by fracture c. An example showing the set of nodes that are enriched for two fractures in a domain is shown in Figure 2.5. For each node, I, the standard finite element shape functions are denoted by N_I and the enrichment functions for fracture c are denoted by $\Psi_I^c(\mathbf{x})$. The vectors of nodal displacements on the standard degrees of freedom and degrees of freedom enriched on node I by fracture c are denoted by $\tilde{\mathbf{u}}_I(t)$, and $\tilde{\mathbf{a}}_I^c(t)$, respectively. This enrichment function is described in further detail in Section 2.4.4.

In matrix form, the shape functions corresponding to the standard degrees of freedom are denoted by $\mathbf{N}_u$, and the enriched shape functions corresponding to the enriched degrees of freedom for all fractures are compiled into a matrix and denoted by $\mathbf{N}_a$. Likewise, the nodal displacements for the standard and enriched degrees of freedom are combined into column matrices $\hat{\mathbf{u}}$ and $\hat{\mathbf{a}}$, respectively. The formulation can be rewritten to simplify computations by creating a matrix that contains both the standard and enriched shape functions, $\mathbf{N}(\mathbf{x})$, and a column matrix that contains the displacements on both the standard and enriched degrees of freedom, $\mathbf{d}(t)$. The time derivatives of the displacement field (velocity and acceleration) are approximated similarly.

Using the approximation, the jump in the displacement field can then be defined in terms of the enriched degrees of freedom as

$$\begin{aligned}
[\![\mathbf{u}^h(\mathbf{x})]\!] &= \mathbf{u}^h(\mathbf{x}^+) - \mathbf{u}^h(\mathbf{x}^-) \\
&= \sum_{c\in S_c}\left(\sum_{J\in S_{nc}} \mathbf{N}_J(\mathbf{x})\left(\Psi_J^c(\mathbf{x}^+) - \Psi_J^c(\mathbf{x}^-)\right)\tilde{\mathbf{a}}_J^c(t)\right) \\
&\equiv \left[\mathbf{N}_a(\mathbf{x}^+) - \mathbf{N}_a(\mathbf{x}^-)\right]\hat{\mathbf{a}}(t)
\end{aligned} \tag{2.18}$$

The strain, or spatial derivative of the displacement field, is approximated by

$$\begin{aligned}
\boldsymbol{\varepsilon}^h = \nabla^s\mathbf{u}^h(\mathbf{x},t) &= \sum_{I\in S_n}\nabla^s N_I(\mathbf{x})\tilde{\mathbf{u}}_I(t) + \sum_{c\in S_c}\left(\sum_{J\in S_{nc}}\nabla^s N_J(\mathbf{x})\Psi_J^c(\mathbf{x})\tilde{\mathbf{a}}_J^c(t)\right) \\
&\equiv \mathbf{B}_u(\mathbf{x})\hat{\mathbf{u}}(t) + \mathbf{B}_a(\mathbf{x})\hat{\mathbf{a}}(t) \\
&\equiv \begin{bmatrix}\mathbf{B}_u(\mathbf{x}) & \mathbf{B}_a(\mathbf{x})\end{bmatrix}\begin{bmatrix}\hat{\mathbf{u}}(t)\\ \hat{\mathbf{a}}(t)\end{bmatrix} = \mathbf{B}(\mathbf{x})\mathbf{d}(t)
\end{aligned} \tag{2.19}$$

in which $\mathbf{B}_u$ and $\mathbf{B}_a$ are the derivatives of the shape functions corresponding to the standard and enriched degrees of freedom, respectively, and $\mathbf{B}$ is a matrix that contains the derivatives of the shape functions for both the standard and enriched degrees of freedom.

2.4.3 Identification of enriched nodes

Nodes of the solid mesh that have their nodal support cut by a fracture are enriched with extra degrees of freedom for that fracture. The process of enriching nodes begins by searching through each element to identify which elements contain a part of the fracture, and then adding enriched degrees of freedom to all nodes in the element. Three criteria based on the level-set functions at the element nodes are used to identify if a fracture is cut. The element is intersected by a fracture if the minimum and maximum normal level sets have opposite sign, and if the minimum and maximum tangential level sets are greater than the fracture length and less than zero, respectively. The criteria are defined with respect to all nodes I in the element,

$$\max(\phi_c(\mathbf{x}_I)) \min(\phi_c(\mathbf{x}_I)) \leq 0 \tag{2.20}$$

$$\max(\psi_c(\mathbf{x}_I)) \leq 0 \tag{2.21}$$

$$\min(\psi_c(\mathbf{x}_I)) \geq -L_c \tag{2.22}$$

in which L_c is the fracture length.

There are various cases around the fracture tip in which these criteria are not sufficient to properly identify an element with a fracture in it. An example of this is given in Figure 2.7, in which the top-right element meets the criteria for enriched element detection but does not contain the fracture. For this reason, it is necessary to add a criterion for elements around the fracture tip. If the element possibly contains a fracture tip (i.e. $\min(\psi_c(\mathbf{x}_I)) \max(\psi_c(\mathbf{x}_I)) \leq 0$ or $\min(\psi_c(\mathbf{x}_I)) \leq -L_c$ and $\max(\psi_c(\mathbf{x}_I)) \geq -L_c$), then the explicit fracture mesh must be checked to ensure that the tip is in fact located inside the element.

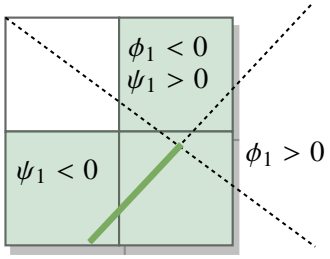

Figure 2.7: Erroneous detection of enriched element with criteria based on level-set functions. The top-right element is detected as enriched but does not contain a fracture

2.4.4 Enrichment function

To model discontinuities in the displacement field, a shifted Heaviside enrichment function is used at each node, J, defined as

$$\Psi_J^c(\mathbf{x}) = H_c(\mathbf{x}) - H_c(\mathbf{x}_J) \tag{2.23}$$

in which $H_c(\mathbf{x})$ is the Heaviside step function that differentiates between the two sides of fracture c,

$$H_c(\mathbf{x}) = H(\phi_c(\mathbf{x})) = \begin{cases} 0 & \text{if } \phi_c(\mathbf{x}) < 0 \\ 1 & \text{if } \phi_c(\mathbf{x}) \geq 0 \end{cases} \tag{2.24}$$

The Heaviside enrichment at each node is shifted by the Heaviside function evaluated at the corresponding node to satisfy the Kronecker-δ property.

For a single fracture or multiple, non-intersecting fractures in an element, the enrichment function above is sufficient to capture the discontinuity. Another case that is encountered in this study is the intersection of fractures within an element. Daux *et al.* [97] proposed that an element with two intersecting fractures must have three sets of enriched nodes to satisfy rigid body motions for each of the four independent blocks that are created by the junction. To accomplish this, each element with an intersection is enriched by three fractures–the main fracture and two secondary fractures. This formulation relies on the initial separation into main and secondary fractures described in Section 2.4.1. For each secondary fracture, it is necessary to keep track of all the main fractures that cut it. All nodes, J, which have a nodal support cut by a secondary fracture are enriched with the following function,

$$\Psi_J^c(\mathbf{x}) = J_c(\mathbf{x}) - J_c(\mathbf{x}_J) \tag{2.25}$$

The function $J_c(\mathbf{x})$ is the junction enrichment function which is taken as a modification of that proposed by Zi *et al.* [38] and Daux *et al.* [97]. For enrichment of a given fracture c, this function simplifies to the Heaviside enrichment function when evaluated on the same side of the main fracture which intersects it.

$$J_c(\mathbf{x}) = \begin{cases} H_c(\mathbf{x}) & \text{for } \phi_c(\mathbf{x})\phi_m(\mathbf{x}_c) > 0\,, \forall m \in S_{mc} \\ 0 & \text{otherwise} \end{cases} \tag{2.26}$$

In this function, the subscript c refers to the secondary fracture and S_{mc} is the set of main fractures that cut secondary fracture c. The location $\mathbf{x}_c$ is an arbitrary point on the secondary fracture. The junction function is applied on all enriched nodes for secondary fractures, and not only on

the junction elements, as done in previous works. For enriched nodes that are not directly in the junction element, the junction function will be the same as the Heaviside function.

Using these definitions of enrichment functions the approximation (Equation 2.17) can be rewritten as

$$\begin{aligned}\mathbf{u}^h(\mathbf{x},t) = &\sum_{I\in S_n} N_I(\mathbf{x})\tilde{\mathbf{u}}_I(t) + \sum_{c\in S_m}\left(\sum_{J\in S_{nc}} N_J(\mathbf{x})\left[H_c(\mathbf{x}) - H_c(\mathbf{x}_J)\right]\tilde{\mathbf{a}}_J^c(t)\right) \\ &+ \sum_{c\in S_s}\left(\sum_{J\in S_{nc}} N_J(\mathbf{x})\left[J_c(\mathbf{x}) - J_c(\mathbf{x}_J)\right]\tilde{\mathbf{a}}_J^c(t)\right)\end{aligned} \tag{2.27}$$

in which S_m is the set of all main fractures in the domain, and S_s is the set of all secondary fractures in the domain, as described in Section 2.4.1. An example showing the enrichment functions for intersecting fractures in an element is depicted in Figure 2.8. It can be seen that the Heaviside function is used to enrich the main fracture, and junction enrichments are used to enrich the secondary fractures. In the non-shaded areas of the figures, the enrichment functions have a value of zero.

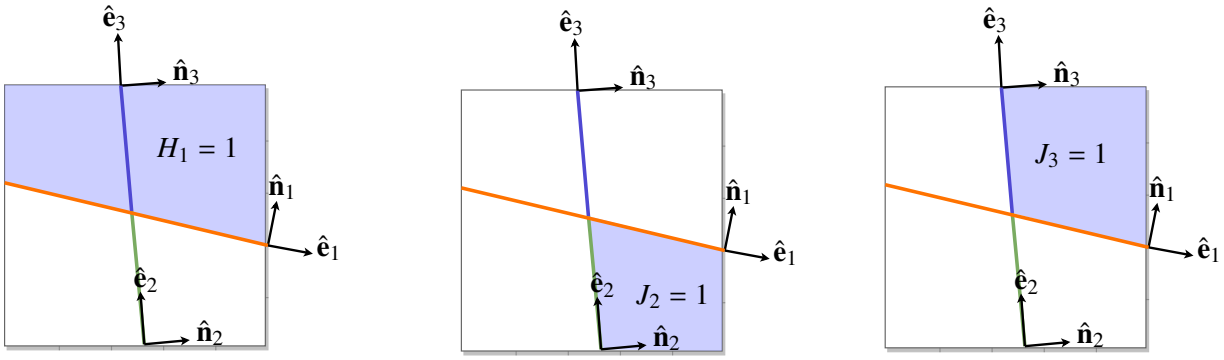

Figure 2.8: Enrichment functions for an element with intersecting fractures

2.4.5 Discretization

Following the standard procedure, the semi-discretized equations are obtained by inserting the approximation (2.17) and a test function of a similar form into the weak form of the governing equation (2.4). The weak form is

$$\underbrace{\left[\int_{\Omega} \rho \mathbf{N}^T \mathbf{N} d\Omega\right] \ddot{\mathbf{d}}}_{\mathbf{F}^{kin}} + \underbrace{\int_{\Omega} \mathbf{B}^T \{\sigma\} d\Omega}_{\mathbf{F}^{int}} = \underbrace{\left[\int_{\Omega} \mathbf{N}^T \mathbf{b} d\Omega + \int_{\Gamma_t} \mathbf{N}^T \bar{\mathbf{t}} d\Gamma\right]}_{\mathbf{F}^{ext}} + \underbrace{\sum_c \int_{\Gamma_c} \mathbf{N}^T \bar{\mathbf{t}}^c d\Gamma}_{\mathbf{F}^c} \tag{2.28}$$

The semi-discrete system of equations is

$$\mathbf{M}\ddot{\mathbf{d}} + \mathbf{C}\dot{\mathbf{d}} + \mathbf{K}\mathbf{d} = \mathbf{F}^{ext} + \mathbf{F}^c \tag{2.29}$$

in which the contribution from kinetic forces is denoted by $\mathbf{F}^{kin} = \mathbf{M}\ddot{\mathbf{d}}$. A viscous damping term, $\mathbf{F}^{damp} = \mathbf{C}\dot{\mathbf{d}}$, is included in the system of equations. A mass-proportional damping matrix is assumed, such that $\mathbf{C} = c\mathbf{M}$. The contribution from internal forces is denoted by $\mathbf{F}^{int} = \mathbf{K}\mathbf{d}$. The column matrix of external forces, $\mathbf{F}^{ext}$, are due to the external tractions, $\bar{\mathbf{t}}$, and body forces, $\mathbf{b}$. The column matrix of forces along the fractures, $\mathbf{F}^c$, are due to tractions along the fracture surfaces, $\bar{\mathbf{t}}^c$. The semi-discrete equations are integrated in time using an explicit time integration method, which is described in more detail in Section 2.5.

The evaluation of the stiffness and mass matrices requires integration over discontinuous element domains and the various fracture surfaces. Domain integration over discontinuous elements is performed by splitting the elements into sub-triangles in the normal XFEM way [34, 44, 50].

2.5 Solution method

The solution of the semi-discrete equation (2.29) is obtained in this study using a dynamic relaxation scheme with explicit time integration. In this section, a description of the solution method is provided.

Implicit methods with a Newton-Raphson iterative solver are commonly used to solve equilibrium problems. For linear transient problems, this method has the distinct advantage of unconditional stability. However, this stability is not proven for nonlinear systems, and convergence of the method often fails in the vicinity of unstable states, such as when a fracture is on the border of contact/separation states [98]. The interface constitutive models employed in this study are non-smooth functions of the displacements: contact/separation, sharp kink before softening of the cohesive forces, stick/slip behavior, and non-smoothness in the dilation behavior which in turn affects the contact traction-separation law. As a result, implicit Newton strategies may lack the robustness to solve this problem under all loading conditions. Additionally, the linearization of the forces along the fractures are cumbersome to derive for the nonlinear relationships of these forces to the displacements, and other history variables. For this reason, many discrete element method codes implement an explicit time integration method, as is the case in this paper.

A dynamic relaxation (DR) scheme is used, as described in more detail in this section. Using this algorithm, Equation (2.29) is solved with certain mass (**M**) and damping (**C**) matrices so that the solution converges to the following quasi-static equation

$$\mathbf{Kd} = \mathbf{F}^{ext} + \mathbf{F}^{c} \tag{2.30}$$

2.5.1 Dynamic relaxation scheme

The selection of density and damping parameters such that the dynamic problem converges to a quasi-static solution is performed through a dynamic relaxation algorithm [99, 100]. This algorithm adjusts the mass and damping of the system to achieve a static solution. The algorithm is as follows,

1. Initialize $\mathbf{d}^0$, $\dot{\mathbf{d}}^{-1/2}$, $\mathbf{F}^{int}$, $\mathbf{M}$, c, and Δt
2. $\ddot{\mathbf{d}}^n = \mathbf{M}^{-1}\left(\mathbf{F}^{ext} + \mathbf{F}^{c} - \mathbf{F}^{int}\right)$
3. $\dot{\mathbf{d}}^{n+1/2} = \left(\frac{2 - c\Delta t}{2 + c\Delta t}\right)\dot{\mathbf{d}}^{n-1/2} + \left(\frac{2\Delta t}{2 + c\Delta t}\right)\ddot{\mathbf{d}}^n$
4. $\mathbf{d}^{n+1} = \mathbf{d}^n + \Delta t\dot{\mathbf{d}}^{n+1/2}$
5. Calculate $\mathbf{F}^{int}(\mathbf{d}^{n+1})$, $\mathbf{F}^{c}(\mathbf{d}^{n+1})$, $\mathbf{M}$ (2.32), and c (2.33)
6. Check convergence (2.36-2.37)
7. If not converged, repeat steps 2-6

The explicit scheme is conditionally stable. To meet the Courant-Friedrichs-Lewy (CFL) condition, the time step used in the system must stay below a critical value, defined as

$$\Delta t \leq \frac{2}{\omega_{max}} \tag{2.31}$$

in which ω_{max} is the highest frequency of the system. In the algorithm used, the time step is user-defined and the highest frequency of the system is adjusted to meet the CFL condition. Although a dynamic equation is solved explicitly, time steps do not represent physical time but rather a way to progress through the quasi-static solution. An upper bound approximation using Gerschgorin's theorem gives the highest frequency of the system with respect to the mass and stiffness matrices. Using the upper bound approximation for the maximum frequency and a prescribed time step size, the system mass matrix is approximated as

$$M_{ii} = \frac{\Delta t^2}{4} \sum_j |\bar{K}_{ij}| \tag{2.32}$$

in which $\bar{\mathbf{K}}$ is the stiffness matrix approximation described below. The mass matrix definition from equation (2.28) is no longer used in the algorithm.

A damping term is added to the system of equations, equal to $\mathbf{C}\dot{\mathbf{d}}$. The mass-proportional damping matrix is defined as $C_{ii} = cM_{ii}$. The damping parameter, c, is defined with respect to the minimum natural frequency of the system.

$$c = 2\omega_{min} \tag{2.33}$$

Using the Rayleigh quotient to estimate the minimum eigenvalue of the system, the minimum natural frequency is estimated in each time step as

$$\omega_{min} = \left[\frac{(\dot{\mathbf{d}}^{n-1/2})^\top \bar{\mathbf{K}}^n \dot{\mathbf{d}}^{n-1/2}}{(\dot{\mathbf{d}}^{n-1/2})^\top \mathbf{M} \dot{\mathbf{d}}^{n-1/2}} \right]^{1/2} \tag{2.34}$$

in which an approximation of the term $\bar{\mathbf{K}}^n \dot{\mathbf{d}}^{n-1/2}$ is given as:

$$\bar{\mathbf{K}}^n \dot{\mathbf{d}}^{n-1/2} = \frac{\left(\mathbf{F}_{int}^n - \mathbf{F}_c^n\right) - \left(\mathbf{F}_{int}^{n-\frac{1}{2}} - \mathbf{F}_c^{n-\frac{1}{2}}\right)}{\Delta t} \tag{2.35}$$

Convergence of the algorithm is based on both displacement- and residual-based criteria, although it is noted that the residual-based criterion often governs. The criteria are

$$||\mathbf{d}^{n+1} - \mathbf{d}^n|| \leq \epsilon_u ||\mathbf{d}^n|| \tag{2.36}$$

$$||\mathbf{r}^{n+1}|| \leq \epsilon_r \max(||\mathbf{F}_{ext}^{n+1}||, ||\mathbf{F}_{int}^{n+1}||, ||\mathbf{F}_c^{n+1}||) \tag{2.37}$$

in which $\mathbf{r}^{n+1} = \mathbf{F}_{kin}^{n+1} + \mathbf{F}_{damp}^{n+1}$. The first condition is met when the percent change in the displacement norm is below a small threshold value, ϵ_u. The second condition is met when the residual norm, defined by the transient terms in the system and normalized by the dominating steady-state forces, is below a small threshold value, ϵ_r. In the problems described in Section 2.6, the tolerances are defined as $\epsilon_u = 1 \times 10^{-4}$, and $\epsilon_r = 1 \times 10^{-5}$.

2.6 Numerical results

This section shows the application of the model to a few problems with naturally fractured rock. To verify the implementation of the constitutive model described in Section 2.3, a shear test is simulated under various loading stresses. The convergence of the model with multiple fractures is studied through a simulation of a biaxial test. Finally, application to a larger scale problem is shown through simulation of loading on a naturally fractured slope. All of the examples use the material properties presented in Table 2.1.

Table 2.1: Material properties for simulations of discrete fracture networks

Young's modulus	E	65	GPa
Poisson's ratio	ν	0.2	
Density	ρ	2.7	g/cm^3
Fracture energy	G_{Ic}	1	J/m^2
Tensile strength	f_u	100	kPa
Cohesion weakening aperture	u_n^{max}	0.0801	mm
Fracture separation aperture	u_n^{sep}	0.01	mm
Unconfined compressive strength	σ_u	100	MPa
Critical slip	u_t^{crit}	12.5	mm
Friction angle	ϕ	32	°
Cohesive shear strength	c_f	100	kPa
Dilation angle	φ	5	°

2.6.1 Shear test

A direct shear test on a 100 mm × 150 mm × 100 mm rock specimen is simulated. The specimen contains a weak plane, i.e., natural joint, passing through the specimen in the middle of its longest dimension as illustrated in Figure 2.9a. A two-dimensional uniform structured mesh of 2601 four-node quadrilateral elements with an average effective mesh size of 2.45 mm is employed to analyze the 100 mm × 150 mm plane of study shown in Figure 2.9b under plane strain conditions. A normal stiffness of k_n =10 GPa/mm and a shear stiffness of k_t = 5 GPa/mm are assumed for the contact behavior along the interface.

The shear test is repeated for four different values of normal stress ranging from 20 MPa to 100 MPa. Each test is carried out by imposing a total horizontal displacement of 60 mm, in equal 3 mm increments, to the upper half of the specimen while the specimen is under specified normal stress, σ_y, applied on its top surface. The bottom edge of the specimen is assumed to be fixed in both x- and y-directions. Upon the start of each test, the horizontal displacement from the

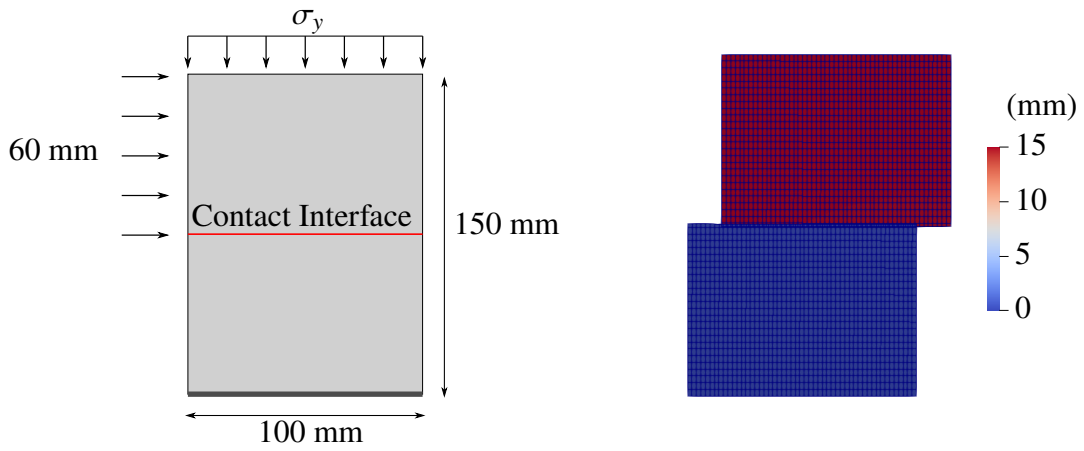

(a) Shear test schematic

(b) Horizontal displacement contour

Figure 2.9: Schematic of shear test specimen (left), and horizontal displacement contour on deformed mesh (right)

previous test is reset to zero and the normal stress is increased to the designated normal stress of the current test. Shear stress, shear deformation, and shear dilation are measured along the joint during each stage of the test. This problem does not conform to the requirements for small displacements and should be performed with contact node detection. However, this simulation is performed under the assumption of small deformations for verification of the interface constitutive model only.

Figure 2.10a illustrates the stress-deformation curves of the specimen under shear stresses generated by the imposed shear displacement under four different normal stresses. The figure is generated by averaging the shear stress at each quadrature point along the fracture. It shows that shear stress on the interface increases linearly to the value of the peak shear strength, τ_{crit}, of the jointed rock specimen as shear displacement is applied with a constant rate. Upon reaching the critical stress, the specimen shows no additional resistance against the shear displacement and the stress-strain curve plateaus. Such a plateau is expected since the effect of asperities (or surface roughness) along the interface is modeled by an average dilation angle which does not take into account the stress drop due to the resolution of asperities on the shearing interface. Figure 2.10a also shows that the magnitude of the normal stress directly affects the shear strength of the specimen. In other words, the specimen shows a higher shear strength along the joint in tests which are carried out under higher normal stresses.

In contrast with the shear strength curve, Figure 2.10b shows that the average dilation of the specimen under direct shearing decreases as the normal stress on the interface increases from 20 MPa to 80 MPa. As seen in the figure, the shear displacement under which dilation initiates (i.e., the point at which the interface starts to slip) and the amount of dilation itself are functions

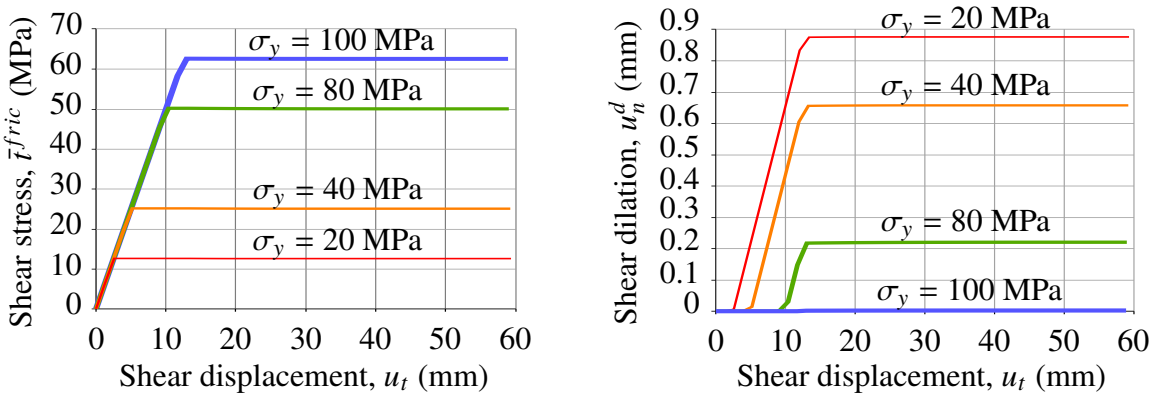

(a) Shear stress (b) Shear dilation

Figure 2.10: Shear stress (left) and shear dilation (right) along crack throughout shear test

of the normal stress, σ_y. In the fourth test in which the normal stress, σ_y = 100 MPa, is equal to the unconfined compressive strength of the specimen, σ_u, the model shows no dilation on the interface as shear displacement increases from zero to its maximum value. Physically, this represents local shearing of asperities along the rough surface, instead of dilation along them.

The analytical Mohr-Coulomb failure surface and the failure point associated with each of the four tests are depicted in Figure 2.11. The dashed line in the figure represents the analytical Mohr-Coulomb failure surface for the values of friction angle and cohesion provided in Table 2.1, which verifies the values obtained from the numerical model using the interface constitutive laws, (2.13) and (2.14) with the same parameters.

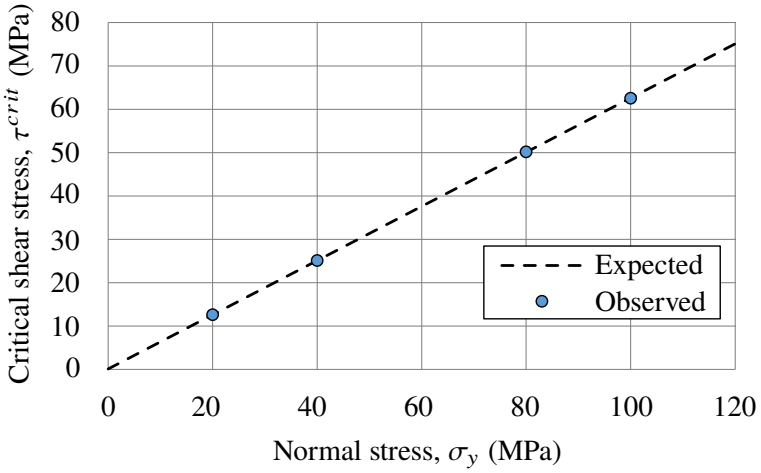

Figure 2.11: Critical shear stress vs. normal stress for shear test specimen

2.6.2 Biaxial test of a rock mass with a DFN

A biaxial test on a 100 mm × 100 mm × 100 mm specimen from a naturally fractured rock sample is simulated. The specimen is assumed to contain two sets of dominant natural fractures as shown in Figure 2.12a. The top and the right edges of the specimen are considered to be fixed in the vertical and horizontal directions, respectively. An external load is applied on the left and bottom edges of the specimen by imposing displacements in x- and y-directions. The plane of analysis is assumed to be under a plane strain condition, and the normal and tangential stiffnesses along fracture interfaces are set to $k_n = 1.0 \times 10^4$ GPa/m and $k_t = 5.0 \times 10^3$ GPa/m respectively.

Applied displacements are chosen to correspond to an equivalent stress state with a ratio of horizontal and vertical stresses, $K = \sigma_x/\sigma_y$. Initially, isotropic confining stresses are applied on the specimen with $K = 1$. The shear stress on the specimen is monotonically increased by decreasing K until failure occurs, reducing σ_x while maintaining σ_y constant. A sample mesh of 400 elements in its deformed shape is presented in Figure 2.12b.

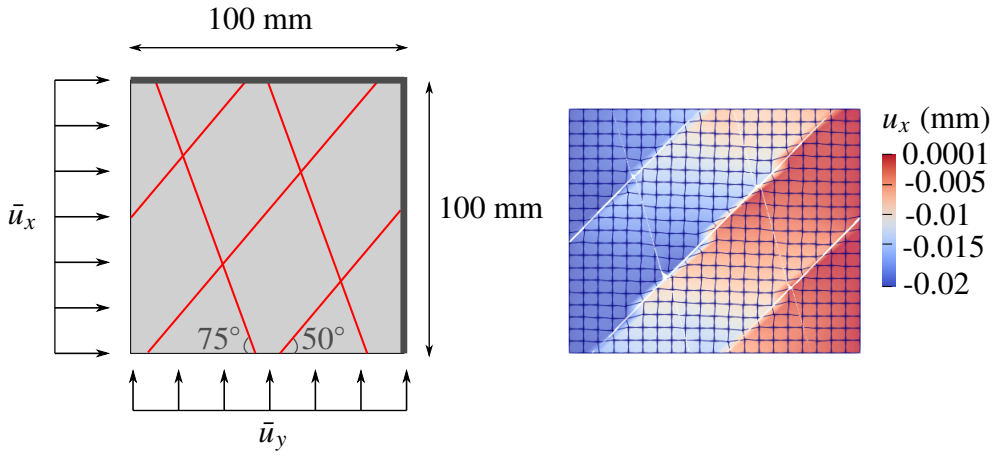

(a) Biaxial test schematic

(b) Horizontal displacement contour

Figure 2.12: Schematic of biaxial test on jointed rock specimen (left), and horizontal displacement contour on structured mesh of 400 linear quadrilateral elements in deformed state using the XFEM-DFN model (right)

Figure 2.13 presents the failure scenario along the fractures in the specimen as the stress ratio changes from $K > 0.28$ to $K = 0.1$, in which sections of the fracture in blue represent parts of the fracture that have yielded. The first evidence of failure is detected along the fracture set oriented 50° from horizontal at $K = 0.28$. Decreasing the stress ratio, the second set of fractures (oriented 75° from horizontal) begins to fail at $K = 0.19$.

Dilation along fractures is expected to follow a similar pattern as the shear displacement in Figure 2.13 due to the proportionality of the dilation and shear displacements in the constitutive

model. Figure 2.14 shows the amount of dilation along the fractures for various stages of loading. The average dilation along fractures oriented 75° from horizontal is lower than the other set of fractures, since the former undergoes smaller shear displacements after failure compared to the latter. The simulation is performed in 20 load steps, with each load step taking between 100 and 2000 iterations to converge to a quasi-static solution. The load steps near the end of the simulation take more iterations to reach equilibrium than the initial load steps since the shear stress acting on the fracture surfaces increases the area of the fracture surfaces yielding and undergoing dilation.

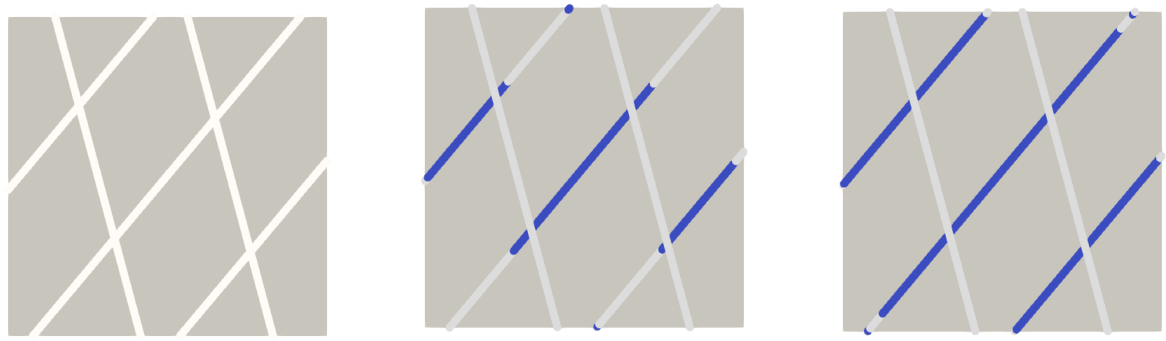

(a) $K < 0.28$ (b) $K = 0.28$ (c) $K = 0.235$

(d) $K = 0.19$ (e) $K = 0.145$ (f) $K = 0.1$

Figure 2.13: Slip (represented in blue) along fractures at various loading stages of a rock mass with a DFN

To study convergence of the numerical solution, seven different meshes of bilinear quadrilateral elements are studied. A failure curve represented by the global differential stress versus the vertical strain is shown in Figure 2.15 for the various meshes. It can be seen that as the average effective mesh size is decreased, the softening branch of the stress-strain curve is captured with higher precision. The curve is similar for all meshes during the initial loading before yielding and varies depending on the mesh size after the yield point. The converged failure curve shows a softening behavior. As K decreases, the average normal stress on the specimen is reduced, which also decreases the differential stress (a measure of shear stress) after the specimen has yielded.

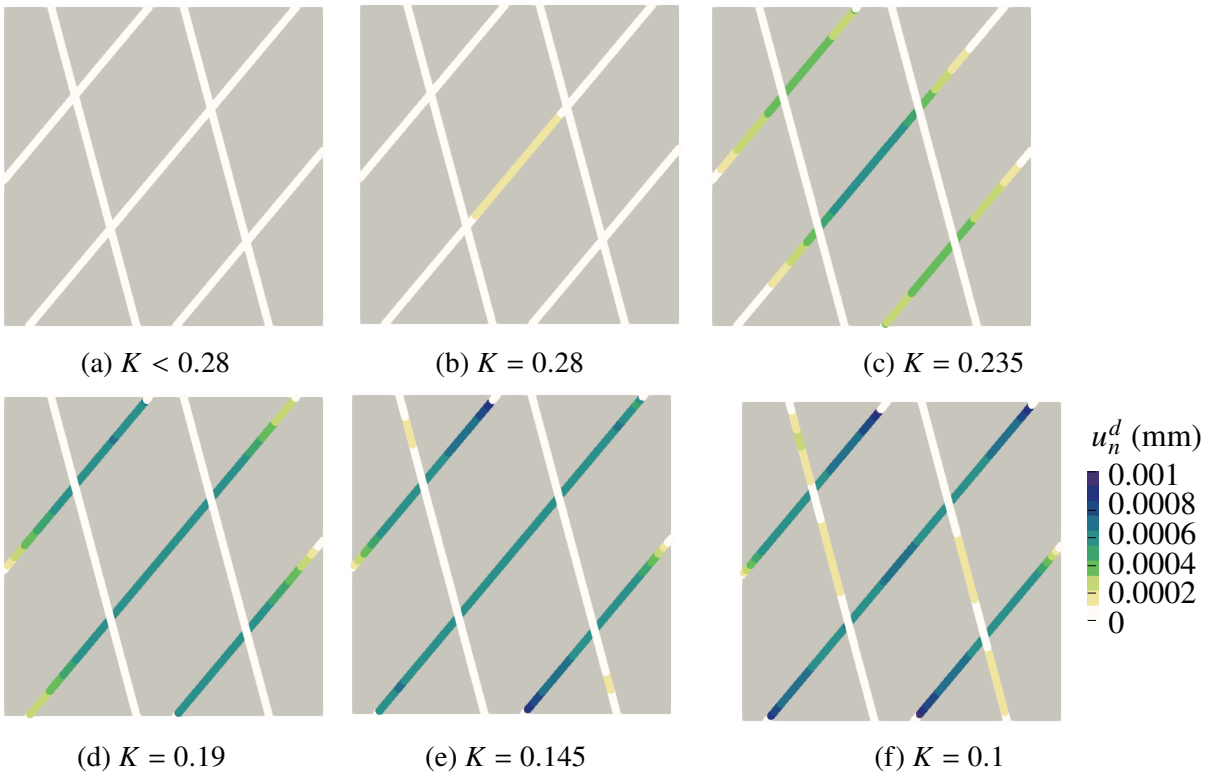

(a) $K < 0.28$ (b) $K = 0.28$ (c) $K = 0.235$

(d) $K = 0.19$ (e) $K = 0.145$ (f) $K = 0.1$

Figure 2.14: Shear dilation along fractures at various loading stages of a rock mass with a DFN

The horizontal displacement contours at $K = 0.1$ for the seven meshes are shown in Figure 2.16. These also show to be converging with smaller element sizes for each mesh.

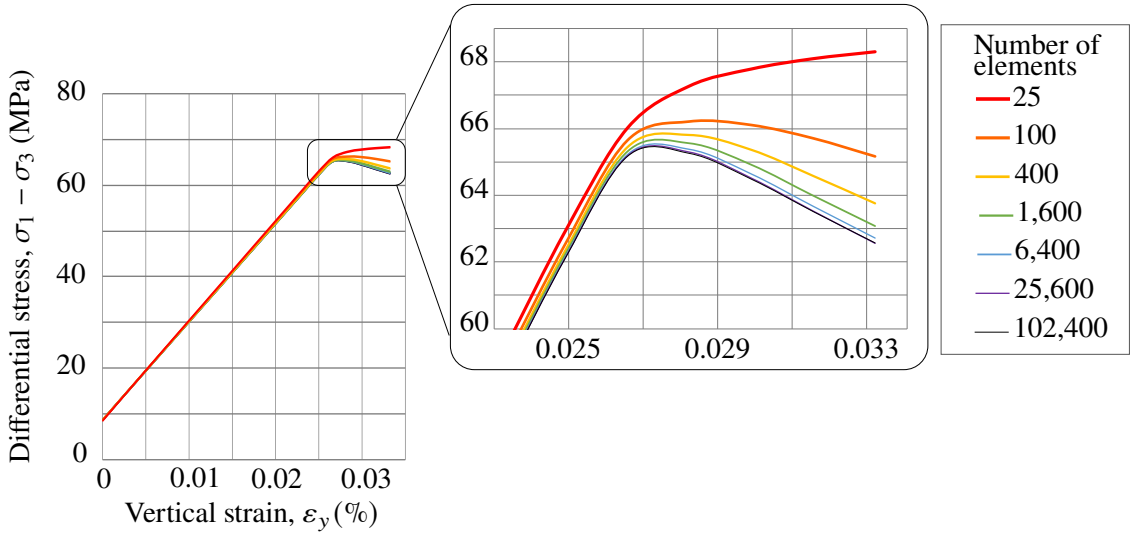

Figure 2.15: Differential stress vs vertical strain of the fractured rock specimen during biaxial loading for various mesh sizes

2.6.3 Stability of a rock slope containing a DFN

A naturally fractured rock slope with two perpendicular dominant fracture sets is simulated in this example to demonstrate the capability of the numerical model in simulating multiple interacting contact surfaces on a large scale.

Figure 2.17a shows the geometry of the slope, which is loaded on its top edge and considered to be confined in the horizontal direction on its left and right edges. The bottom edge of the slope is also assumed to be fixed in both horizontal and vertical directions. The natural fracture network is represented by a set of five parallel fractures with a 22 m spacing and an inclination angle of 50 degrees from the horizontal, along with a set of six fractures perpendicular to the first set with the same spacing (total of 11 fractures) as depicted in Figure 2.17a.

Numerical analysis is performed using an unstructured mesh of 3784 bilinear quadrilateral elements with an average effective mesh size of 1 m. A normal stiffness of $k_n = 10$ GPa/m and a tangential stiffness of $k_t = 1$ GPa/m are set for the constitutive model of the fractures. The slope is initially under gravitational loads from its weight. A monotonically increasing external load is applied along a 5 m span on the top edge of the model in equal increments of $\Delta\bar{t}_y = 0.38$ MPa until the slope fails (failure occurs at $\bar{t}_y = 14.4$ MPa in this case). The deformed configuration

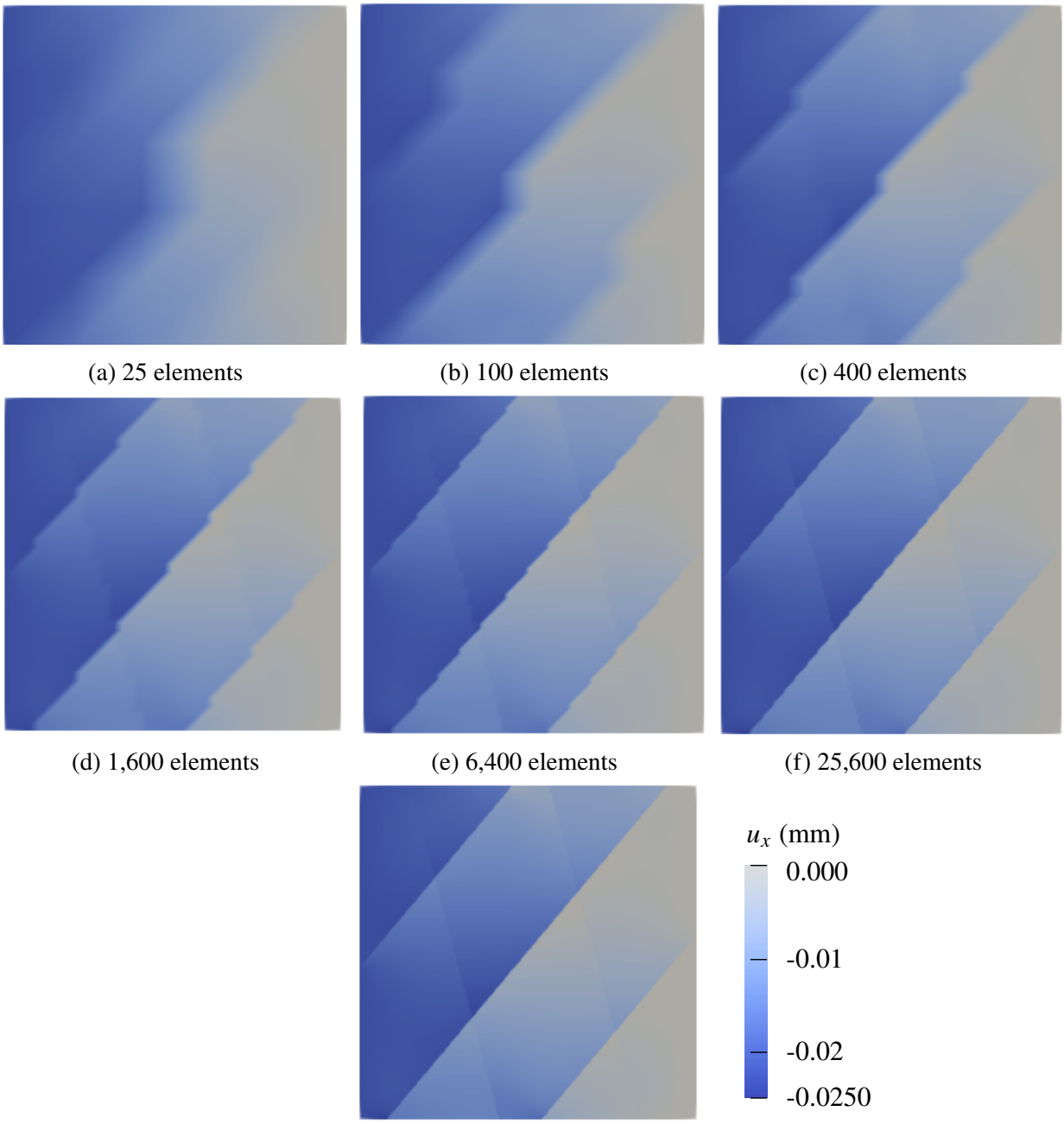

(a) 25 elements (b) 100 elements (c) 400 elements

(d) 1,600 elements (e) 6,400 elements (f) 25,600 elements

(g) 102,400 elements

Figure 2.16: Horizontal displacement contours for various mesh sizes during a biaxial test

of the numerical mesh and the contours of vertical displacement in the model are shown at the moment of failure in Figure 2.17b.

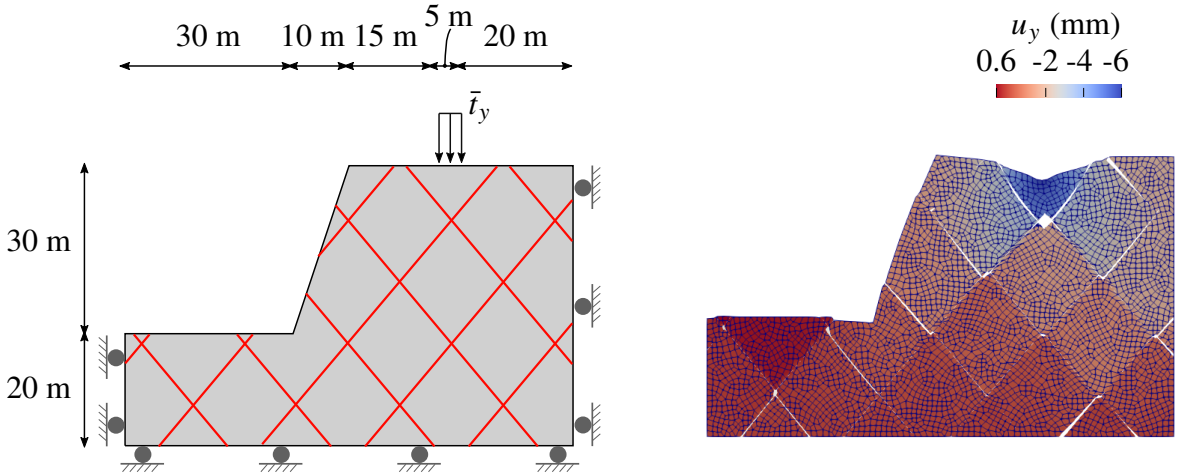

(a) Rock slope schematic

(b) Vertical displacement contours

Figure 2.17: Schematic of loading on fractured rock slope (left) and vertical displacement contours on deformed unstructured mesh of 3784 linear quadrilateral elements, magnified 1000x (right)

Figure 2.18 provides a comparison between components of stress at the initial stage when the slope is only under gravitational forces and the moment of failure. Shear stress contours in Figure 2.18f show the development of high shear stress regions along two of the fractures in the model.

The slip along each fracture on the slope is provided in Figure 2.19a, in which it can be seen that the maximum shear displacement occurs on the fractures directly beneath the applied loading. Referring to Equation 2.14, the amount of dilation along each joint is expected to be directly proportional to the amount of slip that occurs on the interface. Figure 2.19b verifies that the maximum dilation is detected at the point of maximum slip along the critical fracture of the slope. It is also interesting to note that there is a portion along this fracture that does not undergo any dilation. This zone has a normal stress higher than the unconfined compressive strength of the material which suppresses the dilation.

(a) Horizontal stress under gravitational loading

(b) Horizontal stress prior to failure

(c) Vertical stress under gravitational loading

(d) Vertical stress prior to failure

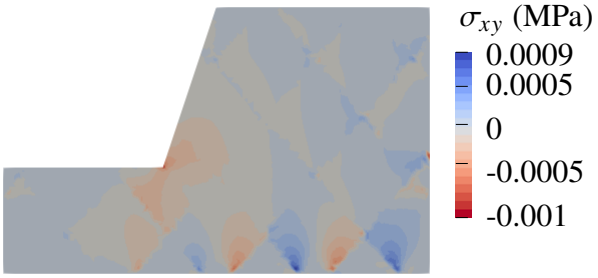

(e) Shear Stress under gravitational loading

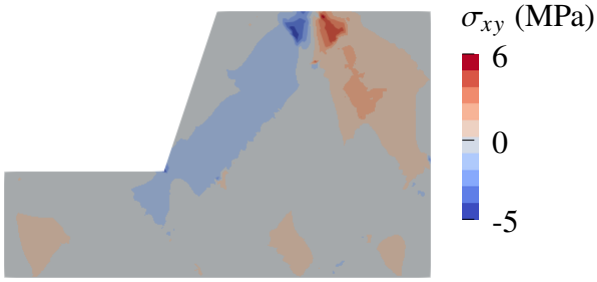

(f) Shear stress prior to failure

Figure 2.18: Stress contours under gravitational loading (a, c, e) and just before failure (b, d, f)

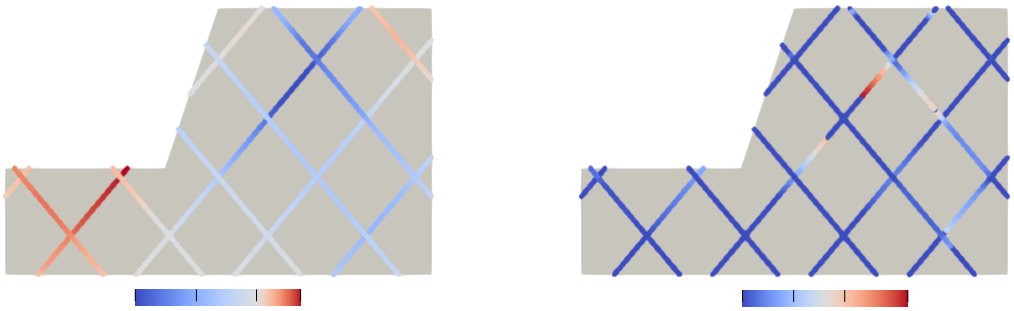

(a) Slip

(b) Shear dilation

Figure 2.19: Contours of slip (left) and dilation (right) along the fractures of the slope just before failure

Chapter 3

Numerical considerations for the simulation of proppant transport through fractures

3.1 Introduction

The purpose of this chapter is to present the numerical methodology for solving the nonlinear hyperbolic partial differential equation that describes proppant transport through a hydraulic fracture in one-dimension using the finite volume method. The model can capture the shock waves generated due to the nonlinear flux function, and the effects of spatially-varying width and pressure gradient along the fracture. It can also capture the mechanism of proppant bridging, or the impediment of proppant flow when the fracture width is too narrow. The one-dimensional model presented in this chapter is not able to capture all the relevant phenomena associated with proppant transport, such as settling, proppant bed formation, dune transport, and viscous fingering. The numerical methodology presented may be applied to a two-dimensional model to capture other mechanisms of interest.

The governing equations for the proppant particle transport are derived in Section 3.2. Possible flux functions are described in this section. In Section 3.3, the finite volume method is used to discretize the governing equations and the approximation of the finite volume fluxes is presented. This section includes the derivation of a critical time step for proppant transport, a discussion of the source of shock waves in the nonlinear problem, the approximation of the characteristic speed and flux at the cell edges, and the boundary conditions imposed on the solution. A new algorithm for constraining the proppant concentration below the saturation limit is described in this section as well. Various numerical results are then discussed in Section 3.4, including proppant transport at the inlet, at a plug, through an elliptical fracture, and a plane-strain KGD fracture. The solution

is verified by comparison with characteristic solutions. Solutions are presented using a variety of effective viscosity expressions from the literature, and the efficacy of the new constraint algorithm is studied.

3.2 Governing equations

The governing equation for proppant transport in a fracture is described in this section and placed in the context of the slurry (fluid and proppant mixture) flow. A mixture model is used which assumes that the fluid and proppant phases are fully mixed and that there is an equilibrium in mass, momentum, and energy transfer [15]. Consider a two-dimensional fracture plane with a reference coordinate system, x, running along the length of the fracture at the centerline from the wellbore to the fracture tip, as depicted in Figure 3.1. The width of the fracture, $w(x)$, is described along the fracture length and the fracture height is assumed to extend a large distance into the domain, such that plane strain conditions apply. Assuming symmetry, only half of the fracture is modeled, with the point closest to the wellbore (or inlet) located at x_0 and the tip of the fracture at x_{tip}.

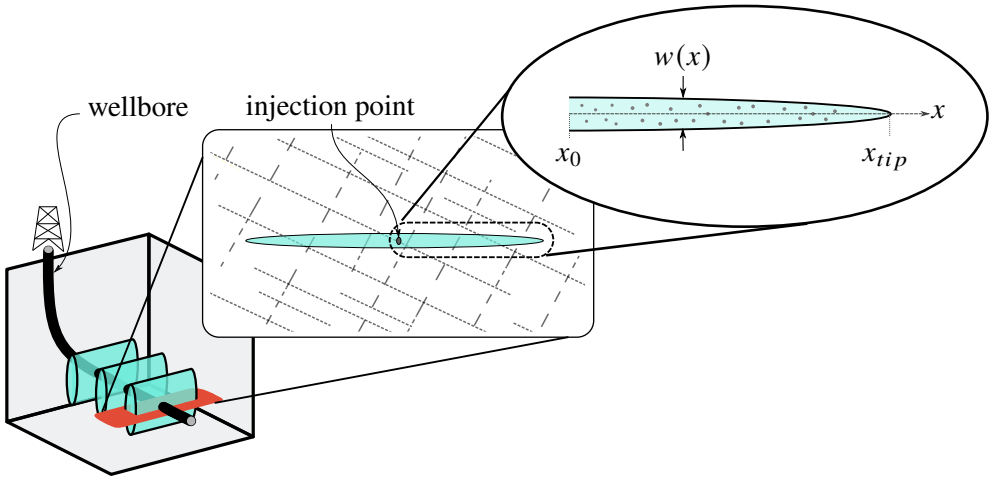

Figure 3.1: Domain of interest for a proppant transport model along a horizontal plane of a vertical fracture

3.2.1 Slurry equations

The equations for conservation of mass for the proppant and fluid phases, respectively, are given in Equations (3.1) and (3.2) below. Summing these equations leads to the conservation of mass for the slurry, given in Equation (3.3).

$$\text{proppant mass}: \quad \frac{\partial}{\partial t}\left(\phi w \rho_p\right) + \frac{\partial Q_p(\phi, w, p_{,x})}{\partial x} = \phi_{inj} Q_{inj} \delta(x - x_0) \tag{3.1}$$

$$\text{fluid mass}: \quad \frac{\partial}{\partial t}\left((1-\phi) w \rho_f\right) + \frac{\partial Q_f(\phi, w, p_{,x})}{\partial x} + Q_{sink} = (1-\phi_{inj}) Q_{inj} \delta(x - x_0) \tag{3.2}$$

$$\text{slurry mass}: \quad \frac{\partial (w\rho)}{\partial t} + \frac{\partial Q(\phi, w, p_{,x})}{\partial x} + Q_{sink} = Q_{inj} \delta(x - x_0) \tag{3.3}$$

In these equations, $\phi(x,t)$ is the average volumetric concentration of proppant particles across the fracture width at time t. The density of the proppant particles and fluid, respectively, are given by ρ_p and ρ_f, while the density of the slurry is $\rho = \phi\rho_p + (1-\phi)\rho_f$. The mass fluxes of proppant and fluid per unit fracture height are denoted by Q_p and Q_f, respectively. The total mass flux of the slurry, $Q = Q_p + Q_f$, is the sum of the proppant and fluid mass fluxes. A constitutive law defines the relationship between the flux and pressure gradient of the slurry, $\partial p/\partial x$, described in further detail below. The source term, Q_{inj}, is the mass flux of slurry per unit area of fracture injected at the wellbore, x_0. The sink term, Q_{sink}, accounts for fluid leaving the fracture in the form of leak-off into the formation.

Any two of the equations (3.1)-(3.3) can be solved to obtain the unknown variables: fluid pressure, p, and proppant concentration, ϕ. Mixture models used to simulate hydraulic fractures in the literature typically solve the proppant (3.1) and slurry (3.3) conservation equations along with the elasticity equation that describes rock deformation to obtain the fracture width. In these models, the converged solution of the rock deformation and slurry flow is obtained first and then the proppant conservation law is used to update the concentration for the next time step.

The missing equation is a constitutive law that relates the mass flux to the concentration and pressure gradient. The most commonly used assumption is that of Poiseuille flow, with a correction for the viscosity of the slurry that is dependent on the proppant concentration, $\mu(\phi)$, described in further detail in Section 3.2.3. Hammond [101] defines these constitutive laws assuming both a homogeneous slurry and a close-packed core sheet. In this work, a homogeneous slurry is assumed. Solving the conservation of momentum of the slurry mixture using lubrication theory, the slurry velocity, v, as a function of the distance along the fracture width, y, is obtained,

$$v = \frac{1}{2\mu(\phi)} \frac{\partial p}{\partial x}\left(y^2 - yw\right) \tag{3.4}$$

The velocity of the proppant component of the slurry, v_p, is defined by assuming a slip velocity between the slurry and the proppant, $v^{slip} = v_p - v$. In the literature, this slip velocity has been related to proppant settling but most models do not include the slip in the direction of the fracture length. In the context of the one-dimensional model used for this work, the proppant is assumed

to flow with the same velocity as the slurry ($v_p = v$). The mass flux of the slurry, Q, and the proppant, Q_p, are defined respectively as

$$Q = \int_0^w \rho v dy = -\rho \frac{w^3}{12\mu(\phi)} \frac{\partial p}{\partial x} \tag{3.5}$$

$$Q_p = \int_0^w \phi \rho_p v_p dy = -\phi \rho_p \frac{w^3}{12\mu(\phi)} \frac{\partial p}{\partial x} \tag{3.6}$$

Coupled hydraulic fracturing models in the literature typically hold the slurry velocity, v, constant during the proppant update, neglecting its dependence on the proppant equation as shown in Equation 3.4. Therefore, in these models, the mass flux of the slurry is linearized to $Q_p = \phi w \rho_p v$. The work in this thesis does not make this assumption, maintaining the nonlinear form of the proppant flux.

3.2.2 Proppant equation

The focus of this chapter is solely on the solution of the continuity equation of the proppant. The specific form of the equation, described in further detail in the following section, depends on the assumptions made about the effective viscosity of the slurry. The mass form of conservation equation (3.1) is rewritten in volumetric form for incompressible proppant as

$$\boxed{\frac{\partial(\phi w)}{\partial t} + \frac{\partial q}{\partial x} = \phi_{inj} q_{inj} \delta(x - x_0)} \tag{3.7}$$

in which $q = Q_p/\rho_p$ is the volumetric flux of the proppant per unit height of the fracture and q_{inj} is the volumetric injection flux per unit area of the channel. This chapter aims to discuss the solution of the nonlinear advection equation (3.7) for proppant flow in a fracture. Dividing equation (3.6) by the proppant density, the volumetric flux of the proppant is given as

$$q(\phi, \mu(\phi), w, p_{,x}) = -\phi \frac{w^3}{12\mu(\phi)} \frac{\partial p}{\partial x} \tag{3.8}$$

In this chapter, the fracture width, $w(x,t)$, and the pressure gradient, $\partial p(x,t)/\partial x$, along the fracture length are assumed to be known values taken from the solution of the rock deformation and slurry flow equations, as would occur in a sequential solution to the hydraulic fracturing model. The independent variable is the average proppant concentration, ϕ. In the context of the loosely-coupled models in the literature, this chapter is focused on the proppant update, excluding

the solution of the solid and slurry equations. Since the effective viscosity, $\mu(\phi)$, is a function of the proppant concentration, substituting the constitutive law for the flux (3.8) into (3.7) leads to a nonlinear advection equation.

3.2.3 Flux functions

Various expressions have been postulated for the effective viscosity of the slurry as a function of the proppant concentration, $\mu(\phi)$. The first viscosity expression was proposed by Einstein [102], but is applicable only for dilute suspensions. Later expressions were proposed which represent a range of slurries, from dilute to saturated suspensions. Several commonly used expressions, with both theoretical and experimental origins, are provided in Table 3.1. These expressions are written in terms of the viscosity of the carrier fluid, μ_0. Many other functions have been proposed in the literature. A comparison of expressions for effective viscosity in the context of dense suspensions is given by Stickel and Powell [103].

The fully saturated concentration, ϕ_m, is defined as the maximum packing fraction of the proppant. This is the upper limit of physically allowable proppant concentration in a fracture. Values of saturated concentration in the literature range from 0.52 for loose-packed spheres [104] to 0.74 for hexagonal close-packing of mono-disperse spherical particles [105]. In this chapter, a value of 0.64 is used, which is the value for random close-packing of mono-disperse spherical particles [105].

The proppant flux associated with several of the expressions for effective viscosity from Table 3.1 for a range of normalized proppant concentration, ϕ/ϕ_m, between 0 and 1 are shown in Figure 3.2. The curves are defined using a saturated proppant concentration of 0.64, a carrier fluid viscosity of 1 mPa·s, a fracture width of 1 mm, and a pressure gradient of -1 kPa/m. These effective viscosities share the property that as the proppant concentration approaches zero, the effective viscosity approaches the viscosity of the carrier fluid. This limit describes pure fluid flow and the proppant flux also goes to zero at this limit.

At the limit where the proppant concentration reaches the saturation point, the proppant flux should also go to zero since it is too packed to flow. From Figure 3.2 it can be seen that the expressions used by Einstein [102] and Batchelor [106] for effective viscosity do not behave in the expected manner as the proppant reaches the saturation point, because the expressions predict a flux at high concentrations which do not account for packing of the proppant. These effective viscosity relationships are thus excluded from further study here. The relationships postulated by Eskin and Miller [107], Eilers [108], and Krieger and Dougherty [109] incorporate the expected behaviors in the limit and will be further studied.

Table 3.1: Expressions of effective viscosity as a function of proppant concentration, $\mu(\phi)$

Expression		Source
$\mu(\phi) = \mu_0(1 + B\phi)$	$B = 2.5$ [1]	Einstein [102]
$\mu(\phi) = \mu_0\left(1 + B\phi + B_1\phi^2 + ...\right)$	$B_1 = 7.6$ [2]	Batchelor [106]
$\mu(\phi) = \mu_0\left(1 + B\phi + B_1\phi^2 + B_2\exp(B_3\phi)\right)$	$B_1 = 10$ $B_2 = 0.0019$ $B_3 = 20$	Eskin and Miller [107]
	$B_1 = 10.05$ $B_2 = 0.00273$ $B_3 = 16.6$	Thomas [110]
$\mu(\phi) = \mu_0\left(1 - \frac{\phi}{\phi_m}\right)^{-\beta}$	$\beta = 2.5\phi_m$ [3]	Krieger and Dougherty [109]
	$\beta = 2.5$	Nicodemo *et al.* [111]
	$\beta = 2$	Maron and Pierce [112]
	$\beta = 1.5$	Barree and Conway [113]
	$\beta = 1.82$	Krieger [114]
	$\beta = 1.89$	Scott [115]
$\mu(\phi) = \mu_0\left[1 + \left(\frac{1.25\phi}{1 - \phi/\phi_m}\right)\right]^2$		Eilers [108]

[1] Also been used with $1.5 \leq B \leq 5$ [105]
[2] Also been used with $7.35 \leq B_1 \leq 14.1$ [105]
[3] Also been used with $1 \leq \beta \leq 3$ [15]

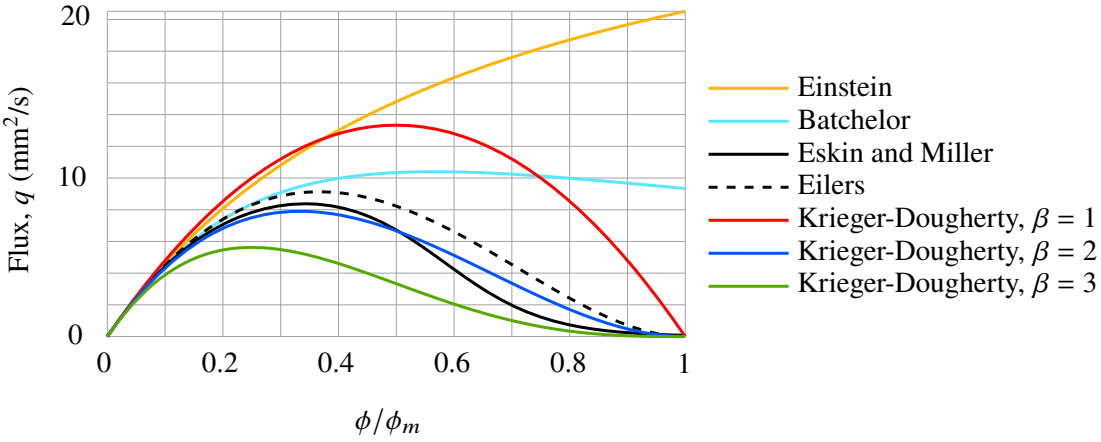

Figure 3.2: Proppant flux, q, over a range of normalized proppant concentrations, ϕ/ϕ_m. Curves are computed with a constant fracture aperture, w = 1 mm, pressure gradient, $\partial p/\partial x$ = -1 kPa/m, proppant saturation concentration, ϕ_m = 0.64, and viscosity of the carrier fluid, μ_0 = 1 mPa·s

3.2.4 Initial and boundary conditions

The conditions required to solve the proppant transport problem are described in this section. A hyperbolic problem requires initial conditions, defining the proppant concentration in the fracture at the start of the simulation by ϕ_0,

$$\phi(x, 0) = \phi_0(x) \tag{3.9}$$

At the fracture tip, proppant is prevented from exiting the fracture by applying a solid wall boundary condition which restricts proppant flow,

$$q(x_{tip}, t) = 0 \tag{3.10}$$

Based on physical limitations, the proppant concentration is constrained to non-negative values less than or equal to the saturation concentration,

$$0 \leq \phi \leq \phi_m \tag{3.11}$$

Numerical methods don't constrain the solution from exceeding the physically admissible limits, so an additional algorithm is implemented in Section 3.3.6 to explicitly constrain the problem.

Finally, proppant bridging, or arching, occurs when particles become confined between the fracture faces at very small fracture widths. The threshold fracture width at which the particles form a bridge is a function of the average proppant diameter [116]. In this work, the proppant is restricted from flowing through a fracture width smaller than 3 proppant diameters in size. This is expressed in the formulation as

$$q(x,t) = 0 \quad \text{if } w < 3 \cdot (2a) \tag{3.12}$$

in which a is the average proppant radius. Due to this constraint, the tip condition is redundant and does not come into effect under typical hydraulic fracturing conditions.

3.3 Finite volume discretization

The finite volume method used to solve the governing equation is described in detail in this section. The one-dimensional fracture is discretized into N evenly-spaced cells of length Δx, as depicted in Figure 3.3. A node is placed at the center of each cell, each associated with an unknown nodal value of proppant concentration, ϕ_i, and known values of fracture width, w_i, and fluid pressure, p_i.

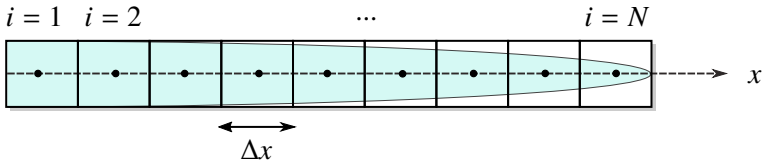

Figure 3.3: Finite Volume mesh for discretization of proppant advection

The governing equation (3.7) is integrated over a single cell associated with node i over a time step, Δt, from time t_n to t_{n+1},

$$\int_{t_n}^{t_{n+1}} \int_{x_{i-1/2}}^{x_{i+1/2}} \frac{\partial(\phi w)}{dt} dx dt + \int_{t_n}^{t_{n+1}} \int_{x_{i-1/2}}^{x_{i+1/2}} \frac{\partial q}{\partial x} dx dt = 0 \tag{3.13}$$

in which $x_{i\pm1/2}$ denote the edges of cell i. The source term due to injection is neglected in the formulation and added later as a boundary condition. In the remainder of the text, the superscript n denotes a variable evaluated at the current time t_n, and the subscript i denotes the variable evaluated at the position x_i, i.e., the proppant concentration at position x_i along the fracture and time t_n is $\phi_i^n = \phi(x_i, t_n)$. The volumetric proppant flux at location x_i and time t_n is denoted by

$q_i^n = q(\phi_i^n, \mu(\phi_i^n), w_i^n, p_{,x_i}^n)$. Using the fundamental theorem of calculus the differential terms are eliminated from the integral equation,

$$\int_{x_{i-1/2}}^{x_{i+1/2}} \left[(\phi w)^{n+1} - (\phi w)^n\right] dx + \int_{t_n}^{t_{n+1}} \left[q_{i+1/2} - q_{i-1/2}\right] dt = 0 \tag{3.14}$$

Using the midpoint numerical integration rule for the first term and adopting explicit time integration (forward Euler), the discrete equation is obtained,

$$\left[(\phi w)_i^{n+1} - (\phi w)_i^n\right] \Delta x + \left[q_{i+1/2}^n - q_{i-1/2}^n\right] \Delta t = 0 \tag{3.15}$$

Rearranging, the standard form for the explicit finite volume formulation is obtained,

$$(\phi w)_i^{n+1} = (\phi w)_i^n - \frac{\Delta t}{\Delta x}\left[q_{i+1/2}^n - q_{i-1/2}^n\right] \tag{3.16}$$

The finite volume method is conservative along the cell edges since any flux leaving or entering a cell leads to a flux entering or leaving a neighbor cell. This means the total mass in the domain is preserved and only changes due to fluxes at the boundaries. The difficulty in the finite volume method is in approximating the proppant flux terms at the cell edges, $q_{i\pm1/2}^n$.

The rest of this section describes the numerical methodology used to approximate the proppant flux at the cell edges. First, the characteristic speed of proppant is defined at the cell edges. Then, the characteristic speed is used to derive an estimate of the critical time step for proppant transport problems. The types of shock waves encountered in the solution of the nonlinear advection problem are described to define the scenarios that must be addressed in the approximation of the proppant fluxes, $q_{i\pm1/2}^n$. Finally, the high-resolution proppant flux approximation (a combination of the Godunov method and Lax-Wendroff method) at the cell edges is described.

3.3.1 Characteristic speed of proppant

The solution to the nonlinear advection equation is dependent on the characteristic speed of the proppant, which is the speed, s, at which a constant proppant concentration profile travels through the domain,

$$s = \frac{\partial q}{\partial(\phi w)} = \frac{\partial}{\partial(\phi w)}\left(-\phi \frac{w^3}{12\mu(\phi)} \frac{\partial p}{\partial x}\right) \tag{3.17}$$

The derivative that describes the proppant characteristic speed is not trivial and is instead approximated using the assumption of constant fracture aperture as $s \approx \frac{1}{w}\frac{q}{\phi}$. The proppant characteristic speed for various functions of effective viscosity is plotted over the range of normalized proppant concentrations in Figure 3.4 for a fracture width of 1 mm, a pressure gradient of -1 kPa/m, a fluid viscosity of 1 mPa·s and a maximum proppant concentration of 0.64. These curves are all characterized by being greater than zero for low proppant concentrations, signifying that proppant travels in the direction of slurry flow. The characteristic speed crosses into the negative range between $0.2\phi_m$ and $0.5\phi_m$.

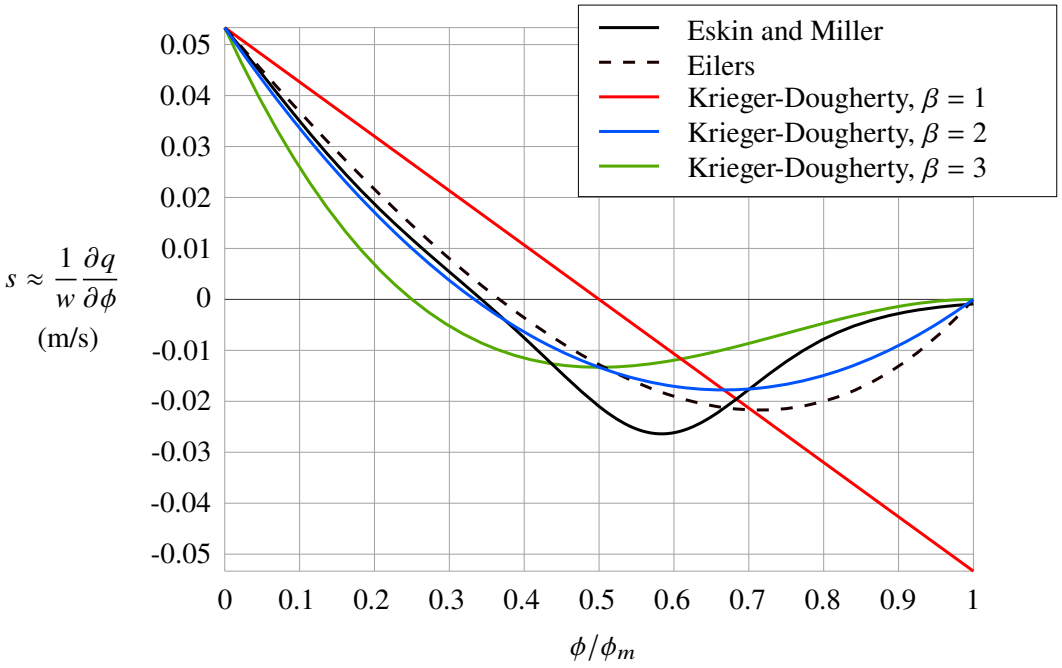

Figure 3.4: Variation in the approximate characteristic speed, s, over a range of normalized proppant concentrations, ϕ/ϕ_m. Curves are plotted for a constant fracture width, w = 1 mm, pressure gradient, $\delta p/\delta x$ = -1 kPa/m, and fluid viscosity, μ_0 = 1 mPa·s)

The proppant characteristic speed should not be confused with the direction of slurry flow. For a nonlinear advection problem, the solution remains constant along the characteristic curve, which has a slope defined by the characteristic speed. For typical fracture conditions with a negative pressure gradient inside the fracture, the proppant flux is always positive (heading towards the tip of the fracture), as shown in Figure 3.2. However, the characteristic speed is negative for higher proppant concentrations, as shown in Figure 3.4. Although the slurry is moving towards the tip of the fracture, a negative characteristic speed signifies that the net amount of proppant carried forward is limited so that the concentration builds up in the direction opposite to the flow. The curves in Figure 3.2 show that the characteristic speed of the nonlinear flux functions

naturally captures the reversal of proppant build-up direction as the concentration increases. The sudden change in direction of characteristic speed is the cause of shock waves in the solution for a nonlinear advection problem. At the saturation proppant concentration, ϕ_m, a zero characteristic speed signifies that the characteristic curve is not moving. The curve for the Krieger-Dougherty equation with $\beta = 1$ does not exhibit this behavior and is therefore not applicable for slurries at the saturation limit.

The concentration at which the characteristic speed changes sign is called the stagnation point (or sonic point) [117], and it is shown in later sections that it is important to define the stagnation point to locate the origin of a shock wave. The stagnation point, ϕ_s, for different effective viscosity functions is provided in Table 3.2.

Table 3.2: Stagnation point for various effective viscosity functions, independent of width, w, and pressure gradient, $p_{,x}$

Effective viscosity function	Stagnation point, ϕ_s
Eilers	$\dfrac{\sqrt{25\phi_m^4 + 160\phi_m^3} - 5\phi_m^2 - 8\phi_m}{10\phi_m - 8}$
Krieger-Dougherty, $\beta = 1$	$0.50\phi_m$
Krieger-Dougherty, $\beta = 2$	$0.33\phi_m$
Krieger-Dougherty, $\beta = 3$	$0.25\phi_m$

Due to the complexity of the proppant flux function, an explicit expression for the characteristic speed (3.17) is difficult to obtain, so an approximation is used. At the cell centers, the characteristic speed is approximated as

$$s_i = \frac{1}{w_i} \frac{\partial q}{\partial \phi}\bigg|_{x_i} \tag{3.18}$$

Due to the piecewise constant approximation used in the FVM, there are jumps in proppant concentration at the cell edges that create shocks in the numerical solution. The jump in propped width across a cell edge is defined as $\Delta(\phi w)_{i+1/2} = (\phi w)_{i+1} - (\phi w)_i$. Similarly, the flux wave is defined as the change in flux at the cell edge, $\Delta q_{i+1/2} = q_{i+1} - q_i$. The Rankine-Hugoniot jump condition [117] approximates the speed at which the shock on the cell-edge travels as

$$s_{R_{i\pm1/2}} = \frac{\Delta q_{i\pm1/2}}{\Delta(\phi w)_{i\pm1/2}} \tag{3.19}$$

The approximation of the proppant flux at the cell edges depends on the value of the proppant

characteristic speed at the cell edges, denoted by $s_{i\pm1/2}$. The proppant characteristic speed is approximated as the shock speed using the Rankine-Hugoniot jump condition if there is a jump in the propped width. If there is no jump in the propped width, the characteristic speed is approximated by the characteristic speed at the cell center, using an upwind method with the shock speed to determine which cell to approximate from.

$$s_{i+1/2} = \begin{cases} s_{R_{i+1/2}}, & |\Delta(\phi w)_{i+1/2}| > \epsilon_s \\ s_i, & |\Delta(\phi w)_{i+1/2}| \leq \epsilon_s \text{ and } s_{R_{i+1/2}} \geq 0 \\ s_{i+1}, & |\Delta(\phi w)_{i+1/2}| \leq \epsilon_s \text{ and } s_{R_{i+1/2}} < 0 \end{cases} \tag{3.20}$$

$$s_{i-1/2} = \begin{cases} s_{R_{i-1/2}}, & |\Delta(\phi w)_{i-1/2}| > \epsilon_s \\ s_{i-1}, & |\Delta(\phi w)_{i-1/2}| \leq \epsilon_s \text{ and } s_{R_{i-1/2}} \geq 0 \\ s_i, & |\Delta(\phi w)_{i-1/2}| \leq \epsilon_s \text{ and } s_{R_{i-1/2}} < 0 \end{cases} \tag{3.21}$$

The variable ϵ_s is a small value used to determine whether the jump in ϕw is approaching zero and taken as 10^{-8} for problems in this chapter.

3.3.2 Critical time step for proppant transport

The stable time step size for the explicit equation is limited according to the Courant-Friedrichs-Lewy (CFL) stability condition,

$$\Delta t \leq \frac{\Delta x}{s^n_{max}} \tag{3.22}$$

in which s^n_{max} is the maximum characteristic speed present throughout the domain at time t_n. An explicit expression for the characteristic speed is difficult to obtain for the nonlinear proppant flux since the term being advected is (ϕw). Hence, using the assumption that the fracture width is constant in the time step, it is approximated as

$$\begin{aligned} s^n_{max} &= \max\left(\frac{\partial q(\phi, w)}{\partial(\phi w)}\right) \\ &\approx \max\left(\frac{1}{w}\frac{\partial q(\phi, w)}{\partial \phi}\right) = \max\left(\frac{-w^2}{12\mu(\phi)}\frac{\partial p}{\partial x}\left(1 - \frac{\phi}{\mu(\phi)}\right)\right), \quad 0 \leq \phi \leq 1 \end{aligned} \tag{3.23}$$

It is interesting to note that the maximum characteristic speed of the proppant occurs at zero concentration for all the effective viscosity relationships shown in Figure 3.2. Therefore, the critical time step is the same for any selected function of effective viscosity, so long as the concentration is zero somewhere in the domain. A conservative estimate of the time step may be calculated using the proppant flux at zero concentration irrespective of the effective viscosity relationship chosen.

$$s^n_{max} \approx \max\left(\frac{-w_i^{n2}}{12\mu_0}\frac{\partial p_i^n}{\partial x}\right), \forall i \in [0, N] \tag{3.24}$$

3.3.3 Shock waves in proppant transport problems

The sources of numerical complexity of nonlinear advection problems are the shocks that appear in the solution. The solution becomes non-smooth, and the jumps in the proppant concentration propagate throughout the domain. The jumps in proppant concentration must be properly taken into account when approximating the flux at the cell edges. This section discusses the types of shock waves that arise in the propagation of proppant, and the approximation of edge fluxes is described in detail in Section 3.3.4. There are four types of shocks to account for when approximating the proppant flux at cell edges:

1. the proppant concentration jumps from cell edge to cell edge because using the finite volume method the approximate solution in each cell is taken as the average along the cell (discontinuities propagate from the cell edges, due to the discontinuous nature of the solution);

2. the proppant concentration builds up in one location and the build-up creates a shock that travels through the fracture (discontinuities due to characteristic curves merging between the cell centers creating a compression wave);

3. the proppant concentration disperses from an area of high concentration into parts of the fracture with a low concentration (discontinuities due to characteristic curves diverging between the cell centers creating a rarefaction wave); and

4. the width or pressure gradient changes along the fracture, causing the proppant concentration to change suddenly (discontinuities due to the jump in characteristic speed at cell edges).

The first type of shock that is created in the solution is a byproduct of the piecewise constant approximation of ϕ used in the finite volume method. The proppant concentration is only

approximated at the center of each cell, representing the average concentration throughout the cell. At each cell edge, there is a jump in the solution which creates a jump in the characteristic speed, or the speed at which the proppant is transported through the fracture. Considering the case where the concentrations in adjacent cells are either both above the stagnation point, ϕ_s, or both below the stagnation point, the jump in the solution for proppant concentration can lead to the creation of either left-traveling or right-traveling shock waves. The creation of these shock waves is depicted in Figure 3.5, in which the jump in proppant concentration at cell edges and the corresponding characteristic curves are shown for left- and right-traveling waves in Figures 3.5a and 3.5b, respectively. The top half of each figure depicts the portion of the fracture width filled with proppant (ϕw) for two adjacent finite volume cells, with the proppant concentration at the cell center shown in red and the cell edge represented by a dotted line. The bottom half of the figures shows the idealized characteristic curves for the proppant in each of the cells. The characteristic curve represents the curve in time and space along which the solution is constant, with the slope of the curve representing the proppant characteristic speed, s. In both scenarios shown in Figures 3.5a and 3.5b, the characteristic speed on either side of the cell edge is traveling in the same direction. The resulting shock wave has a magnitude defined by the Rankine-Hugoniot jump condition as given in Equations 3.20-3.21.

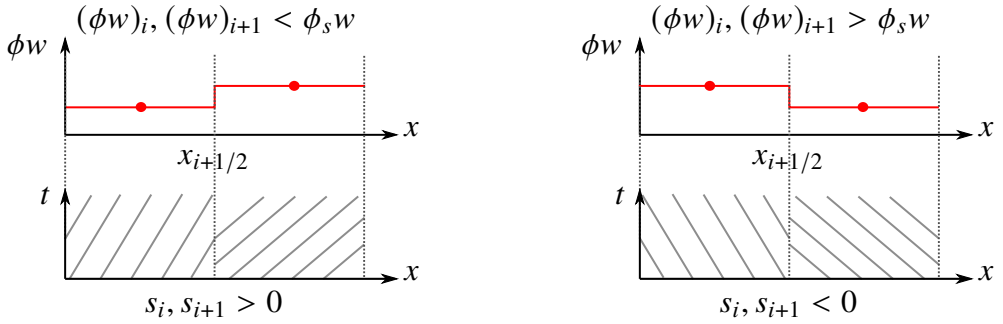

(a) Right-traveling shock wave propagating from the cell edge due to the discontinuous nature of the solution

(b) Left-traveling shock wave propagating from the cell edge due to the discontinuous nature of the solution

Figure 3.5: Visualization of characteristic curves during the formation of shock waves propagating due to discontinuity in the solution at a cell edge

The second type of shock wave occurs when the proppant in each adjacent cell is traveling towards the same edge and builds up. In hydraulic fracturing simulations, this type of shock wave occurs during the formation and growth of a plug. The accumulation of proppant concentration creates a shock wave that travels through the domain. This discontinuity stems from the merging of characteristic curves within a cell, as depicted in Figure 3.6a, creating a compression wave. The characteristic speed is positive in the left cell, and negative in the right cell, with the solution in each adjacent cell lying on either side of the stagnation point. The resulting shock wave is

naturally captured by approximating the characteristic speed using the Rankine-Hugoniot jump condition.

The third type of shock wave is generated when a build-up of proppant disperses into areas of low proppant concentration, as occurs when a proppant plug is flushed. In this scenario, the characteristic curves diverge within a cell, as depicted in Figure 3.6b. A rarefaction wave is created that spreads partially to the left and partially to the right of the cell edge. Similar to the compression wave, the solution in each adjacent cell is on either side of the stagnation point but located such that the proppant is traveling away from the cell edge instead of towards it. The solution to the conservation law in this scenario is not necessarily unique [117]. Therefore, another condition, called an admissibility condition or entropy condition, must be imposed to ensure uniqueness. In terms of proppant transport, the physical interpretation of the entropy condition is that the total proppant mass must be conserved within the domain. The magnitude of the shock wave is equivalent to the concentration at the stagnation point, given in Table 3.2. To ensure that the entropy condition is satisfied, the flux that is propagated in the rarefaction wave is equal to the flux at the stagnation point, $q_s = q(\phi_s)$. The implementation is modified for the special case of a rarefaction wave and described in further detail in Section 3.3.4.

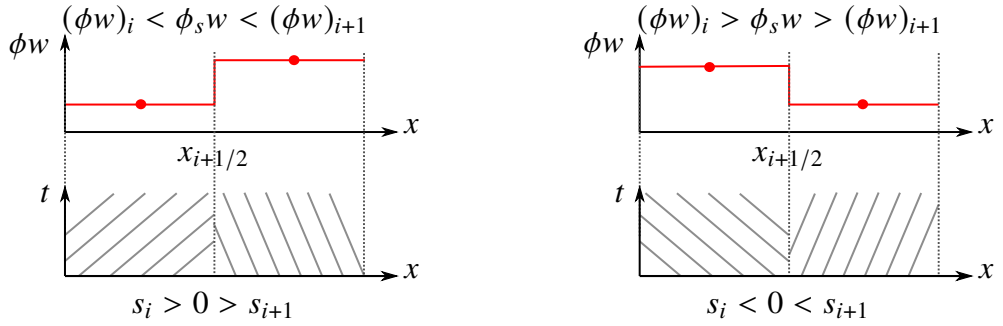

(a) Compression wave due to characteristic curves merging between the cell centers

(b) Rarefaction wave due to characteristic curves diverging between the cell centers

Figure 3.6: Visualization of characteristic curves during formation of compression and rarefaction waves

Finally, the fourth type of shock wave encountered is due to a change in fracture width or pressure gradient of the slurry along the fracture, as occurs due to hydraulic fracture propagation. Similar to the proppant concentration, both the fracture width and pressure gradient are specified at cell centers and are discontinuous at the cell edges, causing a jump in the characteristic speed at the cell edge. The jump in characteristic speed related to this spatially-varying flux function results in a stationary shock wave–an abrupt change in the solution that does not travel through the domain. The magnitude of the jump in solution is difficult to approximate, but since the flux must be conserved at the cell edge, writing the approximation in terms of the change in flux allows for the

stationary shock wave to be accounted for. The implementation presented by Bale *et al.* [118] is used and described in further detail in Section 3.3.4.

3.3.4 Approximation of proppant fluxes

The difficulty in the finite volume method is in approximating the flux terms at the cell edges, $q^n_{i\pm1/2}$. The flux is dependent on terms that are known only at the cell centers. The method selected for the approximation must take into account that the flux function is nonlinear and spatially varying, which introduces discontinuities in the solution that travel as shock waves through the domain. In this section, a high-resolution method is described which accounts for the shock waves described in the previous section. On their own, the Godunov method and the Lax-Wendroff method add numerical inaccuracies to the solution [117]. The Godunov method adds numerical diffusion (over-smoothing) and the Lax-Wendroff method adds numerical dispersion (lag). The best features of the two methods are maintained by using a high-resolution method that combines them using Total Variation Diminishing (TVD) slope limiters. These methods are described in detail in the following sub-sections. Using an explicit formulation, all values are computed at the current time, t_n. For simplicity, all superscripts n are excluded in this section, but it is implied that all values are calculated at the current time step.

Godunov method

The Godunov method approximates the flux at the cell edges, $q_{i\pm1/2}$, by solving the Riemann problem at each of these edges using the characteristics. This method provides a first-order approximation which naturally accounts for discontinuities propagating left and right, and characteristics merging between the cell centers (shock waves of type 1 and 2 mentioned in the previous section). In the case of a linear flux function, $q = c\phi$ with constant-valued c, the Godunov method is identical to the first-order upwinding method.

A rarefaction wave in which proppant spreads between the cell centers as depicted in Figure 3.6b is not captured naturally using the Godunov method. The Godunov method may lead to an incorrect solution that does not satisfy the entropy condition [117], described in Section 3.3.3. The entropy condition is a constraint imposed on the conservation law to ensure that the total proppant mass is conserved within the domain. To ensure that the entropy condition is satisfied, the flux that is propagated in the rarefaction wave is equal to the flux at the stagnation point, $q_s = q(\phi_s)$. The stagnation points are given in Table 3.2 for various expressions of viscosity. To correctly capture the rarefaction wave, the Godunov method with an entropy fix approximates the flux at the cell edges as,

$$q^G_{i+1/2} = \begin{cases} q_s, & s_{i+1} > 0 \text{ and } s_i < 0 \\ q_i, & s_{i+1/2} \geq 0 \\ q_{i+1}, & s_{i+1/2} < 0 \end{cases} \tag{3.25}$$

$$q^G_{i-1/2} = \begin{cases} q_s, & s_i > 0 \text{ and } s_{i-1} < 0 \\ q_{i-1}, & s_{i-1/2} \geq 0 \\ q_i, & s_{i-1/2} < 0 \end{cases} \tag{3.26}$$

The formulation is based on the flux at cell centers, q_i, for $i = 1, 2, ..., N$. If there is no rarefaction wave, the selection of the flux is based on the direction of the characteristic speed at the cell edges, $s_{i\pm1/2}$, computed by Equations 3.20 and 3.21.

The rarefaction wave is characterized by a proppant concentration on either side of the stagnation point. The flux functions of interest in proppant transport have two stagnation points, as shown in Figure 3.4. One occurs for a normalized proppant concentration, ϕ/ϕ_m, between 0.2 and 0.5 depending on the expression of effective viscosity used, and the other occurs for a normalized proppant concentration $\phi/\phi_m = 1$. The range of physically admissible normalized proppant concentrations is between 0 and 1, so the stagnation point at a normalized proppant concentration of 1 is typically not encountered in simulations. However, this formulation can capture both stagnation points.

Lax-Wendroff method

The first-order Godunov method adds numerical diffusion to the solution, particularly near shock waves where the gradient of the concentration profile is steep. For this reason, a high-resolution method is required to avoid over-smoothing of the solution and maintain a sharp proppant front. The Lax-Wendroff method provides a second-order approximation and contains anti-diffusive terms in the formulation which cancel out the numerical diffusion created in the Godunov method [117].

The Lax-Wendroff method is typically written in terms of the jump in the propped aperture at the cell edge, $\Delta(\phi w)$. For spatially-varying flux functions, the jumps in proppant concentration also arise because the fracture width and pressure gradient are discontinuous at cell edges. The jump in concentration at the cell edge is therefore not a straightforward calculation based on the values at the neighboring nodes. Using the fact that flux is conserved at the cell edge, Bale *et al.* [118] wrote the Lax-Wendroff approximation in terms of the change in flux, Δq, which is equipped to handle spatially-varying fluxes and does not require an explicit calculation of the

change in concentration, $\Delta\phi$, at the cell edge. The flux approximations at the cell edges using the Lax-Wendroff method based on flux waves are

$$q_{i+1/2} = \Delta q_{i+1/2} H(-s_{i+1/2}) + \underbrace{\frac{1}{2}\text{sign}(s_{i+1/2})\left(1 - \frac{\Delta t}{\Delta x}|s_{i+1/2}|\right)\Delta q_{i+1/2}}_{q^{LW}_{i+1/2}} \tag{3.27}$$

$$q_{i-1/2} = -\Delta q_{i-1/2} H(s_{i-1/2}) + \underbrace{\frac{1}{2}\text{sign}(s_{i-1/2})\left(1 - \frac{\Delta t}{\Delta x}|s_{i-1/2}|\right)\Delta q_{i-1/2}}_{q^{LW}_{i-1/2}} \tag{3.28}$$

in which the flux wave is defined as the change in flux at the cell edge, $\Delta q_{i+1/2} = q_{i+1} - q_i$, and $H()$ is the Heaviside step function. The first term in the approximation is equivalent to the Godunov method without the entropy fix, and the second term can be seen as a correction term for the diffusion in the Godunov method. The correction term, $q^{LW}_{i\pm1/2}$, is used in the following section to define a high-resolution method.

High resolution method

The Lax-Wendroff method eliminates the numerical diffusion seen in the Godunov method but adds some lag (numerical dispersion) to the solution. To take advantage of the properties of the Godunov method when the solution is smooth, and the Lax-Wendroff method when there is a sharp gradient in the solution, a flux limiter method is used. The flux approximation at the cell edges is given by

$$\begin{aligned} q_{i+1/2} &= q^{G}_{i+1/2} + \varphi(r_{i+1/2}) q^{LW}_{i+1/2} \\ q_{i-1/2} &= q^{G}_{i-1/2} + \varphi(r_{i-1/2}) q^{LW}_{i-1/2} \end{aligned} \tag{3.29}$$

in which the superscripts G and LW refer to the Godunov approximation (3.25-3.26) and the correction term in the Lax-Wendroff approximation (3.27-3.28), respectively.

The function $\varphi(r)$ is called the limiter function, which is responsible for applying the second-order corrections when there is a sharp gradient in the solution. The limiter function varies between 0 for a smooth concentration profile and 1 for a sharp jump in concentration, effectively working to add more of the Lax-Wendroff correction near discontinuities. Various limiter functions have been developed, with the key feature being that they are Total Variation Diminishing (TVD). The

total variation of the solution is the sum of the jump in concentration at all cell edges throughout the domain. Oscillations introduced by the numerical method would increase the total variation of the solution over time. TVD limiter functions are chosen to avoid adding oscillations by requiring that the method not increase the total variation of the solution. A review of possible limiters can be found in LeVeque [117]. This work uses the monotized central-difference (MC) limiter, defined as

$$\varphi(r) = \max(0, \min((1+r)/2, 2, 2r)) \tag{3.30}$$

No significant difference is observed in the numerical results presented in Section 3.4 when compared with simulations using the Min-Mod, Superbee, and Van Leer limiters. The variable r in the limiter function is the slope ratio, which relates the upwind concentration gradient to the gradient at the cell edge, is defined at the cell edges as

$$r_{i+1/2} = \begin{cases} \dfrac{(\phi w)_i - (\phi w)_{i-1}}{(\phi w)_{i+1} - (\phi w)_i}, & s_{i+1/2} \geq 0 \\ \dfrac{(\phi w)_{i+2} - (\phi w)_{i+1}}{(\phi w)_{i+1} - (\phi w)_i}, & s_{i+1/2} < 0 \end{cases} \tag{3.31}$$

$$r_{i-1/2} = \begin{cases} \dfrac{(\phi w)_{i-1} - (\phi w)_{i-2}}{(\phi w)_i - (\phi w)_{i-1}}, & s_{i-1/2} \geq 0 \\ \dfrac{(\phi w)_{i+1} - (\phi w)_i}{(\phi w)_i - (\phi w)_{i-1}}, & s_{i-1/2} < 0 \end{cases} \tag{3.32}$$

To define the upwind direction, the characteristic speed at the cell edge is approximated as described in Section 3.3.1. The sign of the approximated characteristic speed is used to determine the upwind direction for calculation of the slope ratio.

3.3.5 Boundary conditions

Flux boundary conditions are applied on both sides of the domain. At the wellbore (left edge of the domain) is an inflow boundary, which is implemented by prescribing the injection flux on the left edge of the first cell,

$$q_{1/2} = \phi_{inj} q_{inj} \tag{3.33}$$

At the fracture tip (right edge of the domain) is a solid wall boundary, which is prescribed by setting the flux on the right edge of the last cell to zero,

$$q_{N+1/2} = 0 \tag{3.34}$$

3.3.6 Proppant concentration constraints

Since the approximation of fluxes is not perfect, it is possible to obtain non-physical concentration values, outside the range $\phi \in [0, \phi_m]$. To avoid this, the predictor-corrector algorithm described below is implemented to prevent proppant from flowing into cells that have already reached the maximum concentration, ϕ_m, and to prevent proppant from leaving cells that are at the minimum proppant concentration, $\phi = 0$. The predictor step uses the flux approximation described in the previous sub-sections to solve for the proppant concentration at the next time step. Then, the set of cells that have a concentration outside the allowable range are identified and the fluxes going in/out of those cells are adjusted so that the final concentration is exactly the limit value. Finally, the concentration at the next time step is calculated using the adjusted fluxes. The algorithm is outlined below. In the simulations shown in this chapter, the aperture at the next time step is assumed to equal the aperture at the previous time step, $w_i^{n+1} = w_i^n$.

1. *Predictor step*: solve for concentration at the next time step ($\phi_{i,p}^{n+1}$) using the approximated fluxes ($q_{i+1/2}^n$ and $q_{i-1/2}^n$),

$$\phi_{i,p}^{n+1} = \phi_i^n \frac{w_i^n}{w_i^{n+1}} - \frac{\Delta t}{w_i^{n+1}\Delta x}\left(q_{i+1/2}^n - q_{i-1/2}^n\right) \tag{3.35}$$

   (a) Identify the set of cells with concentrations that are not within the allowable range. The sets of cells which have a proppant concentration above the maximum ($\phi = \phi_m$) and below the minimum ($\phi = 0$) are denoted by S^+ and S^-, respectively).

   (b) Correct the fluxes according to the current inflow/outflow:
   For cells in set S^+, the correction flux is defined as

$$q_{correct}^+ = w_i^{n+1}\frac{\Delta x}{\Delta t}\left(\phi_i^n \frac{w_i^n}{w_i^{n+1}} - \phi_m\right) \tag{3.36}$$

   The corrected cell edge flux approximations, $q_{i\pm1/2}^c$, are defined depending on the predictor flux approximation, as defined in Figure 3.7.

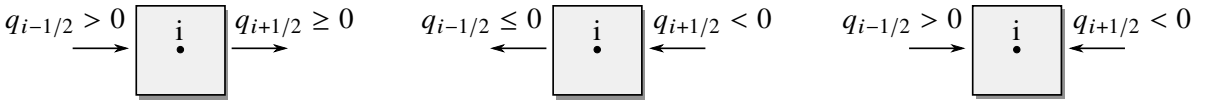

Figure 3.7: Corrected cell edge fluxes for cells in set S^+

For cells in set S^-, the correction flux is defined as

$$q^-_{correct} = \phi^n_i w^n_i \frac{\Delta x}{\Delta t} \tag{3.37}$$

The corrected cell edge flux approximations, $q^c_{i\pm1/2}$, are defined depending on the predictor flux approximation, as defined in Figure 3.8.

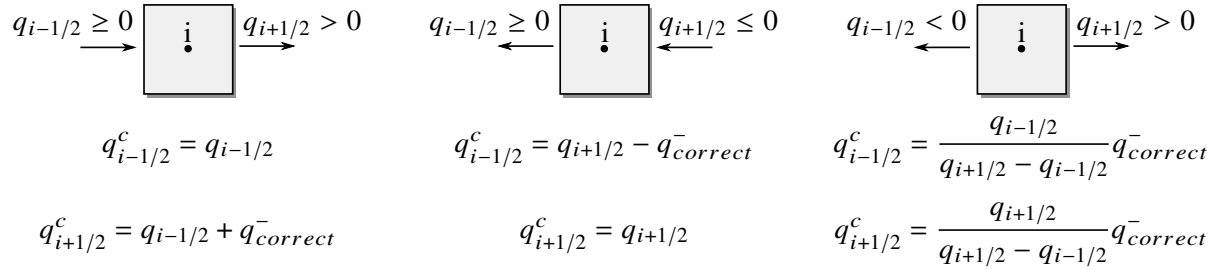

Figure 3.8: Corrected cell edge fluxes for cells in set S^-

(c) Update the fluxes for the neighboring cells accordingly to maintain conservation property.

2. *Corrector step*: solve for concentration using the corrected fluxes

$$\phi^{n+1}_i = \phi^n_i \frac{w^n_i}{w^{n+1}_i} - \frac{\Delta t}{w^{n+1}_i \Delta x} \left(q^c_{i+1/2} - q^c_{i-1/2} \right) \tag{3.38}$$

3. Set the approximation to the corrected fluxes, $q^n_{i+1/2} = q^c_{i+1/2}$, and repeat if any concentrations are still outside the acceptable range (in simulations it was found that repetitions are rarely required).

3.4 Numerical results

In this section, the implementation of the numerical methodology is verified for the case of a rarefaction wave and a compression wave. Proppant transport through an elliptical fracture is studied, and the limit injection rate is found for which a proppant plug occurs at the inlet. Finally, proppant flow through a plane-strain KGD fracture is investigated in which proppant bridging is observed, and the use of a concentration constraint is investigated. All results are compared using various expressions for effective viscosity to understand how the solution varies with the selection of expression. Parameters that are constant for all simulations in this section are specified in Table 3.3.

Table 3.3: Material properties for simulations of proppant transport through planar fractures

Parameter	Variable	Value	Unit
Maximum proppant concentration	ϕ_m	0.64	
Carrier fluid viscosity	μ_0	1.2	mPa·s
Average proppant radius	a	0.3	mm

3.4.1 Injection and growth of propped fractures

The first problem considered is proppant advection in a 100 m channel of constant width (2 mm) and constant pressure gradient (-0.5 kPa/m) that is initially packed with proppant on the left half ($x < 0$) with a concentration of $0.9\phi_m$. The initial conditions prescribed, shown in Figure 3.9a, occur in hydraulic fractures at the fracture inlet where the injected proppant builds up quickly. The proppant must spread to the surrounding fracture which does not yet contain any proppant. This concentration profile also arises in the case of a propped fracture with a saturated concentration at the tip. As such a fracture grows in length, the proppant flows into the new fracture segment that is initially void of proppant.

Solution of the nonlinear advection equation with the initial proppant concentration described results in a rarefaction wave spreading from the jump in concentration–the characteristic speed is negative to the left of the proppant front and positive to the right of the proppant front. Therefore, the concentration diminishes for $x < 0$ and increases for $x > 0$. Although a constant channel width and pressure gradient is not representative of conditions in a hydraulic fracture, the problem is used for verification of the numerical method and ensures that the rarefaction wave can be adequately captured by the entropy fix described in Section 3.3.4. This problem resembles the so-called green-light problem in traffic flow simulations, which models the advection of vehicles when a traffic light turns green [117]. The Krieger-Dougherty equation for effective viscosity of

the fluid with $\beta = 1$ has the same form as the linear traffic flow equation and produces the same shape of the rarefaction curve.

The channel is discretized with 500 cells. Outflow boundary conditions are applied on both ends of the channel, allowing the proppant to leave the domain at these boundaries. There is no injection of proppant into the domain, simply advection of the initial proppant concentration for 500 seconds. The problem is solved using various forms of the flux function, and the resulting concentration profiles throughout the simulation time are shown in Figure 3.9. In all cases, proppant concentration is reduced to the left of the initial discontinuity ($x < 0$), and increased to the right ($x > 0$). The shape of the rarefaction wave over time is dependent on the characteristic speed of the flux function. The proppant characteristic speed corresponding to the initial proppant concentration profile is shown for each viscosity expression in Figure 3.10. The curve of the characteristic speed matches the curve of the corresponding rarefaction wave in Figure 3.9. The concentration at which the proppant front smooths out is the stagnation point, provided in Table 3.2. For the nonlinear characteristic speed curves that are double-valued, the equal-area rule determines the location of the shock front theoretically [117]. The theoretical curves match the resultant concentration profiles after rarefaction, verifying the shape of the solution. For the same initial proppant concentration, the use of the Krieger-Dougherty equation with $\beta = 1$ leads to the most proppant spreading, while $\beta = 3$ leads to the least spreading of the proppant. The other viscosity functions lead to concentration profiles that lie between these two limits.

3.4.2 Plug formation and growth

The next problem considered is proppant advection in a 50 m channel of constant width (2 mm) and constant pressure gradient (-0.5 kPa/m) that is initially packed with proppant on the right half ($x > 0$) with a concentration of $0.9\phi_m$. The left half of the channel ($x < 0$) has a concentration of $0.3\phi_m$. The initial concentration profile prescribed in this problem (seen in Figure 3.11a) leads to a compression wave that moves towards the left of the channel, representing proppant build-up at a plug. This concentration profile may arise for a plug forming at the fracture tip, or proppant bridging along the length of the channel where the fracture width is not large enough for the proppant to flow through. This problem is used for verification of the numerical method, ensuring that the compression wave can be adequately captured using the flux approximation described in Section 3.2.3 and that concentration limits are not exceeded. This problem resembles the so-called red-light problem in traffic flow simulations, which models the advection of vehicles when a traffic light turns red [117].

The channel is discretized using 500 cells and the advection of the initial concentration profile lasts 500 seconds. The proppant concentration throughout the simulation time is shown for various expressions of effective viscosity in Figure 3.11. In all the cases shown, the proppant concentration builds up to the left of the discontinuity ($x < 0$). The shape of the compression

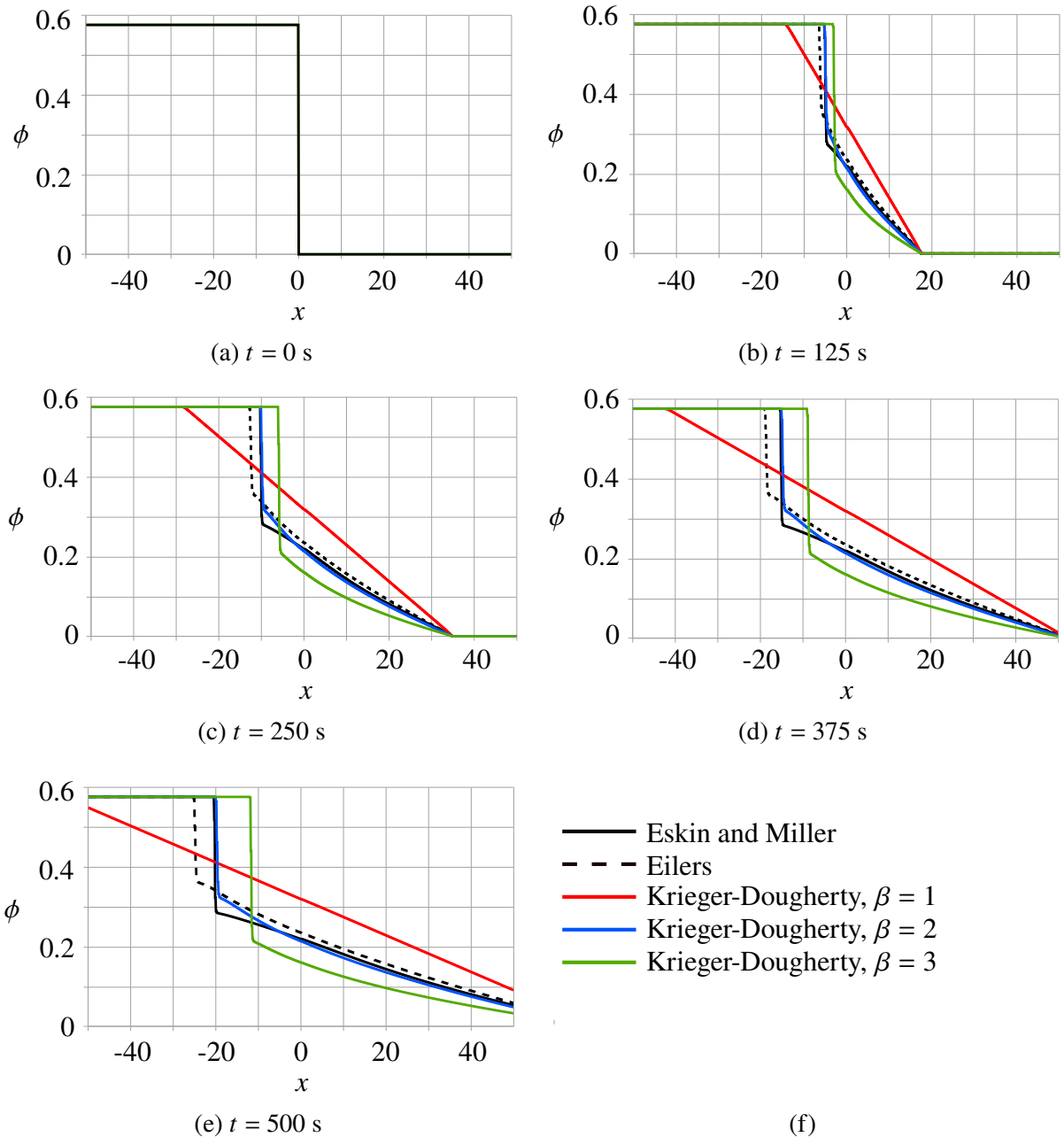

Figure 3.9: Proppant concentration spreading at the fracture inlet over time

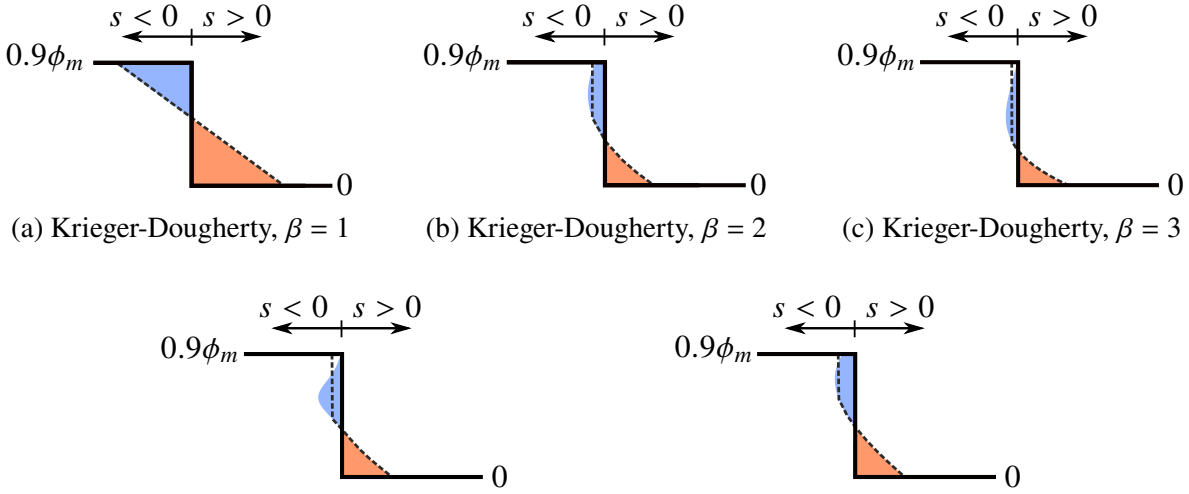

(a) Krieger-Dougherty, $\beta = 1$ (b) Krieger-Dougherty, $\beta = 2$ (c) Krieger-Dougherty, $\beta = 3$

(d) Eskin and Miller (e) Eilers

Figure 3.10: Theoretical characteristic speed patterns for rarefaction waves

wave is also dependent on the characteristic speed, depicted for the initial concentration profile in Figure 3.12. The resulting concentration profiles match the theoretical curves obtained from the characteristic speed patterns, after applying the equal-area rule for multi-valued solutions [117]. Similar to the first test case in Section 3.4.1, the use of the Krieger-Dougherty equation with $\beta = 1$ leads to the fastest-moving shock wave and $\beta = 3$ is the slowest-moving shock wave.

3.4.3 Inject into an elliptical fracture with constant pressure gradient

The proppant flux is a function of the proppant concentration, fracture width, and fluid pressure gradient. The verification cases performed in the previous sections had a constant fracture width and pressure gradient, with nonlinearity coming only from the proppant concentration. The next problem studies proppant advection through a 100 m long elliptical channel with a maximum fracture width of 3 mm. A constant pressure gradient of -0.5 kPa/m is maintained throughout the fracture length. Although a constant pressure gradient is not representative of conditions in a hydraulic fracture, this condition is useful for studying the shocks in the solution that originate due to nonlinearity in the fracture width.

The channel is discretized using 500 cells. The proppant width is calculated at the center of each finite volume cell and adds another spatially-varying term in the flux function. A solid wall boundary condition (3.34) is applied to the fracture tip on the right-hand side of the domain.

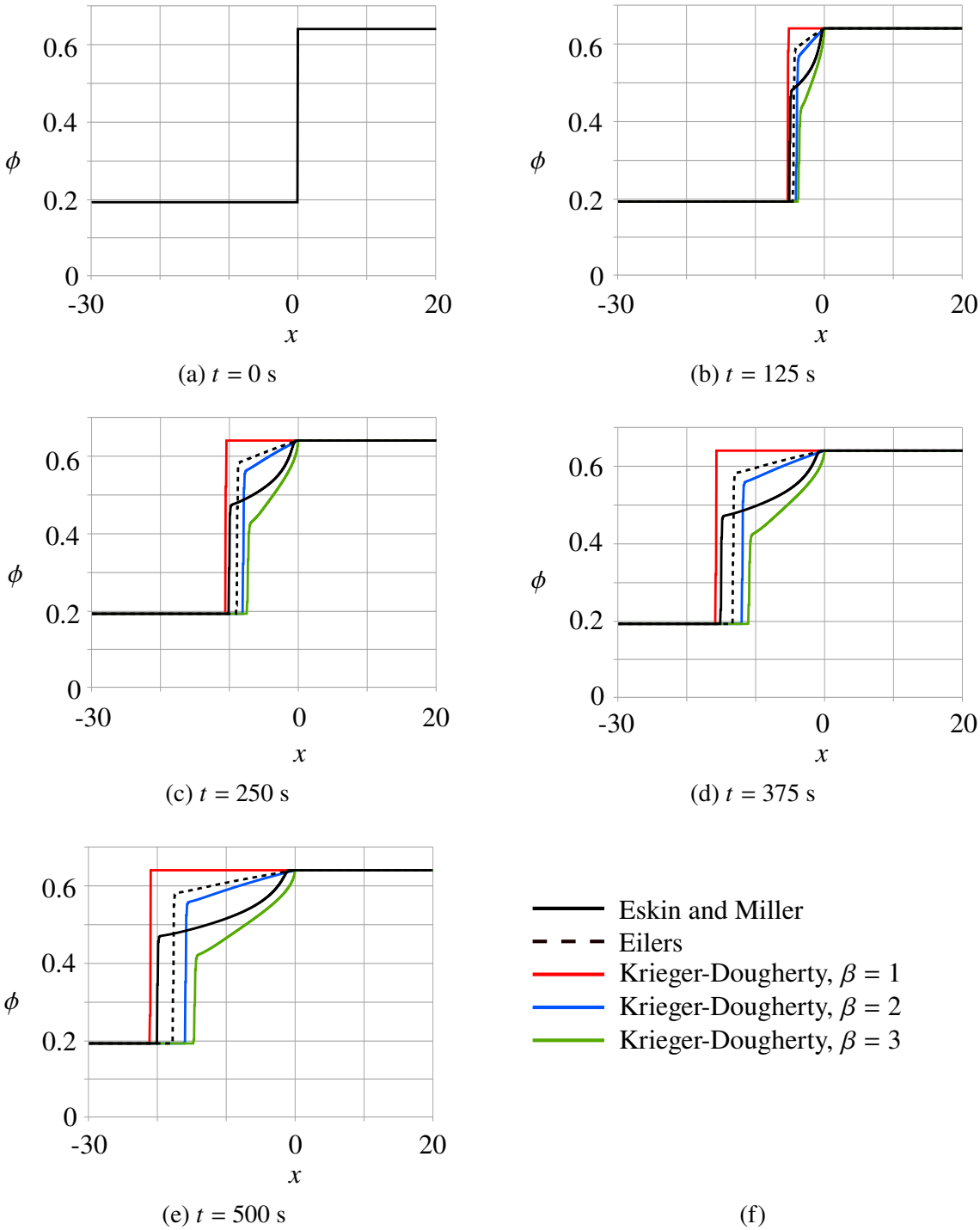

Figure 3.11: Proppant concentration backing up at a plug over time

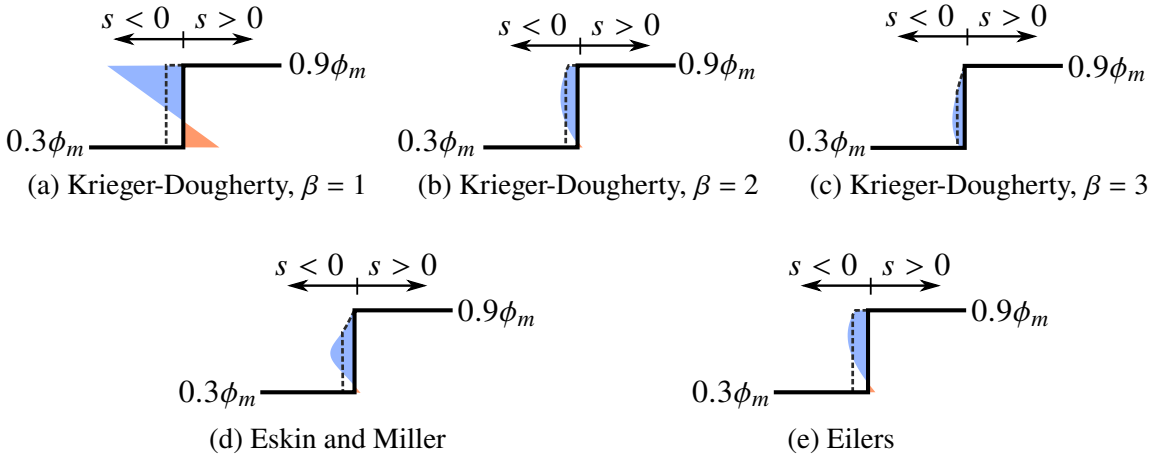

(a) Krieger-Dougherty, $\beta = 1$ (b) Krieger-Dougherty, $\beta = 2$ (c) Krieger-Dougherty, $\beta = 3$

(d) Eskin and Miller (e) Eilers

Figure 3.12: Theoretical characteristic speed patterns for compression waves

Proppant is injected at a constant volumetric concentration of 0.1 for 800 seconds, with an inlet flux given in Table 3.4 for each viscosity expression studied.

Table 3.4: Injection rate used to maintain injection concentration of $\phi_{inj} = 0.1$ for various expressions of effective viscosity

Viscosity Expression	$\phi_{inj}(t)q_{inj}(t) = 0.1\frac{-w^3}{12\mu(0.1)}\frac{\partial p}{\partial x}$
Eskin and Miller	68.730 mm^2/s
Eilers	71.117 mm^2/s
Krieger-Dougherty, $\beta = 1$	79.101 mm^2/s
Krieger-Dougherty, $\beta = 2$	66.742 mm^2/s
Krieger-Dougherty, $\beta = 3$	56.313 mm^2/s

A blocking function is included in the flux formula, which prevents proppant from flowing into a cell with a fracture width less than 3 proppant diameters in size, as defined in Equation 3.12. Figure 3.13 shows the proppant concentration profiles for various times using five different expressions for effective viscosity. The injected proppant travels towards the tip of the fracture as a rarefaction wave, with the narrowing fracture width creating a small build-up of proppant ahead of the concentration jump (see Figure 3.13b). Once the proppant front reaches 80 m, the small fracture width causes bridging and prevents proppant from flowing to the tip, as seen in Figure 3.13c. The proppant builds up to the saturation concentration and another shock wave emerges forcing the proppant to build up towards the inlet. In Figure 3.13d two shock fronts are visible–one moving towards the right from the initial injection spreading and one moving towards the left as the proppant plug grows from the screen-out point. Dontsov and Peirce [73]

propose a modified blocking function that provides a smoother transition for the on/off status of the function. No difference was found in the solution when tested with the modified version, which shows that the modification by Dontsov and Peirce [73] approximates the condition very well. The approximation using the Krieger-Dougherty equation with $\beta = 1$ creates the fastest proppant transport towards the tip and subsequent build-up, while the slowest advection occurs using $\beta = 3$.

3.4.4 Injection into KGD fracture

Proppant advection through a hydraulic fracture is simulated by discretizing the fracture into 500 finite volume cells. The approximate solution for a finite, plane-strain fracture (KGD) derived by Dontsov [119] was used to obtain the fracture width and pressure along the fracture length after injecting pad fluid for 30 min at a rate of 0.01 m^3/s into a 10 m high fracture. The solution is obtained for a rock mass with Young's modulus of 40 GPa, Poisson's ratio of 0.25, fracture toughness of 1 $MPa\sqrt{m}$, and Carter leak-off coefficient of 0.001 $m/\sqrt{min}$. The fracture propagates to 213.1 meters in 30 min, with a width and pressure gradient profile as shown in Figure 3.14. The pressure gradient is calculated using a forward difference from the pressure profile. Due to the blocking function, the proppant is prevented from flowing through portions of the fracture with an aperture narrower than 3 proppant diameters. Therefore the proppant does not reach the fracture tip. The pressure gradient throughout the majority of the fracture length is approximately -500 Pa/m, with a much higher pressure gradient at the inlet of -25,000 Pa/m, and the fracture tip. An accurate pressure profile for a hydraulic fracture can only be obtained through a fully coupled model since the proppant concentration will change the effective viscosity of the fluid and increase the fluid pressure. This problem is used to demonstrate the types of shocks that occur in the proppant transport solution due to the large changes in pressure gradient at the fracture inlet.

Maintaining a constant width and pressure profile, proppant slurry is injected into the fracture for 30 min at a rate of 40 mm^2/s. The concentration profiles for various times throughout the injection are shown in Figure 3.15 for several effective viscosity expressions. The advection is affected by both the nonlinear fracture width and the nonlinear pressure gradient along the length of the fracture. The steep change in pressure gradient at the inlet causes the proppant to build-up around 50 m into the fracture as it spreads towards the fracture tip. Proppant bridging occurs approximately 150 m into the fracture at which point the concentration reaches the saturation point and builds up towards the inlet. The Krieger-Dougherty viscosity function with $\beta = 1$ results in the fastest proppant transport towards the fracture tip and also the fastest build-up at the tip. In contrast, the function with $\beta = 3$ produces the most build-up of proppant near the inlet and slowest build-up at the plug. These two viscosity functions represent the limits for all problems studied in this chapter.

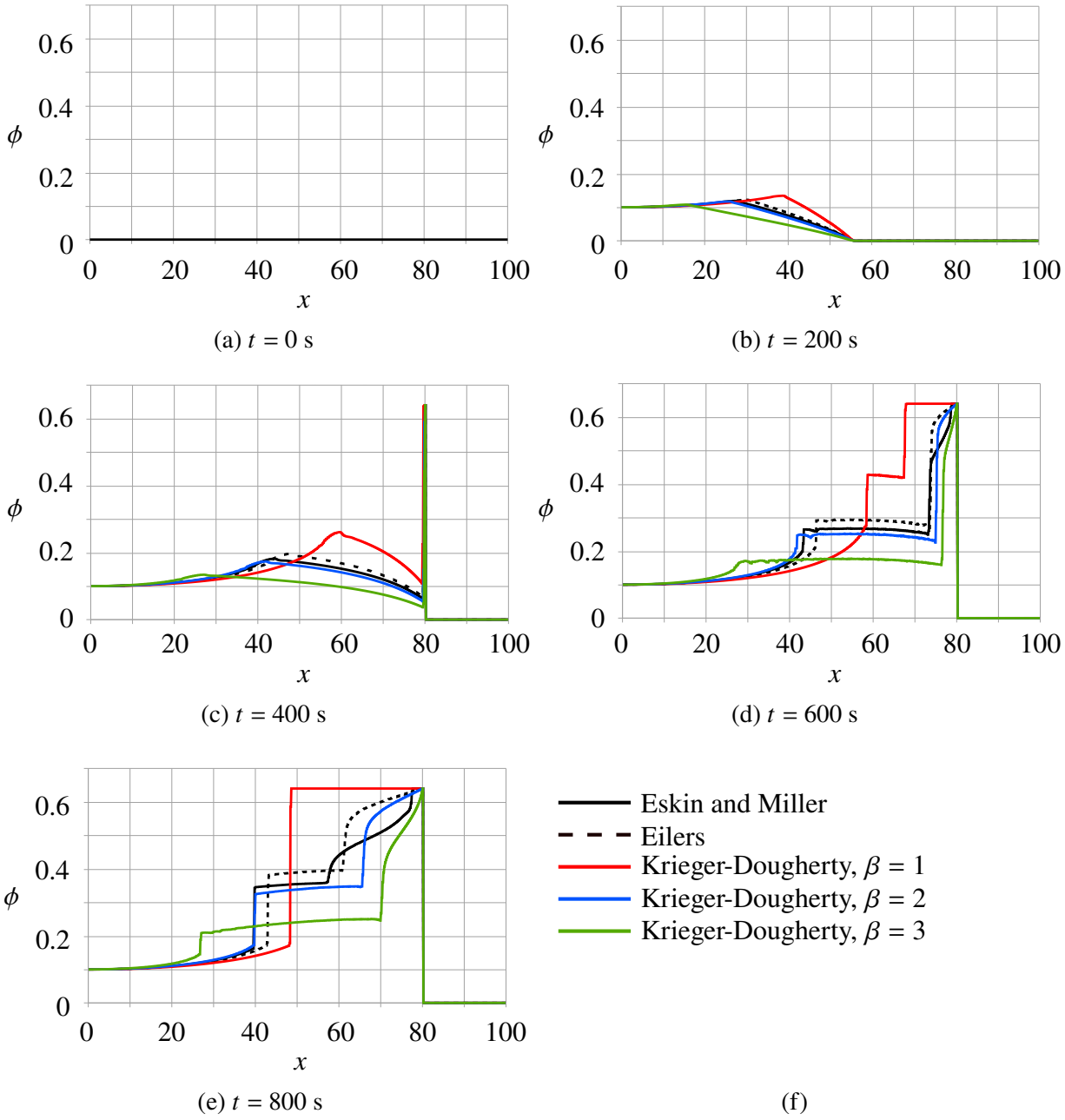

(a) $t = 0$ s

(b) $t = 200$ s

(c) $t = 400$ s

(d) $t = 600$ s

(e) $t = 800$ s

(f)

Figure 3.13: Proppant injection into an elliptical fracture with constant pressure gradient over time

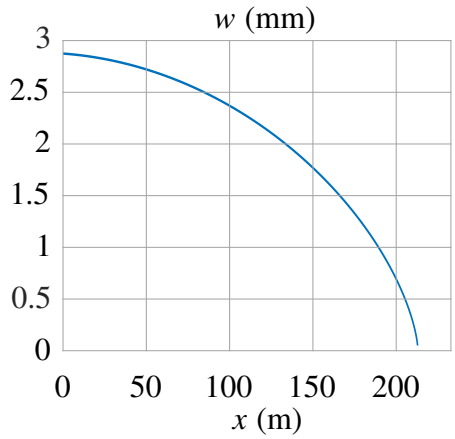

(a) Width profile for KGD fracture [119]

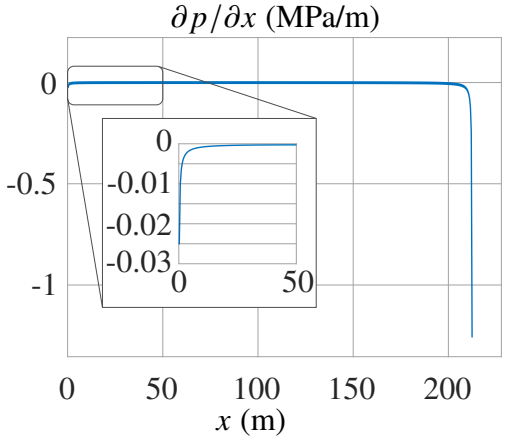

(b) Pressure gradient profile for KGD fracture [119]

Figure 3.14: Width and pressure along the length of a KGD fracture. Solutions are obtained for a rock mass with Young's modulus of 40 GPa, Poisson's ratio of 0.25, fracture toughness of 1 MPa$\sqrt{\text{m}}$, and Carter leak-off coefficient of 0.001 m/$\sqrt{\text{min}}$

Implementation of the concentration constraint described in Section 3.3.6 makes the solution stable and remain within the physical bounds. It is most common to see the concentration exceed the maximum either near the boundary or at a tip-screen out location. In unrefined meshes, oscillations due to a poor approximation may cause the concentration to exceed the maximum as well. In these situations, the concentration constraint prevents the problem from becoming unbounded. The concentration profiles obtained without imposing the constraint are shown in Figure 3.16 (dashed lines). In some cases, the solution oscillates above the limit, as in Figure 3.16a. In other cases, the solution becomes unbounded and the last cell increases in concentration without allowing a build-up of proppant in neighboring cells, such as in Figures 3.16b and 3.16e. These non-physical concentrations are avoided by imposing concentration constraints.

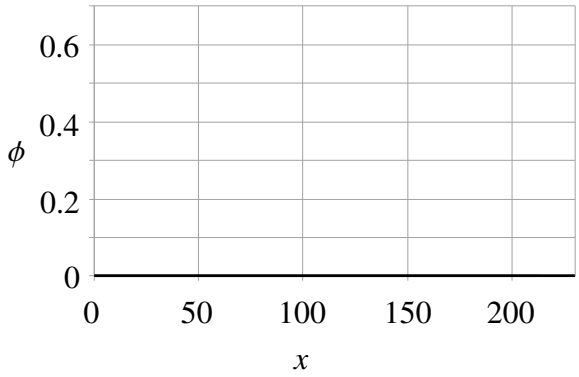

(a) $t = 0$ s

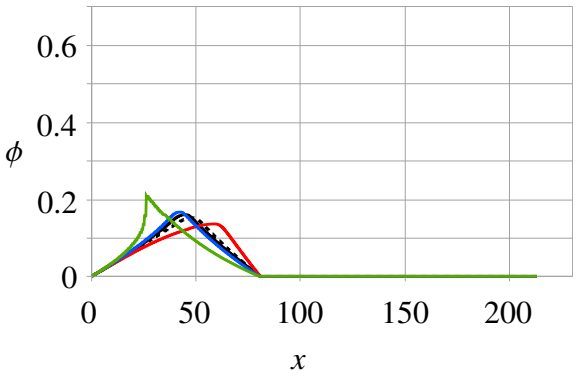

(b) $t = 450$ s

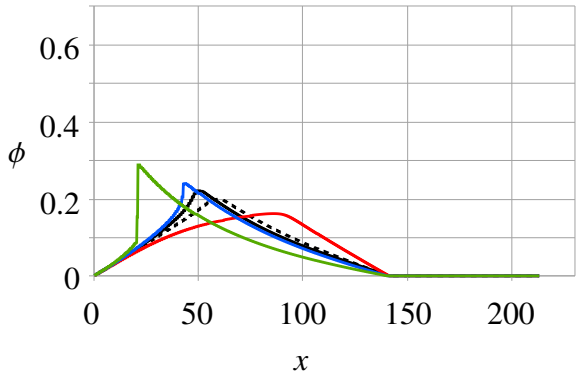

(c) $t = 900$ s

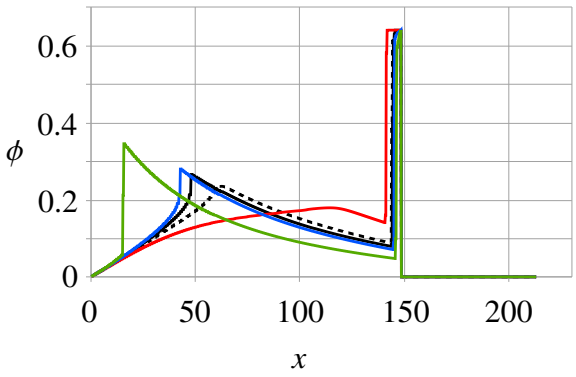

(d) $t = 1350$ s

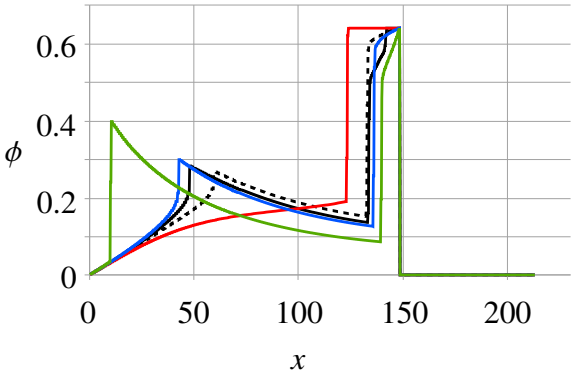

(e) $t = 1800$ s

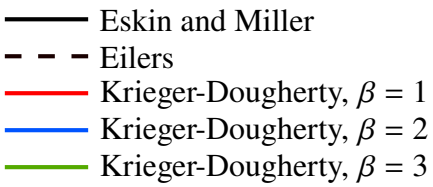

(f)

Figure 3.15: Proppant injection into a KGD fracture over time

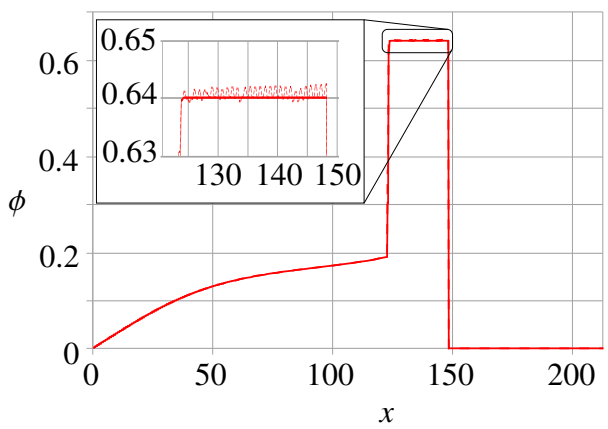

(a) Krieger-Dougherty, $\beta = 1$

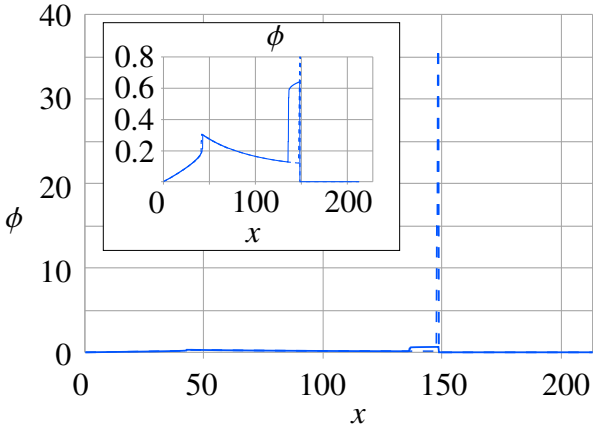

(b) Krieger-Dougherty, $\beta = 2$

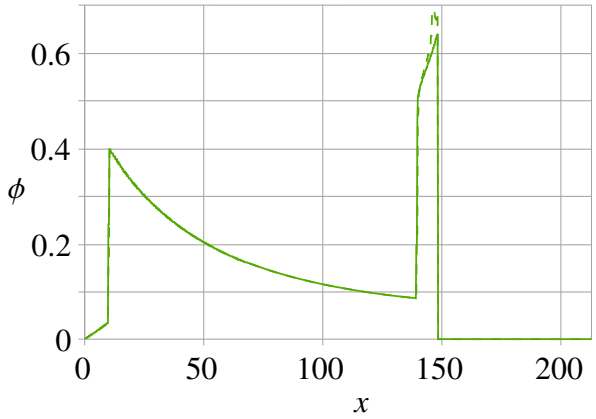

(c) Krieger-Dougherty, $\beta = 3$

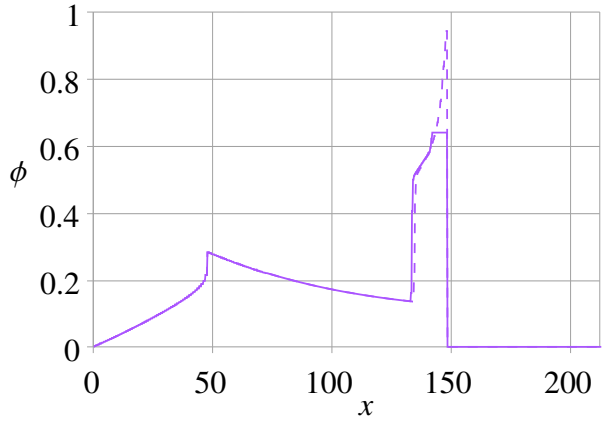

(d) Eskin and Miller

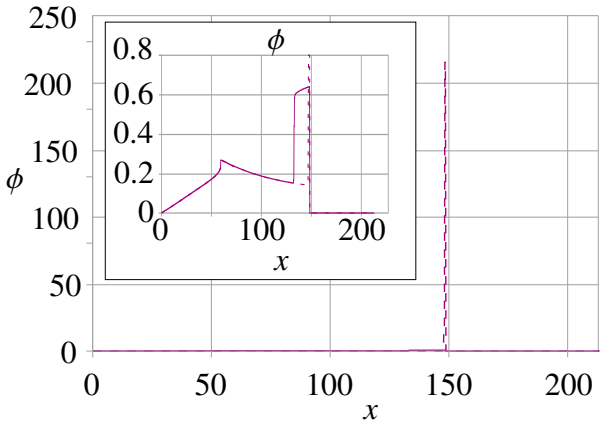

(e) Eilers

Figure 3.16: Proppant concentration at $t = 1800$ s using various effective viscosity formulas with (solid line) and without (dashed line) concentration constraints

Chapter 4

A monolithic coupled hydraulic fracture model with proppant transport

4.1 Introduction

The purpose of this chapter is to present the numerical methodology for solving the monolithic coupled equations for hydraulic fracture propagation with the inclusion of proppant transport and to compare various coupling approaches for hydraulic fracturing simulation. The contribution of this work is to address the gap in the loosely-coupled methods by providing a method where convergence is more rigorously defined. A model is presented which monolithically couples the rock deformation, fluid flow, and proppant transport by simultaneously solving the equations that govern these mechanisms until convergence.

The linear elastic deformation of the discontinuous rock mass is modeled using the extended finite element method (XFEM), including contact and cohesion along the fracture boundaries. The XFEM has been used by researchers to model fractures in both static and dynamic contexts (e.g. Rivas *et al.* [1], Gupta and Duarte [41], Mohammadnejad and Khoei [120], and Gracie and Parchei Esfahani [121]). A mixture model is used to represent the proppant-laden slurry. The flow of fracturing fluid is simulated using the standard finite element method. It includes the transition from Poiseuille flow to Darcy flow as the proppant becomes packed following the approach proposed by Dontsov and Peirce [73]. The flow of fluid in the reservoir is not considered in this paper, which is a reasonable assumption for reservoirs that have low permeability. Additionally, the slurry is assumed to span the length of the fracture without explicitly accounting for fluid lag. This is valid for deep reservoirs that are subject to high confining stresses [15].

Proppant transport through the hydraulic fracture is simulated using the finite volume method with a second-order correction that minimizes numerical dispersion ahead of the proppant front.

Proppant bridging, or obstruction of proppant flow in narrow fractures, is captured in this model. The nonlinear hyperbolic equation that governs proppant transport is characterized by a solution that contains shock waves, or sharp discontinuities, that must be taken into consideration to obtain a correct approximation. The numerical solution of this nonlinear advection equation in the context of hydraulic fracturing is discussed in detail by Rivas and Gracie [2] (Chapter 3). Proppant transport can be ignored in hydraulic fracture models that are only interested in modeling the fracture growth with low leak-off of fracturing fluid into the reservoir. However, proppant transport cannot be ignored for conditions with leak-off in which a tip screen-out may affect the fracture growth. Furthermore, the proppant distribution is essential for simulating the fracture aperture after shut-in.

An injection-rate controlled simulation is achieved by solving global mass conservation, as previously performed by Adachi *et al.* [15], Khoei *et al.* [122], and Parchei Esfahani [123]. In this chapter, a more robust algorithm is presented for improving convergence of the iterative scheme.

The equations that govern the deformation of the solid rock mass and slurry flow through the fractured media are derived in Section 4.2. In Section 4.3, the numerical methods used to approximate each of the governing equations are described. The solution strategies for solving the coupled system of equations and propagating the hydraulic fracture are described in Section 4.4.

Section 4.5 presents numerical results aimed at verifying the code implementation and simulating the slurry-driven propagation of both planar and non-planar fractures. Tip screen-out behavior is investigated to study the interaction between the coupled mechanisms and the results are compared with those of sequential and loose coupling algorithms. The study shows that the monolithic scheme is optimal in terms of computational cost, robustness, and accuracy. The computational cost of a monolithic scheme is comparable to that of a loose coupling scheme and more efficient than a sequential scheme. A sequential coupling scheme maintains accuracy in early times of the simulation but fails to converge after the onset of a tip screen-out. Additionally, it is demonstrated that a loose coupling scheme fails to converge to the same solution as monolithic and sequential schemes. A discussion of results is provided in Section 4.6.

4.2 Governing equations

The governing equations for an impermeable medium containing a slurry-driven fracture are derived in this section. A two-dimensional fracture plane is modeled. Given an *in-situ* vertical stress, σ_v, minimum horizontal stress, σ_h, and maximum horizontal stress, σ_H, the fracture plane under consideration is aligned with the horizontal stresses, as depicted in Figure 4.1. The fracture height is assumed to extend a large distance into the domain such that plane strain conditions apply. The four mechanisms of interest in this hydraulic fracturing model are the rock deformation, fluid

flow, proppant transport, and fracture propagation. The corresponding variables of interest are the fracture aperture, w, the fluid pressure, p, the volumetric concentration of proppant, ϕ, and the fracture length, L, respectively.

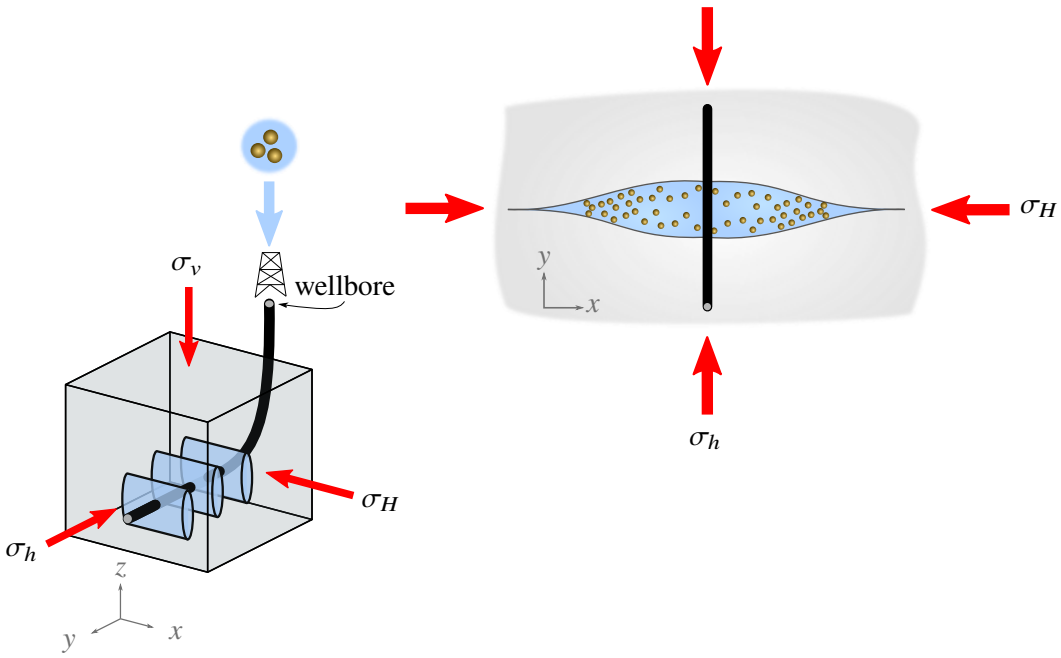

Figure 4.1: Model domain: a two-dimensional domain along the horizontal plane of a fractured rock mass is modeled. The normal of the fracture plane is aligned with the vertical *in-situ* stress. Fracture propagation is driven by slurry flow (a mixture of fracturing fluid and proppant)

4.2.1 Governing equations for the deformation of solid rock mass

The equations that govern the deformation of a fractured rock mass are presented in this section. The rock mass is modeled on a two-dimensional domain, Ω_s, as depicted in Figure 4.2, described on the reference coordinate system $\mathbf{x}$. The domain is enclosed by a boundary, Γ_s, with outward normal vector $\hat{\mathbf{n}}$. The boundary is comprised of mutually exclusive sets Γ_u and Γ_t, corresponding to the Dirichlet and Neumann boundaries, respectively. The domain also contains an internal boundary, Γ_c, pertaining to a fracture surface. The fracture has two faces, denoted by Γ_c^+ and Γ_c^-, with outward normal base vectors $\hat{\mathbf{n}}_{\Gamma_c^+}$ and $\hat{\mathbf{n}}_{\Gamma_c^-}$, respectively. The normal base vector used to describe the internal boundary is $\hat{\mathbf{n}}_{\Gamma_c} = \hat{\mathbf{n}}_{\Gamma_c^-}$, which faces into the domain on the positive fracture face. The deformation of the rock mass, $\mathbf{u}(\mathbf{x})$, is governed by the equilibrium equation

$$\nabla \cdot \boldsymbol{\sigma}(\mathbf{u}) + \mathbf{b} = \mathbf{0}, \quad \forall\, \mathbf{x} \in \Omega_s \tag{4.1}$$

in which $\boldsymbol{\sigma}$ is the Cauchy stress tensor, and $\mathbf{b}$ is the vector of applied body forces. A linear constitutive law of the form $\boldsymbol{\sigma} - \boldsymbol{\sigma}_0 = \mathbf{D} : \boldsymbol{\varepsilon}$ is assumed, in which $\boldsymbol{\sigma}_0$ is the initial stress state, $\mathbf{D}$ is the two-dimensional plane-strain elasticity matrix, and $\boldsymbol{\varepsilon} = \frac{1}{2}(\nabla\mathbf{u} + \nabla\mathbf{u}^\top)$ is the matrix containing the infinitesimal strain. The quasi-static equation of equilibrium is solved assuming a plane strain domain under small deformations. The quasi-steady stress field assumption is valid for this coupled problem since the time scale in which the stress state undergoes changes is larger than the time scale of the slurry flow.

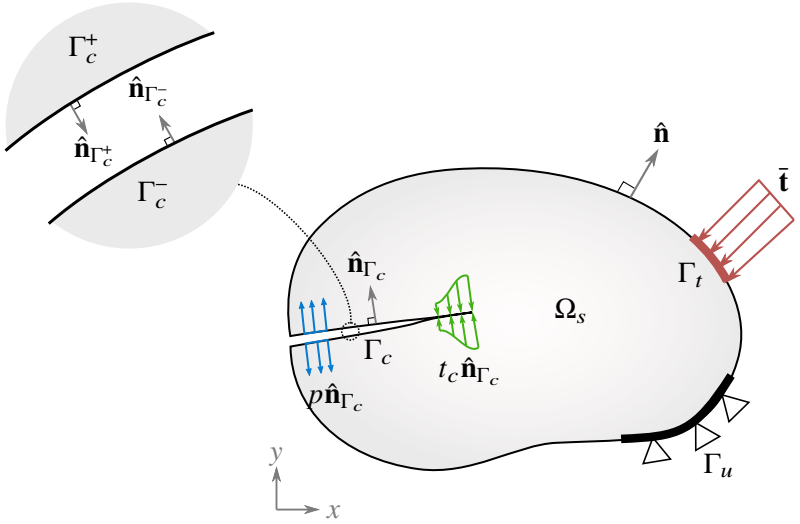

Figure 4.2: Solid rock mass domain

The governing equilibrium equation is a boundary-value problem that requires a Dirichlet boundary condition to obtain a unique solution. The boundary is subject to external tractions, $\bar{\mathbf{t}}$, along the external Neumann boundary, Γ_t, prescribed displacements, $\bar{\mathbf{u}}$, along the Dirichlet boundary, Γ_u, and tractions due to fluid pressure ($p\hat{\mathbf{n}}_{\Gamma_c}$), and contact/cohesive forces ($t_c\hat{\mathbf{n}}_{\Gamma_c}$) along the fracture interface, Γ_c. The fluid pressure is obtained as a part of the solution to the governing equation of the fluid flow, as described in Section 4.2.2, and the constitutive model which describes the contact and cohesive forces are described in the following section. The boundary conditions on the external and internal boundaries are

$$\mathbf{u}(\mathbf{x}) = \bar{\mathbf{u}}, \quad \forall\, \mathbf{x} \in \Gamma_u \tag{4.2}$$

$$\boldsymbol{\sigma} \cdot \hat{\mathbf{n}} = \bar{\mathbf{t}}, \quad \forall\, \mathbf{x} \in \Gamma_t \tag{4.3}$$

$$\boldsymbol{\sigma} \cdot \hat{\mathbf{n}}_{\Gamma_c} = (t_c - p)\hat{\mathbf{n}}_{\Gamma_c}, \quad \forall\, \mathbf{x} \in \Gamma_c \tag{4.4}$$

The weak form of the equilibrium equation is derived by multiplying the governing equation (4.1) by a test function, $\delta\mathbf{u}(\mathbf{x})$, and integrating over the domain, Ω_s [124]. The numerical method used

to solve the weak form of the equilibrium equation is described in Section 4.3.2.

Interface constitutive model

The fracture is subject to contact and cohesive forces that act normal to the fracture surface. Contact forces prevent the non-physical overlap of two fracture surfaces and cohesive forces impede the fracture opening for small apertures. The constitutive model used is similar to the one presented in Section 2.3.1. The magnitude of these forces is dependent on the fracture aperture, $w(\mathbf{x}) = [\![\mathbf{u}(\mathbf{x})]\!] \cdot \hat{\mathbf{n}}_{\Gamma_c}$, which is defined with respect to the jump in displacement along the fracture surface, $[\![\mathbf{u}]\!] = \mathbf{u}|_{\Gamma_c^+} - \mathbf{u}|_{\Gamma_c^-}$. The tractions are applied on either face of the fracture surface with equal magnitude and opposite direction.

$$\boldsymbol{\sigma}^+ \cdot \hat{\mathbf{n}}_{\Gamma_c^+} = -\boldsymbol{\sigma}^- \cdot \hat{\mathbf{n}}_{\Gamma_c^-}, \quad \forall\, \mathbf{x} \in \Gamma_c \tag{4.5}$$

The governing equation (4.1) is satisfied under the constraint that the relative displacement of the fracture surfaces must be non-negative.

$$w(\mathbf{x}) \geq 0, \quad \forall\, \mathbf{x} \in \Gamma_c \tag{4.6}$$

Contact forces are applied using the penalty method to satisfy the above-mentioned constraint, which is akin to placing springs between the two faces of the fracture to prevent them from overlapping. The magnitude of the contact traction is linearly proportional to the magnitude of overlap of the fracture faces, as represented by the left side of the traction-separation curve shown in Figure 4.3. Contact constraints are important at the start of the simulation in which the fracture faces are compressed by the *in-situ* stresses acting on the domain. Contact can be ignored for simulations in which the fracture is filled with fluid and propagating under purely Mode I regime such that the fracture is never in a closed state.

A cohesive-zone model is used to simulate fracture propagation in a ductile rock mass. Fracture formation is conceptualized as the gradual separation of the fracture faces due to plastic deformation at the tip of the fracture. A fracture process zone is assumed to exist near the tip of the fracture which encompasses the region where plastic deformation takes place prior to complete opening of the fracture. Within the fracture process zone, cohesive forces act on the fracture surfaces resisting separation until enough energy is applied to fully open the fracture. Various traction-separation laws have been proposed in the literature for applying cohesive tractions across a fracture [125]. A bilinear intrinsic cohesive model, similar to the one proposed by Geubelle and Baylor [93], is used in this study for cohesion normal to the fracture surface. The magnitude of traction, corresponding to the right side of the traction-separation curve in Figure 4.3, is proportional to the fracture aperture. There is an initial increase in magnitude as the aperture increases until the maximum cohesive traction is reached, equal to the material tensile strength,

f_u. For greater apertures, there is a softening behavior until the fracture completely separates. The traction-separation law is defined as

$$t_c = \begin{cases} f_u \dfrac{w}{w_w}, & w < w_w \\ f_u \left(1 - \dfrac{w - w_w}{w_c - w_w}\right), & w_w \leq w \leq w_c \\ 0, & w > w_c \end{cases} \tag{4.7}$$

in which $w_c = 2G_{Ic}/f_u$ is the aperture at which the fracture surfaces fully separate, and w_w is the weakening aperture, taken between $0.005w_c$ and $0.1w_c$ in this work. The aperture at which the fracture is fully separated is selected such that the area under the traction-separation curve is equal to the Mode I fracture energy,

$$G_{Ic} = \int_0^{w_c} t_c dw \tag{4.8}$$

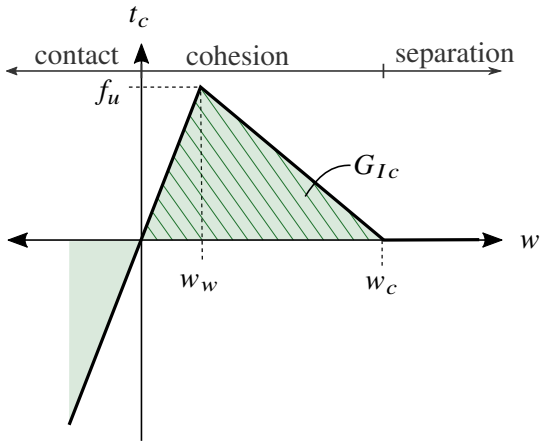

Figure 4.3: Traction-separation law which relates the fracture aperture, w, to the magnitude of cohesive and contact tractions acting along the fracture surface, t_c

4.2.2 Governing equations for the flow of proppant-laden slurry

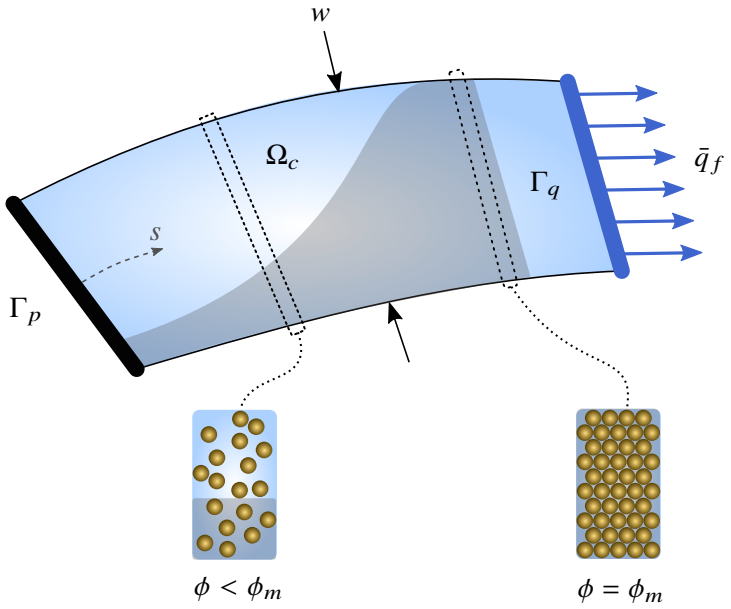

Figure 4.4: Slurry domain

The equations that govern the flow of a proppant-laden slurry through a fracture are presented in this section. Consider a one-dimensional domain, Ω_c, with boundary Γ_f made up of the mutually-exclusive sets Γ_p and Γ_q, corresponding to the Dirichlet and Neumann boundaries of the domain, respectively. The domain is depicted in Figure 4.4. A mixture model is used which assumes that the fluid and proppant phases are fully mixed. There are two variables of interest in the slurry flow: the fluid pressure, p, and the volumetric proppant concentration, ϕ. The variables are taken as average values along the width of the fracture and are varying along the fracture length, s, and time, t. The fracture width, $w(s)$, is obtained from the equilibrium equation (4.1). The equations governing the flow of fluid and proppant are derived from the conservation of mass for each of the phases after assuming that both phases are incompressible. The sum of the conservation of mass of fluid and proppant gives the conservation of slurry mass. Mixture models in the literature typically solve the slurry and proppant conservation equations to obtain the fluid pressure and proppant concentration. In this work, the solution is obtained from the fluid and proppant conservation equations.

$$\text{fluid}: \quad \frac{\partial[(1-\phi)w]}{\partial t} + \frac{\partial q_f}{\partial s} + Q_{leak} = 0 \tag{4.9}$$

$$\text{proppant}: \quad \frac{\partial(\phi w)}{\partial t} + \frac{\partial q_p}{\partial s} = \phi_{inj} Q_{inj} \delta(s - s_0) \tag{4.10}$$

The volumetric fluid flux and proppant fluxes are denoted by q_f and q_p, respectively. The proppant boundary is subject to a prescribed volumetric proppant flux at the fracture inlet, s_0, that is equivalent to the product of the injection rate of the slurry, Q_{inj}, and the concentration of the injected slurry, ϕ_{inj}. Constitutive laws define the relationships between the fluxes, fluid pressure gradient, $\partial p/\partial s$, and proppant concentration. These constitutive laws are described in further detail in the following section. Carter's model is used to approximate the leak-off flux, $Q_{leak}(s,t) = 2c_L/\sqrt{t - t_0(s)}$. This model assumes one-dimensional fluid loss to the rock formation flowing perpendicular to the fracture face due to a constant fluid pressure inside the fracture. The rate of leak-off at any given point along the fracture is proportional to the inverse square root of time, which is measured as the time since the fracturing fluid reached that point, denoted by $t_0(s)$. Leak-off is controlled by the Carter leak-off coefficient, c_L, which depends upon the characteristics of the fracturing fluid used and the reservoir fluids and rock [126]. This model is appropriate only for low-permeability formations, as is assumed in this chapter.

The conservation of fluid mass is a boundary value problem characterized by a diffusion equation. Therefore, the fluid boundary is subject to a prescribed pressure, $\bar{p}$, on the Dirichlet boundary, Γ_p, and a prescribed volumetric flux, $\bar{q}_f$, on the Neumann boundary, Γ_q.

$$p = \bar{p}, \quad \forall\, s \in \Gamma_p \quad \text{subject to: } Q_{inj} = \int_{\Omega_f} \dot{w} d\Omega + \int_{\Omega_f} Q_{leak} d\Omega \tag{4.11}$$

$$q_f = \bar{q}_f, \quad \forall\, s \in \Gamma_q \tag{4.12}$$

In this work, the prescribed pressure is obtained by satisfying global mass conservation in each time step, so that the total change in fracture volume in a time step is equal to the volumetric injection rate at the inlet, Q_{inj}. The procedure for prescribing injection-rate controlled fracture propagation is described in more detail in Section 4.4.2.

The conservation of proppant mass is an initial value problem characterized by an advection equation. It is solved based on an initial proppant concentration profile, which is assumed to be null in the results presented in this chapter. Additionally, equation (4.10) must be solved under the constraint that the proppant concentration must be non-negative and less than the fully saturated proppant concentration, ϕ_m.

$$0 \leq \phi \leq \phi_m \tag{4.13}$$

Values of saturated concentration range from 0.52 for loose-packed spheres [104] to 0.74 for hexagonal close-packing of mono-disperse spherical particles [105]. A value of 0.60 is used in this work.

The weak form of the fluid conservation of mass is derived by multiplying the governing equation (4.9) by a test function, $\delta p(s)$, and integrating over the domain, Ω_c [124]. The numerical method used to solve the weak form of the conservation of fluid mass is described in Section 4.3.3.

Constitutive model of slurry flow

A constitutive law that relates the volumetric fluxes of fluid and proppant to the fluid pressure gradient and proppant concentration is described in this section. Assuming a homogeneous proppant distribution along the width of the fracture, the volumetric flux of the slurry, fluid, and proppant are respectively defined as

$$q = w_f \bar{v} \tag{4.14}$$

$$q_f = (1 - \phi) w_f \bar{v}_f \tag{4.15}$$

$$q_p = \phi w_f \bar{v}_p \tag{4.16}$$

in which the average velocities of the slurry, fluid, and proppant along the fracture width are denoted by $\bar{v}$, $\bar{v}_f$, and $\bar{v}_p$, respectively. Heterogeneous proppant distribution along the fracture width is discussed by Hammond [101]. Due to asperities on the fracture surface, a closed fracture has a residual aperture, w_{res}, within which the slurry may flow. The fracture aperture for slurry flow is defined as

$$w_f = \max(w, w_{res}) \tag{4.17}$$

The average velocities of the two phases of the slurry mixture are defined with respect to two main flow velocities: the velocity of a Newtonian slurry between two parallel plates assuming laminar flow ($\bar{v}_c$) and the velocity of the fracturing fluid through packed proppant particles ($\bar{v}_d$). The two main flow velocities correspond to Poiseuille flow and Darcy flow. The slurry is treated as a Newtonian fluid with an effective viscosity that is dependent on the proppant concentration. The laminar flow velocity, $\bar{v}_c$, stems from the cubic law with a correction for the effective viscosity of the slurry, $\mu(\phi)$.

$$\bar{v}_c = \frac{-w_f^2}{12\mu(\phi)} \frac{\partial p}{\partial s} \tag{4.18}$$

The effective viscosity of the slurry increases with higher proppant concentration, reducing the velocity to zero at a saturated proppant concentration. Various expressions for effective viscosity are proposed in the literature [103]. The role that the effective viscosity plays on the nonlinear advection of proppant through a fracture is discussed by Rivas and Gracie [2] (Chapter 3). The expression proposed by Eilers [108] is used in this work, defined as

$$\mu(\phi) = \mu_0 \left[1 + \frac{1.25\phi}{1 - \phi/\phi_m} \right]^2 \tag{4.19}$$

in which μ_0 is the viscosity of the fracturing fluid. The effective viscosity is equivalent to the pure fluid viscosity at zero proppant concentration and goes to infinity as the proppant concentration reaches the saturation point.

The Darcy flow velocity, $\bar{v}_d$, is the velocity of the fracturing fluid through packed proppant that has become immobilized. The Carman-Kozeny equation [127, 128] is used to relate the mean flow velocity of the fluid to the proppant concentration, fluid pressure gradient, and average proppant particle radius, a. This equation assumes that fluid is moving through a packed proppant bed of unconsolidated, spherical grains.

$$\bar{v}_d = -\frac{(2a)^2}{180\mu_0}\frac{(1-\phi_m)^3}{\phi_m^2}\frac{\partial p}{\partial s} \tag{4.20}$$

In accordance with the definition of the mass-averaged slurry velocity ($\rho\bar{v} = \phi\rho_p\bar{v}_p + (1-\phi)\rho_f\bar{v}_f$), the average slurry, fluid, and proppant velocities are defined as

$$\bar{v} = \bar{v}_c + \left[(1-\phi)\frac{\rho_f}{\rho}\right]\frac{\phi}{\phi_m}\bar{v}_d \tag{4.21}$$

$$\bar{v}_f = \left[1 - \frac{\phi}{1-\phi}\frac{\rho_p}{\rho_f}(B(w_f)-1)\right]\bar{v}_c + \frac{\phi}{\phi_m}\bar{v}_d \tag{4.22}$$

$$\bar{v}_p = B(w_f)\bar{v}_c \tag{4.23}$$

The densities of the slurry, fluid, and proppant are denoted by ρ, ρ_f, and ρ_p, respectively. The first term in each of the velocity definitions (4.21-4.23) is related to the laminar slurry flow term, $\bar{v}_c$. The laminar flow of proppant is hindered by a bridging function, $B(w_f) = H\,(w_f/2a > n_{dia})$, which prevents proppant from entering fracture apertures that are too narrow. The threshold fracture width at which the particles form a bridge is specified as a number of proppant diameters, n_{dia} [116]. In this work, the proppant is restricted from flowing through a fracture aperture smaller than three proppant diameters in size. The laminar flow term in the fluid velocity definition is corrected so that the definition of mass-averaged velocity holds.

The second term in the definition of slurry and fluid velocities (4.21-4.22) is related to the flow of fluid through packed proppant, $\bar{v}_d$. As the proppant concentration reaches the saturated amount, the laminar flow term becomes negligible and the Darcy flow term dominates. The Darcy flow term increases proportionally with increasing proppant concentration until reaching the saturated amount. The proppant is unaffected by the Darcy velocity term since it does not flow at the saturated concentration. The Darcy flow term in the slurry velocity is corrected to satisfy the definition of mass-averaged velocity.

Assuming a homogeneous proppant distribution along the width of the fracture and using the velocity definitions (4.22-4.23), the volumetric flux of the fluid and proppant are defined as,

$$q_f = -(1-\phi)k_f\frac{\partial p}{\partial s} \tag{4.24}$$

$$q_p = -\phi k_p\frac{\partial p}{\partial s} \tag{4.25}$$

in which the fluid and proppant conductivities are respectively defined as

$$k_f = \frac{w_f^3}{12\mu(\phi)}\left(1 - \frac{\phi}{1-\phi}\frac{\rho_p}{\rho_f}(B(w_f) - 1)\right) + \frac{w_f a^2}{45\mu_0}\frac{(1-\phi_m)^3}{\phi_m^2}\frac{\phi}{\phi_m} \tag{4.26}$$

$$k_p = \frac{w_f^3}{12\mu(\phi)}B(w_f) \tag{4.27}$$

The variation of the fluid and proppant fluxes with respect to proppant concentration and fracture apertures are shown in Figures 4.5 and 4.6, respectively. For negligible proppant concentration ($\phi \to 0$), the slurry flow is solely laminar fluid flow. In the other limit, as the proppant concentration becomes saturated ($\phi \to \phi_m$), the slurry flow is solely Darcy flow of the fluid through the packed proppant bed. It is important to note that Equation 4.19 is singular for a saturated proppant concentration ($\phi = \phi_m$). To overcome the numerical challenges of a singular expression, the viscosity is factored into the conductivity expressions (4.26-4.27) to obtain a final expression that has a finite value in the entire range of permissible proppant concentrations.

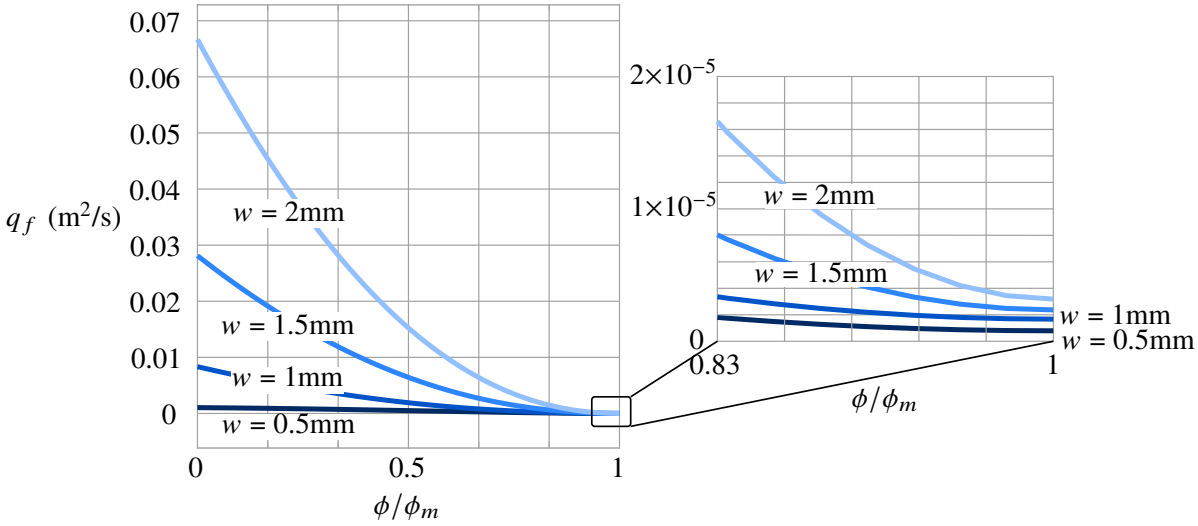

Figure 4.5: Fluid flux for varying fracture apertures as a function of proppant concentration, plotted using $\phi_m = 0.6$, $\delta p/\delta s = -100$ kPa, $\mu_0 = 0.001$ Pa·s, $a = 0.6$, $\rho_p = 2650$ kg/m^3, and $\rho_f = 1000$ kg/m^3

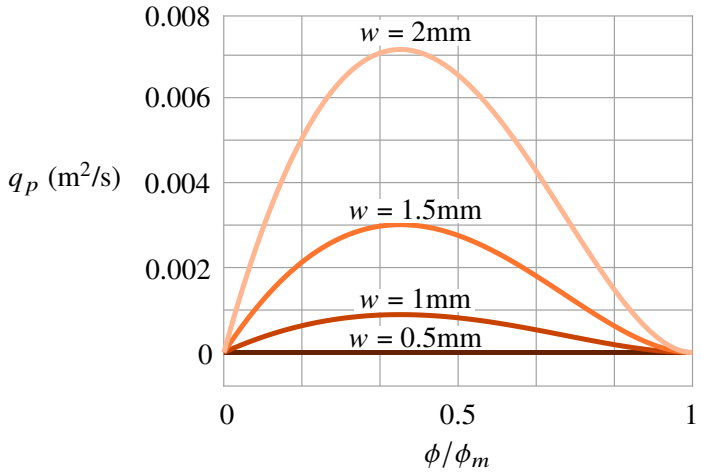

Figure 4.6: Proppant flux for varying fracture apertures as a function of proppant concentration, plotted using $\phi_m = 0.6$, $\delta p/\delta s = -100$ kPa, $\mu_0 = 0.001$ Pa·s, $a = 0.6$, $\rho_p = 2650$ kg/m^3, and $\rho_f = 1000$ kg/m^3

4.3 Numerical methodology

In this section, the numerical methodology used to approximate the governing equations are described. Three different methods are used to solve the three governing equations: the equilibrium equation governing rock deformation (4.1) is approximated using the extended finite element method (XFEM); the conservation of fluid mass (4.9) is approximated using the standard finite element method (FEM); and the conservation of proppant mass (4.10) is approximated using the finite volume method (FVM). The discretization of the three domains is first described, followed by the approximation of rock deformation, fluid pressure, and proppant concentration.

4.3.1 Discretization

Quadrilateral elements are used to discretize the solid rock domain. A fracture is defined in the domain using linear segments that span between the edges of the solid mesh elements, as depicted in Figure 4.7. The standard FEM nodes for the approximation of the rock displacement field are represented by white circles in the figure. Using the XFEM, the displacement field of the rock mass is discontinuous along the fracture. An enrichment function is used on additional degrees of freedom located at nodes surrounding the fracture to capture the discontinuity. Nodes that contain enriched degrees of freedom are represented by dark-gray circles in the figure.

The fluid domain is discretized into one-dimensional linear elements, which coincide with the explicit description of the fracture. The nodes of each fluid element, depicted by blue squares in Figure 4.7, are located on the edges of the solid elements. The proppant domain is discretized into one-dimensional finite volume cells, such that the edges of each cell coincide with the edges of a fluid element. The proppant concentration is approximated at a node located at the center of each finite volume cell, depicted by a red triangle in Figure 4.7.

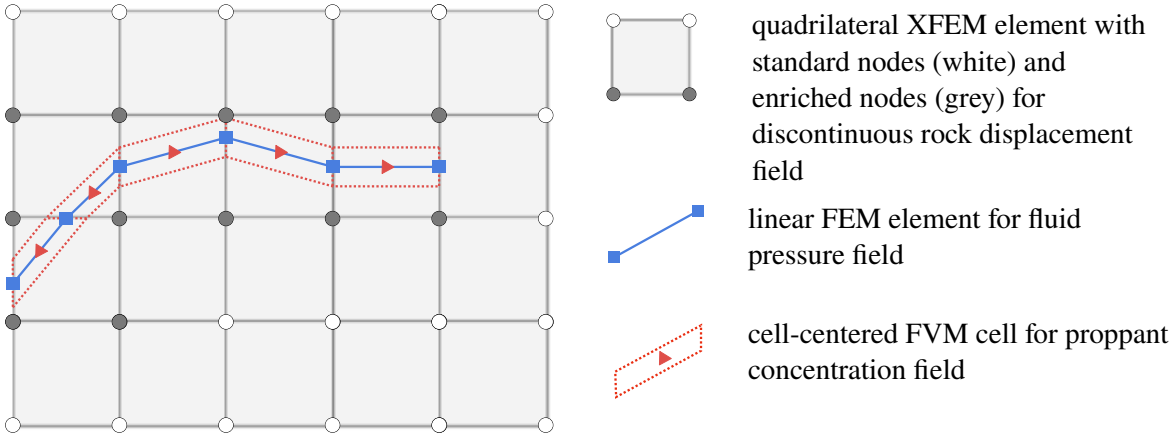

Figure 4.7: Discretized domains for the governing equations of rock deformation, fluid flow and proppant transport

4.3.2 XFEM approximation of the rock deformation

The XFEM is used to approximate the deformation of the fractured rock mass. Additional information on the XFEM can be found in papers by Moës *et al.* [34], Dolbow *et al.* [50], Lecampion [87], Khoei *et al.* [122], and Rivas *et al.* [1]. The rock displacement field is approximated by a discontinuous function, defined by enriching the shape functions of nodes that are adjacent to fractures in the domain. For each element, the approximation of the rock displacement is expressed as

$$\mathbf{u}^h(\mathbf{x}) = \sum_{I \in S_n} N_I(\mathbf{x}) \tilde{\mathbf{u}}_I + \sum_{J \in S_c} N_J(\mathbf{x}) \Psi_J(\mathbf{x}) \tilde{\mathbf{a}}_J \equiv \mathbf{N}(\mathbf{x}) \mathbf{d} \tag{4.28}$$

in which S_n is the set of all nodes in each element and S_c is the set of nodes that have a nodal support cut by the fracture. The vectors of nodal displacement on the standard and enriched degrees of freedom of node I are denoted by $\tilde{\mathbf{u}}_I$ and $\tilde{\mathbf{a}}_I$, respectively. The standard finite element shape functions for each node I are denoted by $N_I(\mathbf{x})$ and enrichment functions are denoted as $\Psi_I(\mathbf{x})$.

In the matrix form of the approximation, $\mathbf{N}(\mathbf{x})$ is a matrix that contains the shape functions corresponding to both the standard and enriched degrees of freedom in each element. Similarly,

the column matrix, $\mathbf{d}$, contains the displacements on both the standard and enriched degrees of freedom. The strain is approximated by

$$\boldsymbol{\varepsilon}^h(\mathbf{x}) = \nabla^s \mathbf{u}^h(\mathbf{x}) \equiv \mathbf{B}(\mathbf{x})\mathbf{d} \tag{4.29}$$

in which $\mathbf{B}$ is the matrix containing the derivatives of the shape functions for both the standard and enriched degrees of freedom. The use of quadrilateral elements results in a bilinear approximation of the displacement along each element. To model discontinuities in the displacement field along the fracture surface, a shifted Heaviside enrichment function is used at each enriched node, J, defined as

$$\Psi_J(\mathbf{x}) = H(\mathbf{x}) - H(\mathbf{x}_J) \tag{4.30}$$

in which $H(\mathbf{x})$ is the Heaviside step function that differentiates between the two sides of the fracture,

$$H(\mathbf{x}) = \begin{cases} 0, & (\mathbf{x} - \mathbf{x}_{tip}) \cdot \hat{\mathbf{n}}_{\Gamma_c} < 0 \\ 1, & (\mathbf{x} - \mathbf{x}_{tip}) \cdot \hat{\mathbf{n}}_{\Gamma_c} \geq 0 \end{cases} \tag{4.31}$$

The function checks the distance between a point in the domain and the fracture tip, $\mathbf{x}_{tip}$, in the direction normal to the fracture surface and assigns a value to either side. The Heaviside enrichment at each node is shifted by the Heaviside function evaluated at the corresponding node to satisfy the Kronecker-δ property. Using the enriched approximation, the fracture aperture is defined as

$$w(\mathbf{x}) = [\![\mathbf{u}(\mathbf{x})]\!] \cdot \hat{\mathbf{n}}_{\Gamma_c} = \hat{\mathbf{n}}_{\Gamma_c}^\top [\![\mathbf{N}(\mathbf{x})]\!]\mathbf{d} \tag{4.32}$$

The discretized system of equations is obtained by inserting the approximation (4.28) and a test function of a similar form into the weak form of the equation governing rock deformation,

$$\underbrace{\left[\int_{\Omega_s} \mathbf{B}^\top \mathbf{D}\mathbf{B} d\Omega\right]\mathbf{d}}_{\mathbf{F}^{int}} + \underbrace{\left[\int_{\Gamma_c} [\![\mathbf{N}]\!]^\top \left(t_c \hat{\mathbf{n}}_{\Gamma_c} - \boldsymbol{\sigma}_0 \cdot \hat{\mathbf{n}}_{\Gamma_c}\right) d\Gamma\right]}_{\mathbf{F}^c} - \underbrace{\left[\int_{\Gamma_c} [\![\mathbf{N}]\!]^\top \hat{\mathbf{n}}_{\Gamma_c} p d\Gamma\right]}_{\mathbf{F}^p} - \underbrace{\left[\int_{\Omega_s} \mathbf{N}^\top \mathbf{b} d\Omega + \int_{\Gamma_t} \mathbf{N}^\top \bar{\mathbf{t}} d\Gamma\right]}_{\mathbf{F}^{ext}} = \mathbf{0} \tag{4.33}$$

The integral terms are written in terms of the column matrices representing the internal forces $\mathbf{F}^{int}$, cohesive and contact forces $\mathbf{F}^c$, pressure forces $\mathbf{F}^p$, and external forces $\mathbf{F}^{ext}$. The magnitude of the contact and cohesive tractions, t_c, are defined by the traction-separation law in Equation 4.7, and the approximation of fluid pressure, p, is described in Section 4.3.3. The fracture surfaces

are also subject to *in-situ* stresses, $\boldsymbol{\sigma}_0$.

4.3.3 FEM approximation of the fluid flow

The standard FEM is used to approximate the equation governing fluid flow through a fracture. In each fluid element, the approximation of the fluid pressure, p^h, and pressure gradient, $p^h_{,s}$, are expressed as

$$p^h(s,t) = \mathbf{N}_f(s)\mathbf{p}(t) \tag{4.34}$$

$$p^h_{,s}(s,t) = \mathbf{B}_f(s)\mathbf{p}(t) \tag{4.35}$$

in which $\mathbf{N}_f$ and $\mathbf{B}_f$ are the matrices containing the standard FEM shape functions and derivatives of the shape functions for the degrees of freedom in each element, respectively. The column matrix containing the nodal pressures is denoted by $\mathbf{p}(t)$. Linear elements are used for the pressure field, which results in a linearly-varying pressure field along the fracture and constant pressure gradients in each element.

The semi-discrete system of equations is obtained by inserting the approximation (4.34) and a test function of a similar form into the weak form of the equation governing fluid flow and integrating over all fluid elements. An implicit backward Euler scheme is used to integrate the storage term over time to obtain the following discrete system of equations,

$$\underbrace{\left[\int_{\Omega_c} \mathbf{B}_f^\top q_f^n ds\right]}_{\mathbf{F}^d} - \frac{1}{\Delta t^n}\underbrace{\left[\int_{\Omega_c} \mathbf{N}_f^\top \Delta[(1-\phi)w] ds\right]}_{\mathbf{F}^s} - \underbrace{\left[\int_{\Omega_c} \mathbf{N}_f^\top Q_{leak}^n ds\right]}_{\mathbf{F}^l} - \underbrace{\left[\left(\mathbf{N}_f^\top \bar{q}_f^n\right)\Big|_{\Gamma_q}\right]}_{\mathbf{F}^f} = \mathbf{0} \tag{4.36}$$

in which $\Delta t^n = t^n - t^{n-1}$ is the time step and $\Delta[(1-\phi)w] = (1-\phi^n)w^n - (1-\phi^{n-1})w^{n-1}$ is the change in fluid storage in the aperture. The constitutive law of the fluid flux defined in Equation 4.24 relates the flux to the fluid pressure. The integral terms are written in terms of the column matrices representing the diffusive fluxes, $\mathbf{F}^d$, storage fluxes, $\mathbf{F}^s$, leak-off fluxes, $\mathbf{F}^l$, and source fluxes, $\mathbf{F}^f$. The approximation of the fracture aperture, w, and proppant concentration, ϕ, are discussed in Sections 4.3.2 and 4.3.4, respectively.

4.3.4 FVM approximation of proppant transport

The FVM is used to approximate the conservation of proppant mass throughout the fracture. Details of the numerical method used to solve the nonlinear and heterogeneous advection of proppant through a fracture are elaborated upon in Rivas and Gracie [2] (Chapter 3). The fracture

is first discretized into N finite volume cells, as depicted in Figure 4.8. The equation governing the conservation of proppant mass (4.10) is integrated over the length of a finite volume cell, Δs, and a time step, Δt^n. The discrete equation is obtained by using the midpoint integration rule for the spatial integral and an explicit forward Euler scheme for time integration,

$$\phi_i^n w_i^n = \phi_i^{n-1} w_i^{n-1} - \frac{\Delta t^n}{\Delta s}\left[q_{p_{i+1/2}}^{n-1} - q_{p_{i-1/2}}^{n-1}\right], \quad \forall\, i \in [0, N] \tag{4.37}$$

This equation describes advection of the propped fracture width (ϕw). The approximation for the proppant concentration at the center of cell i at time t^n is denoted by ϕ_i^n. A piecewise constant approximation of proppant concentration is assumed in each cell. The discrete equation uses the approximate fracture aperture, w_i^n, and fluid pressure, p_i^n, at the center of the cell obtained using Equations 4.32 and 4.34, respectively. The proppant fluxes at the cell edges at time t^{n-1} are denoted by $q_{p_{i\pm1/2}}^{n-1}$. The difficulty in the finite volume method is the approximation of the cell edge fluxes, which is described in 3.3.4.

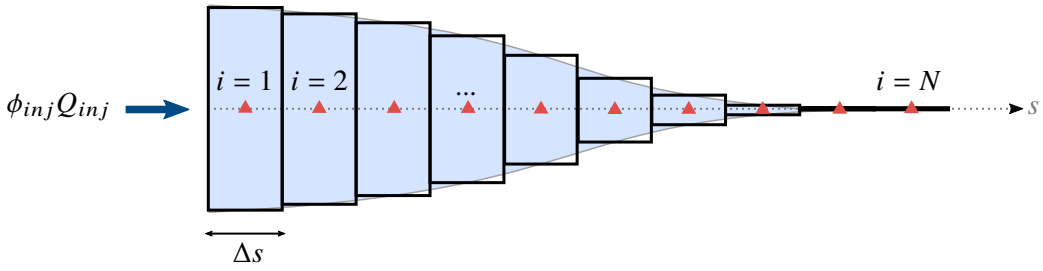

Figure 4.8: Finite volume cells along the fracture length

The matrix form of the discrete system of equations (4.37) is

$$\underbrace{\mathbf{W}\left(\mathbf{d}^n\right)\boldsymbol{\phi}^n - \mathbf{W}\left(\mathbf{d}^{n-1}\right)\boldsymbol{\phi}^{n-1}}_{\mathbf{F}^{ps}} + \underbrace{\frac{\Delta t^n}{\Delta s}\Delta\mathbf{F}^a\left(\mathbf{d}^{n-1}, \mathbf{p}^{n-1}, \boldsymbol{\phi}^{n-1}\right)}_{\mathbf{F}^{advect}} = \mathbf{0} \tag{4.38}$$

in which $\mathbf{W}(\mathbf{d})$ is a diagonal matrix containing the fracture aperture at the center of each cell along its diagonal and $\boldsymbol{\phi}$ is a column matrix containing the proppant concentration at each of the finite volume cells. The column matrix $\Delta\mathbf{F}^a$ contains the difference between the proppant flux at the cell edges for each cell. The equation is written in terms of the column matrices representing the proppant storage flux, $\mathbf{F}^{ps}$, and the advection flux of the propped width, $\mathbf{F}^{advect}$.

The explicit time integration method imposes a constraint on the time step according to the Courant-Friedrichs-Lewy (CFL) stability condition, $\Delta t^n \leq \Delta t_{prop}^n$. The largest time step permis-

sible is approximated using the maximum slurry viscosity as

$$\Delta t^n_{prop} = \min_{i \in [0,N]} \frac{\Delta s_i}{\frac{-\left(w^n_i\right)^2}{12\mu_0}\frac{\partial p^n_i}{\partial s}} \tag{4.39}$$

The maximum time step size is proportional to the element size, and inversely proportional to the fracture aperture and pressure gradient. It does not depend on the proppant concentration.

The model presented in this chapter uses an explicit time integration algorithm to solve the proppant transport equations. Nevertheless, it is also possible to update the proppant concentrations using the estimates of aperture and pressure from the current time step to approximate the fluxes at the cell edges with the following equation,

$$\phi^n_i w^n_i = \phi^{n-1}_i w^{n-1}_i - \frac{\Delta t^n}{\Delta s}\left[q^n_{p_{i+1/2}} - q^n_{p_{i-1/2}}\right], \quad \forall\, i \in [0, N] \tag{4.40}$$

Since the flux approximation depends on the unknown proppant concentration at the current time step, this is considered a quasi-implicit scheme. A comparison of results using the quasi-implicit scheme and the explicit scheme is provided in Section 4.5.2.

Concentration constraints

A predictor-corrector algorithm is used to constrain the proppant concentration within the physically-admissible range such that $\phi \in [0, \phi_m]$ as proposed by Rivas and Gracie [2] (Chapter 3). The concentration is obtained using Equation 4.37 in a predictor step with the flux approximations described in 3.3.4. Then, the set of cells with predicted concentrations outside of the physically-admissible range are identified and the flux approximation is corrected so that the proppant concentration is exactly at the limit. The neighboring cell fluxes are also updated to maintain the conservation property of the finite volume method.

4.3.5 Coupled system of equations

Combining the discrete equations for the solid (4.33), fluid (4.36), and proppant (4.38) domains gives the coupled system of discrete equations in terms of the residuals for the solid deformation,

$\mathbf{R}_d^n$, fluid pressure, $\mathbf{R}_p^n$, and proppant concentration, $\mathbf{R}_\phi^n$, at time t^n.

$$\begin{aligned}
\mathbf{R}_d^n &= \mathbf{F}^{int}(\mathbf{d}^n) + \mathbf{F}^c(\mathbf{d}^n) - \mathbf{F}^p(\mathbf{p}^n) + \mathbf{F}^{ext} = \mathbf{0} \\
\mathbf{R}_p^n &= \mathbf{F}^d(\mathbf{d}^n, \mathbf{p}^n, \boldsymbol{\phi}^n) - \frac{1}{\Delta t}\mathbf{F}^s(\Delta\mathbf{d}, \Delta\boldsymbol{\phi}) - \mathbf{F}^l - \mathbf{F}^f = \mathbf{0} \\
\mathbf{R}_\phi^n &= \mathbf{F}^{ps}\left(\mathbf{d}^n, \boldsymbol{\phi}^n, \mathbf{d}^{n-1}, \boldsymbol{\phi}^{n-1}\right) + \mathbf{F}^{advect}\left(\mathbf{d}^{n-1}, \mathbf{p}^{n-1}, \boldsymbol{\phi}^{n-1}\right) = \mathbf{0}
\end{aligned} \tag{4.41}$$

The strategy used to solve this system of equations is detailed in the following section.

4.4 Solution strategies

In this section, the solution strategies used in simulating the propagation of a hydraulic fracture due to slurry injection are described. A flow chart of the numerical algorithm is provided in Figure 4.9. There are three main loops in the algorithm: a time loop (Section 4.4.4), an external loop used to approximate the pressure at the Dirichlet boundary required to control the injection rate (Section 4.4.2), and an internal loop used to solve the discrete system of equations (Section 4.4.1). Once a converged solution is achieved for the desired injection rate, the fracture is propagated as described in Section 4.4.3 before starting a new time step. Each part of the algorithm is detailed in the following sections.

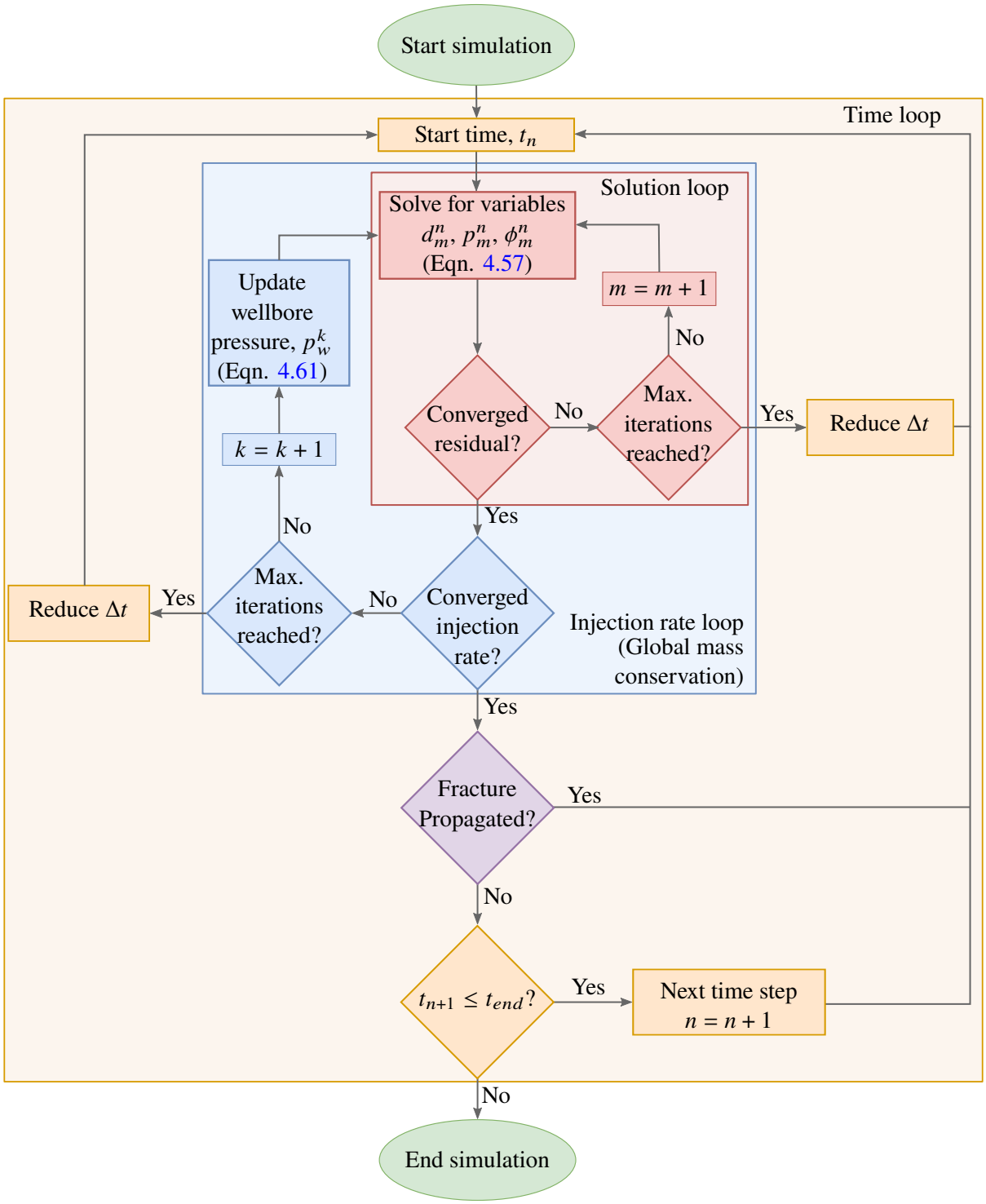

Figure 4.9: Solution algorithm flowchart

4.4.1 Coupled solution algorithm (inner loop)

Monolithic coupling

A robust fully-coupled scheme is developed for the first time in this work. A Newton-Raphson iterative method is used to solve the coupled system of equations. For a given time, t^n, the solution is approximated iteratively, corresponding to the red-filled box in Figure 4.9. The discrete system of equations (4.41) is linearized for a given iteration, m, using a first-order truncated Taylor expansion about the solution in the form

$$\mathbf{R}_m^n + \mathbf{J}_m^n \Delta \boldsymbol{\psi}_m^n = \mathbf{0} \tag{4.42}$$

in which $\mathbf{R}_m^n = \begin{bmatrix} \mathbf{R}_d^n & \mathbf{R}_p^n & \mathbf{R}_\phi^n \end{bmatrix}^\top$ is the column matrix of residuals evaluated from the solution at time t^n, and $\boldsymbol{\psi}_m^n = \begin{bmatrix} \mathbf{d}_m^n & \mathbf{p}_m^n & \boldsymbol{\phi}_m^n \end{bmatrix}^\top$ is the column matrix of independent variables. The Jacobian matrix, $\mathbf{J}_m^n$, contains the first partial derivative of the residual components with respect to the independent variables, defined as

$$\mathbf{J}_m^n = \begin{bmatrix} \dfrac{\partial \mathbf{R}_d^n}{\partial \mathbf{d}^n} & \dfrac{\partial \mathbf{R}_d^n}{\partial \mathbf{p}^n} & \dfrac{\partial \mathbf{R}_d^n}{\partial \boldsymbol{\phi}^n} \\ \dfrac{\partial \mathbf{R}_p^n}{\partial \mathbf{d}^n} & \dfrac{\partial \mathbf{R}_p^n}{\partial \mathbf{p}^n} & \dfrac{\partial \mathbf{R}_p^n}{\partial \boldsymbol{\phi}^n} \\ \dfrac{\partial \mathbf{R}_\phi^n}{\partial \mathbf{d}^n} & \dfrac{\partial \mathbf{R}_\phi^n}{\partial \mathbf{p}^n} & \dfrac{\partial \mathbf{R}_\phi^n}{\partial \boldsymbol{\phi}^n} \end{bmatrix}_m = \begin{bmatrix} \mathbf{K}_{dd} + \mathbf{K}_c & -\mathbf{K}_{dp} & 0 \\ \mathbf{K}_{pd} - \dfrac{1}{\Delta t}\mathbf{K}_{sd} & \mathbf{K}_{pp} & \mathbf{K}_{p\phi} - \dfrac{1}{\Delta t}\mathbf{K}_{s\phi} \\ \mathbf{K}_{\phi d} & 0 & \mathbf{K}_{\phi\phi} \end{bmatrix}_m^n \tag{4.43}$$

The terms in the matrix are

$$\mathbf{K}_{dd} = \frac{\partial \mathbf{F}^{int}}{\partial \mathbf{d}^n} = \int_\Omega \mathbf{B}^\top \mathbf{D} \mathbf{B} d\Omega \tag{4.44}$$

$$\begin{aligned} \mathbf{K}_c &= \frac{\partial \mathbf{F}^c}{\partial \mathbf{d}^n} = \frac{\partial \mathbf{F}^c}{\partial t_c} \frac{\partial t_c}{\partial w} \frac{\partial w}{\partial \mathbf{d}^n} \\ &= \left[\int_{\Gamma_c} [\![\mathbf{N}]\!]^\top \hat{\mathbf{n}}_{\Gamma_c} \frac{\partial t_c}{\partial w} \hat{\mathbf{n}}_{\Gamma_c}^\top [\![\mathbf{N}]\!] d\Gamma \right] \end{aligned} \tag{4.45}$$

$$\mathbf{K}_{dp} = \frac{\partial \mathbf{F}^p}{\partial \mathbf{p}^n} = \int_{\Gamma_c} [\![\mathbf{N}]\!]^\top \hat{\mathbf{n}}_{\Gamma_c} \mathbf{N}_f d\Gamma \tag{4.46}$$

$$\begin{aligned}\mathbf{K}_{pd} &= \frac{\partial \mathbf{F}^d}{\partial \mathbf{d}^n} = \frac{\partial \mathbf{F}^d}{\partial q_f}\frac{\partial q_f}{\partial k_f}\frac{\partial k_f}{\partial w}\frac{\partial w}{\partial \mathbf{d}^n} \\ &= \left[\int_{\Omega_f} \mathbf{B}_f^\top(\phi^n - 1)\frac{\partial k_f}{\partial w}\mathbf{B}_f \mathbf{p}^n \hat{\mathbf{n}}_{\Gamma_c}^\top [\![\mathbf{N}]\!] ds\right] \end{aligned} \tag{4.47}$$

$$\begin{aligned}\mathbf{K}_{sd} &= \frac{\partial \mathbf{F}^s}{\partial \mathbf{d}^n} = \frac{\partial \mathbf{F}^s}{\partial w^n}\frac{\partial w^n}{\partial \mathbf{d}^n} \\ &= \int_{\Omega_f} \mathbf{N}_f^\top(1-\phi^n)\hat{\mathbf{n}}_{\Gamma_c}^\top [\![\mathbf{N}]\!] ds \end{aligned} \tag{4.48}$$

$$\begin{aligned}\mathbf{K}_{pp} &= \frac{\partial \mathbf{F}^d}{\partial \mathbf{p}^n} = \frac{\partial \mathbf{F}^d}{\partial q_f}\frac{\partial q_f}{\partial \mathbf{p}^n} \\ &= \left[\int_{\Omega_f} \mathbf{B}_f^\top(\phi^n - 1)k_f \mathbf{B}_f ds\right] \end{aligned} \tag{4.49}$$

$$\begin{aligned}\mathbf{K}_{p\phi} &= \frac{\partial \mathbf{F}^d}{\partial \boldsymbol{\phi}^n} = \frac{\partial \mathbf{F}^d}{\partial q_f}\frac{\partial q_f}{\partial \boldsymbol{\phi}^n} \\ &= \int_{\Omega_f} \mathbf{B}_f^\top \left(k_f - (1-\phi^n)\frac{\partial k_f}{\partial \phi}\right)\mathbf{B}_f \mathbf{p}^n ds \end{aligned} \tag{4.50}$$

$$\mathbf{K}_{s\phi} = \frac{\partial \mathbf{F}^s}{\partial \boldsymbol{\phi}^n} = -\left(\int_{\Omega_f} \mathbf{N}_f^\top w ds\right) \tag{4.51}$$

$$\begin{aligned}\mathbf{K}_{\phi d} &= \frac{\partial \mathbf{F}^{ps}}{\partial \mathbf{d}^n} = \frac{\partial \mathbf{W}}{\partial \mathbf{d}^n}\boldsymbol{\phi}^n \\ K_{\phi d,i} &= \phi_i \hat{\mathbf{n}}_{\Gamma_c}^\top [\![\mathbf{N}(\mathbf{x}(s_i))]\!] \end{aligned} \tag{4.52}$$

$$\mathbf{K}_{\phi\phi} = \frac{\partial \mathbf{F}^{ps}}{\partial \boldsymbol{\phi}^n} = \mathbf{W}\left(\mathbf{d}^n\right) \tag{4.53}$$

The differential terms in the integrals are specified as,

$$\frac{\partial t_c}{\partial w} = \begin{cases} \dfrac{f_u}{0.1w_c}, & w < 0.1w_c \\ \dfrac{-f_u}{0.9w_c}, & 0.1w_c < w < w_c \\ 0, & w > w_c \end{cases} \tag{4.54}$$

$$\frac{\partial k_f}{\partial w} = \left\{ \frac{w^2}{4\mu(\phi)} \left[1 - \frac{\phi}{1-\phi} \frac{\rho_p}{\rho_f} (B(w) - 1) \right] + \frac{a^2}{45\mu_0} \frac{(1-\phi_m)^3}{\phi_m^2} \frac{\phi}{\phi_m} \right\} \tag{4.55}$$

$$\begin{aligned} \frac{\partial k_f}{\partial \phi} = \Bigg\{ & \frac{-w^3\mu'}{12\mu(\phi)^2} \left[1 - \frac{\phi}{1-\phi} \frac{\rho_p}{\rho_f} (B(w) - 1) \right] + \frac{w^3}{12\mu(\phi)} \frac{1}{(1-\phi)^2} \frac{\rho_p}{\rho_f} (B(w) - 1) \\ & + \frac{wa^2}{45\mu_0} \frac{(1-\phi_m)^3}{\phi_m^3} \Bigg\} \end{aligned} \tag{4.56}$$

For each successive iteration, the independent variables are updated by

$$\boldsymbol{\psi}_m^n = \boldsymbol{\psi}_{m-1}^n + \Delta\boldsymbol{\psi}_{m-1}^n \tag{4.57}$$

The iterative scheme is continued until the vector norm of the residual is less than a specified tolerance, $\epsilon_{tol,a}$, or when the residual norm has been reduced by a specified ratio from the norm of the first iteration, $\epsilon_{tol,b}$.

$$\|\mathbf{R}_m^n\| \leq \epsilon_{tol,a} \quad \text{or} \quad \|\mathbf{R}_m^n\| \leq \epsilon_{tol,b} \|\mathbf{R}_1^n\| \tag{4.58}$$

In the numerical results shown in this chapter, the tolerances used are $\epsilon_{tol,a} = 10^{-8}$ and $\epsilon_{tol,b} = 10^{-10}$.

Sequential and loose coupling

A comparison of the proposed monolithic coupling with sequential and loose coupling schemes is performed in Section 4.5.2. In the sequential scheme, the solid and fluid degrees of freedom are first solved simultaneously using a Newton-Raphson iteration with fixed values of proppant concentration from the previous time step or iteration. The Jacobian does not contain any terms from the proppant advection equation,

$$\mathbf{J}^n_{m_{seq}} = \begin{bmatrix} \mathbf{K}_{dd} + \mathbf{K}_c & -\mathbf{K}_{dp} \\ \mathbf{K}_{pd} - \dfrac{1}{\Delta t}\mathbf{K}_{sd} & \mathbf{K}_{pp} \end{bmatrix}^n_m \tag{4.59}$$

The proppant degrees of freedom are then updated using an explicit finite volume method (Equation 4.37) with the converged values of fracture aperture for the time step, w^n_i. The norm of the residuals of the displacement and pressure, $\mathbf{R}^n_d$ and $\mathbf{R}^n_p$, respectively, are checked for convergence using the criteria in Equation 4.58. If the equations fail to converge, the time step is repeated using the latest proppant concentration estimates to compute the rock displacement and fluid pressure until all residuals are converged.

A loosely-coupled solution algorithm is also compared in this section, similar to the ones used in proppant transport models in the literature (e.g. Adachi *et al.* [15], Shiozawa and McClure [71], Dontsov and Peirce [75], and Shi *et al.* [83]). The loosely-coupled scheme follows the same steps as the sequential scheme, solving first for the displacement and pressure fields simultaneously and then updating the proppant concentration using Equation 4.37. The algorithm then moves to the next time step. The difference between the loosely-coupled algorithm and the sequential algorithm is that the residual norms are not checked for convergence after the proppant concentrations are updated.

4.4.2 Injection rate-controlled boundary: Global mass conservation (outer loop)

For an injection rate-controlled hydraulic fracture in an impermeable medium, the flux is prescribed at the fracture inlet and zero flux is required at the fracture tip. However, the boundary-value problem that governs fluid flow requires a Dirichlet boundary condition, *i.e.*, a prescribed fluid pressure, to obtain a unique solution to the fluid flow equation [15, 122, 123]. An additional constraint is required, called the solvability condition by Adachi *et al.* [15], to obtain a well-posed problem. The solvability condition is imposed in the form of global mass conservation along the fracture,

$$Q_{inj} = \int_{\Omega_c} \dot{w} d\Omega + \int_{\Omega_c} Q_{leak} d\Omega \tag{4.60}$$

The equation above is mass conservation of the slurry along the entire fracture, as opposed to the fluid mass conservation equation used to govern fluid flow (4.9).

Although the solvability condition has been used in various models, Gupta and Duarte [41] have recently proven that the coupled system for the hydro-mechanical problem provides a unique solution without a prescribed fluid pressure along the boundary. It is suspected that

the coupled system of equations presented in this chapter also leads to a unique solution when solved monolithically, eliminating the need for a solvability condition and thereby reducing the computation time. However, the solvability condition is still required when the problem is solved sequentially. This work is solved by imposing the solvability condition for all coupling schemes to obtain a more direct comparison.

In Khoei *et al.* [122] and Parchei Esfahani [123], global mass conservation is imposed in an external loop to the solution to iteratively determine the wellbore pressure, p_w, that is equivalent to prescribing a fluid injection rate, Q_{inj}. The algorithm corresponds to the blue-filled box in Figure 4.9. Within each iteration, k, of the outer loop, the system is solved for a given wellbore pressure estimate, p_w^k, and the resulting injection rate of the system, $\tilde{Q}^k$, is computed. The wellbore pressure estimate is then improved with each iteration until the injection rate of the system matches the desired injection rate, Q_{inj}. In Khoei *et al.* [122], a fixed-point iterative scheme is used to estimate the wellbore pressure at the fracture inlet. This method was found to lack robustness. A more robust scheme was presented in Parchei Esfahani [123], in which an iterative Newton-Raphson scheme is used to obtain the wellbore pressure corresponding to the prescribed injection rate. With each iteration, k, the wellbore pressure is estimated as

$$p_w^k = p_w^{k-1} + \lambda^{k-1} \Delta Q^{k-1} \tag{4.61}$$

The slope of the nonlinear function, $\lambda = \partial p_w / \partial \tilde{Q}$, is an unknown part of the solution and must be estimated. The error in the injection rate for iteration k is the difference between the estimated injection rate and the prescribed injection rate, $\Delta Q^k = \tilde{Q}^k - Q_{inj}$. The injection rate for the current estimate, p_w^k, is calculated as

$$\tilde{Q}^k = \frac{1}{\Delta t} \sum_e \Delta w_e \Delta s_e + \sum_e Q_{leak}^e \Delta s_e \tag{4.62}$$

in which $\Delta w_e = w_e^n - w_e^{n-1}$ is the change in fracture aperture at the center of each fluid element, e, calculated using Equation 4.32, and Δs_e is the length of the fluid element. The volumetric leak-off flux at the center of each element is denoted by Q_{leak}^e, calculated as the average leak-off flux at each of the quadrature points in the element. The iterative scheme is continued until the normalized error in injection rate is less than a specified tolerance, $\epsilon_{tol,global}$.

$$\frac{\Delta Q^k}{Q_{inj}} < \epsilon_{tol,global} \tag{4.63}$$

In the simulations included in this chapter, the global tolerance is specified as 10^{-3}.

An accurate estimate of the slope, λ, is crucial to convergence of the iterative scheme. Parchei Esfahani [123] proposed that the slope be estimated using an analytical model. While convergence

is improved for some problems, it is sometimes slow for others since it is difficult to select a suitable asymptotic solution. The addition of proppant transport equations to the model has necessitated a more robust algorithm. In Section 4.4.2, a new algorithm for estimating the slope of the wellbore pressure-injection rate curve is described which improves convergence of the global mass conservation by adaptively improving the estimate during the iterative loop.

The convergence of Newton's method is improved if the initial guess is close to the solution. Estimates of the wellbore pressure, p_w^k, and slope, λ^k, are based on analytical solutions of hydraulic fracture propagation derived from asymptotic tip conditions to increase the algorithm's efficiency. A summary of the analytical solutions is provided by [129]. For fractures in the toughness-dominated regime, solutions to the wellbore pressure are given by [130], and for those in the viscosity-dominated regime, solutions are given by [131]. The estimates described are chosen to optimize the efficiency of the global mass conservation loop for planar fracture propagation of fractures with tip conditions close to the asymptotic cases. However, the estimates are not optimized for all fractures. In cases where the fracture is further from the asymptotic tip conditions, for non-planar fractures, or for multiple fractures the global mass conservation iterative scheme may still require many iterations and perhaps small time steps to converge.

New iterative method for injection control

A new algorithm for adaptively updating the slope estimate throughout the global mass conservation loop to speed up convergence is provided for the first time in this section. Previous algorithms proposed by Khoei *et al.* [122] and Parchei Esfahani [123] are highly dependent on the initial estimates of the wellbore pressure and slope and exhibit slow convergence or lack of convergence if the initial estimates are inaccurate. The algorithm described in this section is more robust, converging even when the previous algorithms fail due to the ability to adaptively estimate the slope of the wellbore pressure/injection rate curve. It is also efficient, converging in under 10 iterations for non-planar fractures.

In each time step, the initial slope estimate based on analytical solutions is used for the first two iterations. All wellbore pressure estimates, p_w^k, and corresponding injection rates, $\tilde{Q}^k$, are stored after each iteration, as depicted by blue circles in Figure 4.10. These points are used to obtain a better approximation of λ^k for all future iterations. A linear interpolation of the previous solutions for the prescribed injection rate is used to estimate the slope. As shown in Figure 4.10, only the points closest to the prescribed injection rate are needed for the estimate. Without the adaptive estimate of the slope, the iterative method is entirely dependent on the accuracy of the initial estimate of the slope. The initial estimate may be based on analytical solutions but these are only available for limited cases.

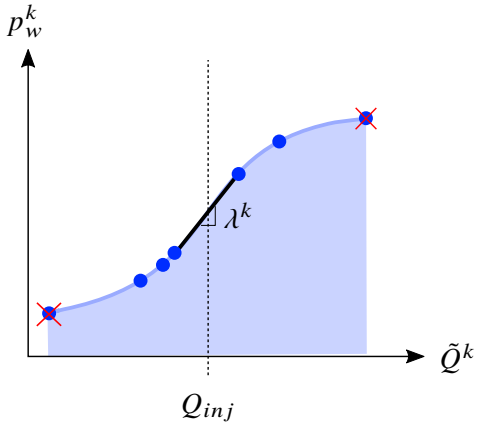

Figure 4.10: Stored data points for slope estimate

During the global mass conservation loop, it is possible that the domain is modified due to opening and closing of the fracture, essentially creating a new minimization problem. If the slope of the $p_w^k\left(\tilde{Q}^k\right)$ curve from the saved data points changes direction, it indicates that the domain has changed significantly during the iterative process and a new minimization problem must be solved. Only five data points are stored for any iteration, eliminating those furthest from the prescribed injection rate, Q_{inj}, as depicted in Figure 4.10. This number of data points is enough to determine whether the slope of the curve has changed direction, although only the two points closest to the desired solution are used in the linear interpolation. If the slope of the curve changes direction, the wellbore pressure estimate is reduced to 20% of the lowest saved estimates in the loop, and all the data points are eliminated from memory so that the wellbore pressure for the new minimization problem can be found.

Constraints are applied to the change in wellbore pressure for each iteration to further increase convergence of the iterative scheme. To avoid a negative wellbore pressure, the change in wellbore pressure is limited by setting the pressure estimate to 50% of the lowest saved estimates.

$$\text{if } \lambda^{k-1}\Delta Q^{k-1} < -p_w^{k-1} \quad \text{then} \quad p_w^k = \min_{kn \in [1,\, k-1]} \frac{1}{2} p_w^{kn} \tag{4.64}$$

Furthermore, the change in wellbore pressure is limited by a specified factor, p_{lim}, in each iteration to avoid drastically changing the solution, which may cause convergence issues in the inner solution loop.

$$\text{if } \lambda^{k-1}\Delta Q^{k-1} > p_{lim} p_w^{k-1} \quad \text{then} \quad p_w^k = p_w^{k-1}(1 + p_{lim}) \tag{4.65}$$

The limiting factor is initially set to $p_{lim} = 2$ for all simulations in this chapter. If the time step fails to converge, the factor is reduced by 20% for the following attempt.

4.4.3 Fracture propagation

A fracture is propagated through the rock domain with a cohesive-zone model [132, 133]. The cohesive zone represents the fracture process zone that is characteristic of ductile and quasi-brittle materials. It is modeled as a section of the fracture near the tip that is resisted from opening by the cohesive tractions discussed in Section 4.2.1. As such, the numerical model contains two fracture tips, one representing the tip of the fracture process zone (a fictitious crack-tip) and another representing the tip of the fully-opened fracture (the real crack-tip), as depicted in Figure 4.11a. A fracture propagation criterion extends the fracture process zone; the physical fracture propagation occurs as the fracture opens due to the fluid pressure.

The fracture process zone is propagated in the model when the maximum principal stress exceeds the yield strength of the material. The fracture is propagated to the edge of the adjacent element if the maximum principal stress at any of the quadrature points in the element ahead of the fracture tip exceeds the material yield strength, as depicted in Figure 4.11b. The direction of propagation is determined using the maximum circumferential stress criterion [134]. The hoop stress is sampled at points 2.5 element lengths ahead of the fracture in a 140-degree arc around the fracture tip. Ideally, the hoop stress is sampled as close to the crack tip as possible, but the stress state at the tip has a lower accuracy than elsewhere due to the stress concentration. The location of the sample points (2.5 elements ahead of the tip) is selected as a compromise between sampling close to the fracture tip and loss in accuracy.

When fracture propagation is detected in the algorithm, the fracture propagates to the neighboring element edge in the direction of the highest hoop stress. A common problem with arbitrary fracture propagation using the XFEM arises when a fracture intersects or gets very close to a node, leading to an ill-conditioned stiffness matrix Sukumar *et al.* [35]. To overcome this issue, if the fracture direction is headed near a node of the solid rock mesh, the fracture direction is shifted by 15 degrees. This correction does not lead to major deviation from the appropriate fracture path since it is only across a single element length.

Fracture propagation is accompanied by an addition of elements into the fluid mesh and proppant mesh. An element of the same length as the new fracture segment is added to the fluid mesh and the boundary conditions at the tip are moved to the end of the new segment. Similarly, a finite volume cell of the same length as the new fracture segment is added to the proppant mesh and the boundary conditions at the outlet are shifted to the edge of the new cell. After propagation, the time step is repeated using the new fracture length. This allows for the fracture to propagate multiple elements in a single time step.

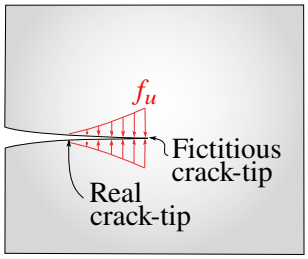

(a) Cohesive zone model

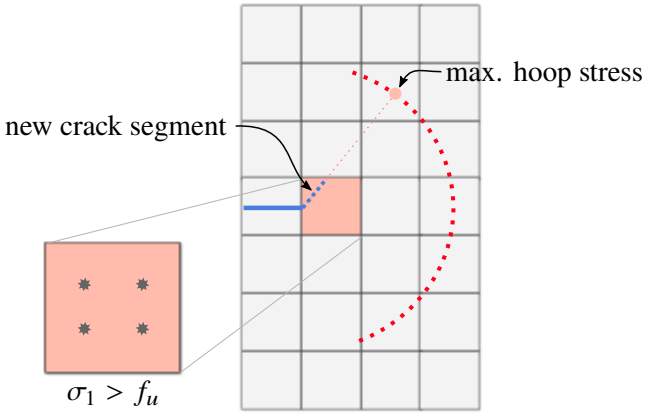

(b) Fracture propagation criterion: maximum principal stress at quadrature points in the adjacent element determines propagation and maximum hoop stress 2.5 elements away from the tip determines direction

Figure 4.11: Cohesive zone model (left) and fracture propagation criterion (right)

4.4.4 Adaptive time steps

To optimize the computational time, an adaptive time-stepping algorithm is used in this model. The largest change in the solution often occurs at the beginning of the hydraulic fracturing simulation, while the fracture is initially opening, thus requiring small time steps to converge. Once the fracture propagation begins the time step size may be increased. A reduction in the time step is also required at the onset of proppant injection and when there is a saturation of proppant concentration throughout the fracture. Since the exact time step size required is unknown to the user and varies throughout the simulation, an adaptive algorithm for setting the time step is used in this work.

Any time the maximum number of iterations is reached in the solution loop or the injection rate loop, as shown in Figure 4.9, the time step is reduced by 50%. After each iteration of the time loop, the step sizes are analyzed to determine whether a modification of the time step is required for the rest of the simulation. If the five preceding time steps have been smaller than the base time step size, the base time step for the next iterations is reduced. This reduction in time step size permits the convergence of the system of equations in parts of the simulation which undergo large changes in the solution, such as during the initial opening of the fracture or when proppant bridging occurs. The adaptive scheme also increases the base time step size when the system of equations is continuously converging to increase the efficiency of the algorithm. If the ten preceding time steps have been equal to the base time step (no reductions required), then the base time step is increased to twice the size of the current base time step. The maximum time step size

Table 4.1: Material properties for simulations of proppant transport in propagating fractures

Rock mass		
Young's modulus, E	20	GPa
Poisson's ratio, ν	0.2	
Density, ρ_s	2800	kg/m^3
Fracturing fluid		
Density, ρ_f	1000	kg/m^3
Residual aperture, w_{res}	0.1	mm
Proppant		
Density, ρ_p	2650	kg/m^3
Average radius, a	0.1	mm

is limited by the time step requirements for explicit time integration of conservation of proppant mass, Δt^n_{prop}, as defined in Equation 4.39.

4.5 Numerical results

In this section, the implementation of the numerical methodology is first verified by analyzing the proppant concentration, wellbore pressure, and wellbore aperture along a slurry-driven hydraulic fracture with a pre-defined fracture path. A study of a tip screen-out in a planar fracture is then performed for three coupling schemes: monolithic, sequential, and loose coupling. The importance of a monolithic coupling scheme is highlighted in this section, where it is shown that a sequential coupling scheme fails to converge after the onset of a tip screen-out, and a loose coupling scheme has inaccuracies due to lack of convergence. Finally, proppant transport in non-planar fracture propagation is studied and the solution of the monolithic model is compared with that of loosely-coupled and sequential models. Verification of planar fracture propagation is discussed in Appendix A, where fracture propagation in the toughness and viscosity-dominated asymptotic tip conditions are compared with analytical KGD models. The material properties that are common to all simulations in this section are provided in Table 4.1. These values are representative of a water-based fracturing fluid mixed with a 40/70 mesh sand injected into a shale reservoir.

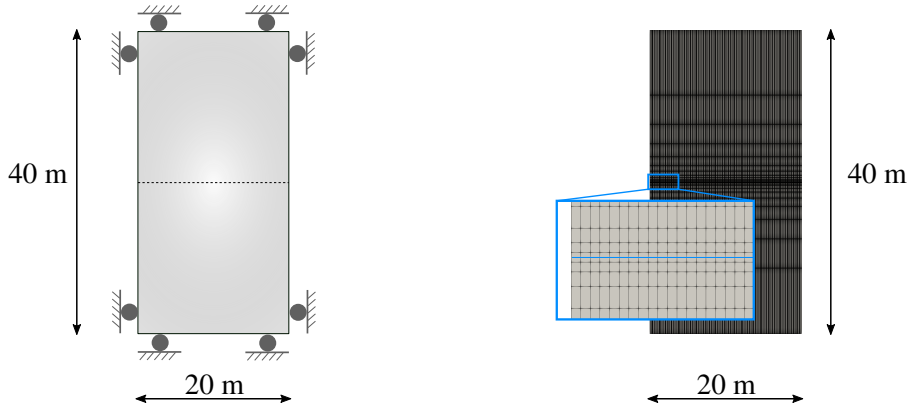

(a) Pre-defined fracture schematic (b) Numerical mesh

Figure 4.12: Schematic (left) and mesh (right) for a model of slurry flow through a pre-defined fracture

4.5.1 Slurry flow through a pre-defined fracture

In the first problem, the coupled algorithm is verified by analyzing the slurry flow through a pre-defined fracture. Neither the global mass conservation nor the fracture propagation algorithms are active in this example, to focus on the solution of the discrete system of equations (the inner solution loop in Figure 4.9).

A 20 m by 40 m domain is simulated, as depicted in Figure 4.12a, with a horizontal fracture located 20 m from the bottom of the domain that runs along the entire length of the domain. The rock mass is constrained from deforming vertically on the top and bottom edges, and horizontally on the left and right edges. There are no *in-situ* stresses applied on the domain. The rock mass has a tensile strength of 1 MPa and fracture energy of 10 J/m^2.

A structured mesh is used to discretize the solid rock domain, as depicted in Figure 4.12b. The mesh is uniformly distributed in the horizontal direction with 200 elements, and non-uniformly distributed in the vertical direction with 27 elements that are more refined near the fracture. The fluid domain is also discretized into 200 elements and the proppant domain is discretized into 200 cells.

A pad of clean fracturing fluid is injected for the first 8 seconds of the simulation into the left edge of the fracture followed by a proppant-laden slurry for 32 seconds, for a total simulation time of 40 seconds. The fracturing fluid has a viscosity of 0.001 Pa·s and is injected at a rate of 0.005 m^2/s. The proppant concentration of the injected slurry is varied and results are provided for ϕ_{inj} = 0.1, 0.3, and 0.45. The fluid is allowed to exit the domain on the right-edge by setting a zero-pressure boundary condition. The proppant is also able to exit the domain by prescribing a ghost cell on the right edge with the same proppant concentration as the adjacent cell.

The profiles of proppant concentration, fluid pressure, and fracture aperture along the length of the fracture for various time steps are provided in Figure 4.13. Results for injected proppant concentrations of 0.1, 0.3, and 0.45 are represented by red, blue, and green lines, respectively. The proppant concentration at $t = 7.5$ s is initially zero for all cases, but over time the injected proppant passes from the left edge to the right edge of the fracture until the entire fracture has the same concentration at $t = 30$ s. The proppant is transported through the fracture with a sharp proppant front. The lack of numerical diffusion in the model is made possible by the applied flux limiters, as discussed in 3.3.4. Slurries of higher proppant concentration move slower through the fracture, demonstrated in Figure 4.13g by the proppant front for the injected slurry of 0.45 proppant concentration lagging behind the other cases. A greater proppant concentration leads to a higher effective slurry viscosity, and therefore a slower transport speed.

At $t = 7.5$ s, the fluid has filled the fracture, resulting in a pressure profile starting at 0.815 MPa at the inlet and reducing to zero at the outlet. As the proppant is injected, the effective viscosity of the slurry is increased leading to an elevated fluid pressure inside the fracture. The pressure increase follows the proppant front from the left edge to the right edge of the domain over time. The final pressure profile at $t = 30$ s for the slurry-filled fracture is higher than that of the pure fluid-filled fracture at $t = 7.5$ s. A higher proppant concentration results in a greater pressure increase, demonstrated in Figure 4.13k, in which the fracture injected with a slurry of 0.45 proppant concentration has a higher pressure profile than those injected with slurries of lower proppant concentration. Higher fluid pressures also result in larger fracture apertures as the fluid causes the fracture to push open, shown in Figure 4.13l. In summary, an injected slurry with higher proppant concentration moves slower through the fracture, but leads to a higher pressure build-up and consequently a wider fracture than slurries of lower proppant concentration. The response of the fluid pressure and fracture aperture to the proppant flow is as expected.

4.5.2 Comparison of coupling schemes during tip screen-out

In this section, slurry flow through a fracture and the onset of a tip screen-out are compared for three different coupling schemes: monolithic, sequential, and loose coupling. The same mesh, boundary conditions, and material properties as the previous example are used. Differing from the previous example, leak-off of the fracturing fluid into the domain is included with a Carter leak-off coefficient of 1×10^{-4} m/$\sqrt{\text{s}}$. Fracturing fluid is first injected into the domain for 4 seconds, followed by a slurry with proppant concentration of 0.1 m^3/m^3 for 6 seconds, for a total simulated time of 10 seconds. The results of the monolithic model presented in this chapter are compared with a sequentially-coupled scheme and a loosely-coupled scheme. The difference in the three schemes lies in the algorithm for the solution loop, as described in Section 4.4.1.

The profiles of proppant concentration, fluid pressure, and fracture aperture along the length of the fracture for various time steps are provided in Figure 4.14. Results for the monolithic, sequential,

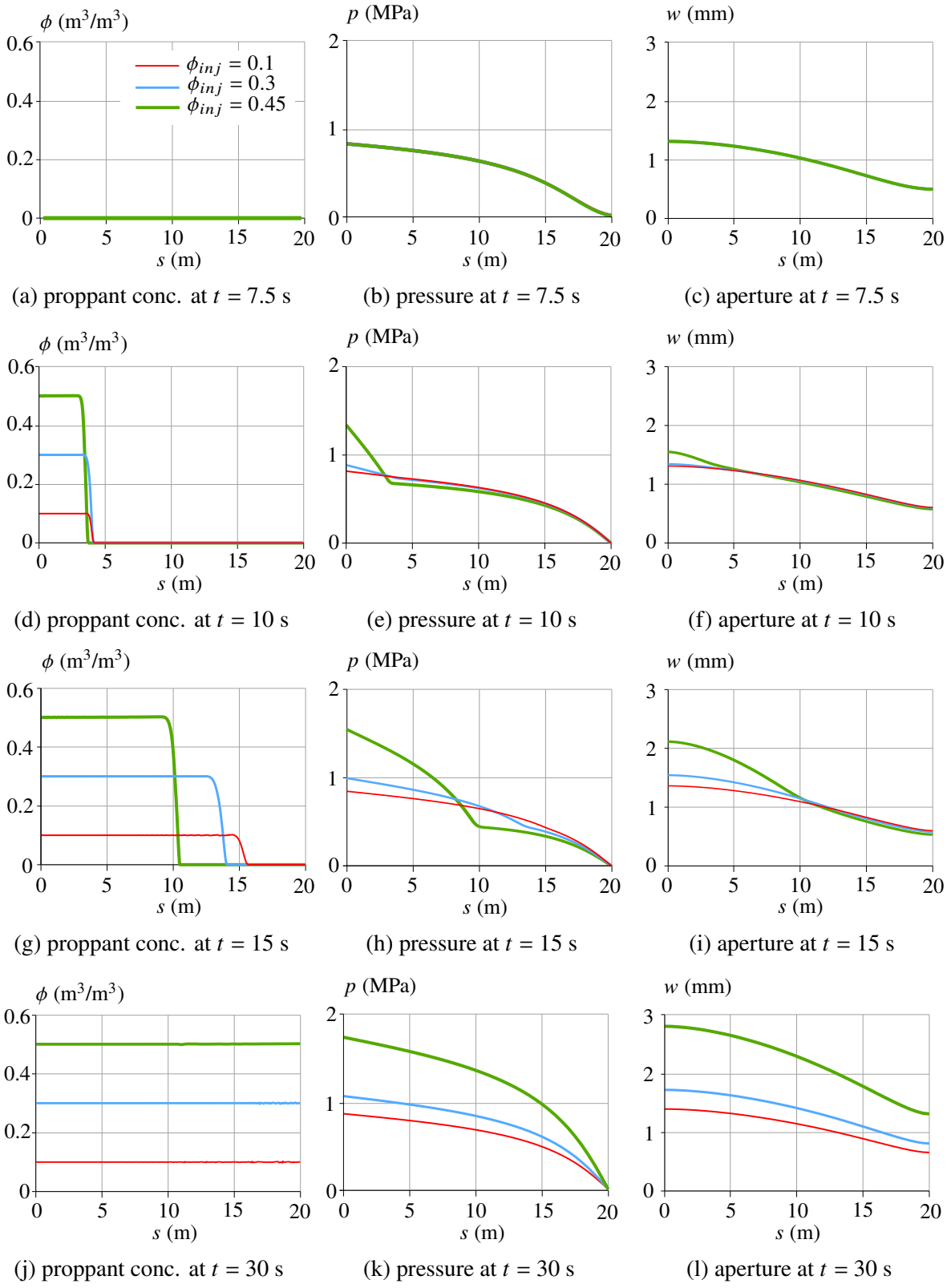

(a) proppant conc. at t = 7.5 s (b) pressure at t = 7.5 s (c) aperture at t = 7.5 s

(d) proppant conc. at t = 10 s (e) pressure at t = 10 s (f) aperture at t = 10 s

(g) proppant conc. at t = 15 s (h) pressure at t = 15 s (i) aperture at t = 15 s

(j) proppant conc. at t = 30 s (k) pressure at t = 30 s (l) aperture at t = 30 s

Figure 4.13: Proppant concentration, fluid pressure, and fracture aperture for a planar, slurry-driven fracture over time. Results are plotted for various injected proppant concentrations: ϕ_{inj} = 0.1 (red), ϕ_{inj} = 0.3 (blue), and ϕ_{inj} = 0.45 (green)

and loose solution algorithms with explicit time integration are shown. Though the schemes yield different solutions, each is converged and unchanging with refinement. A proppant-laden slurry is injected starting at $t = 4$ s with a volumetric proppant concentration of 0.1 m^3/m^3 and travels from the left- to right- edge of the domain over time. During the treatment, the proppant front reaches a point along the fracture at which the aperture is too narrow for the particles to pass and bridging occurs (at 6 mm or three proppant diameters). The proppant concentration builds up until it reaches a saturation value of 0.6 m^3/m^3. After bridging occurs, the proppant is no longer able to travel through the fracture and fluid flow is greatly reduced. A large pressure gradient is formed at the location of proppant bridging and the physical fracture tip ceases to propagate. This behavior is commonly known as a tip screen-out, which leads to the creation of wide, short fractures. The location along the fracture at which proppant bridging occurs is dependent both on the average proppant diameter and the choice in threshold aperture of the bridging function. The selection of material parameters and injection parameters used in this example leads to the on-set of proppant bridging within 10 seconds of the start of injection. Bridging occurs fairly quickly in this example due to the combination of high injection rate and high leak-off coefficient, though in practice the onset of a tip screen-out may occur within minutes or hours of proppant injection.

The results of the monolithic and sequential coupling algorithms are identical up to the point of bridging, reflected by the curves for these two models lying right on top of one another in Figure 4.14. After bridging occurs the solution loop for the sequential scheme fails to converge. The results of the loosely-coupled algorithm are the same as those of the monolithic and sequential algorithms before proppant injection begins at 4 s. Once proppant injection begins the solutions diverge and the accumulation of error in the loosely-coupled scheme is pronounced once proppant bridging occurs. The loosely-coupled algorithm predicts the onset of tip screen-out earlier along the fracture than the sequential and monolithic schemes (around 8.5 m compared to 10 m).

In Figure 4.15, the proppant concentration over time is shown for the loose coupling scheme solved with both explicit and quasi-implicit time integration, henceforth denoted as loose-explicit and loose-implicit, respectively. The results are shown for a time step size of 8ms after the start of proppant injection. Spurious oscillations at the proppant front are observed for the loose-explicit scheme, a behavior not exhibited in the loose-implicit algorithm for the same time step size. The spurious oscillations are eliminated with refinement in time, thereby showing that a smaller time step size is required for the loose-explicit scheme than the other coupling schemes. For this problem, the monolithic, sequential, and loose-implicit algorithms show converged results for time step sizes at their CFL limit of around 15 ms, whereas the loose-explicit scheme exhibits oscillations in the results for time step sizes greater than 5 ms.

Despite the elimination of spurious oscillation behavior at the proppant front, the loose-implicit scheme converges to the same results as the loose-explicit scheme. An increase in accuracy is not obtained with a different time integration method for a loose coupling scheme. This result may be attributed to the fact that the loose schemes do not ensure that the residuals are reduced to zero within each time step.

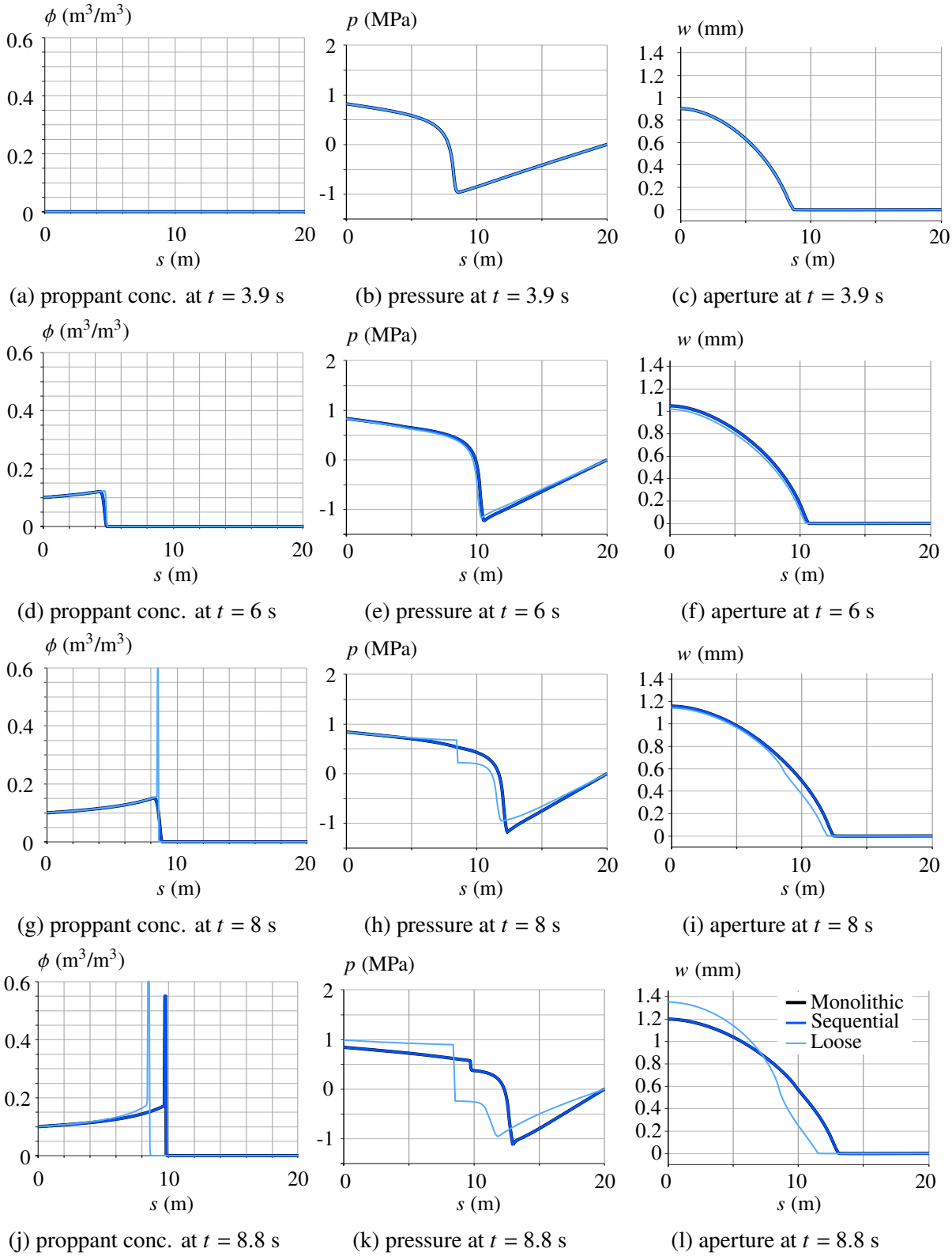

(a) proppant conc. at t = 3.9 s (b) pressure at t = 3.9 s (c) aperture at t = 3.9 s

(d) proppant conc. at t = 6 s (e) pressure at t = 6 s (f) aperture at t = 6 s

(g) proppant conc. at t = 8 s (h) pressure at t = 8 s (i) aperture at t = 8 s

(j) proppant conc. at t = 8.8 s (k) pressure at t = 8.8 s (l) aperture at t = 8.8 s

Figure 4.14: Proppant concentration, fluid pressure, and fracture aperture for a planar, slurry-driven fracture undergoing a tip screen-out at various times. Results are plotted for various coupling schemes: monolithic (black), sequential (dark blue), and loose (light blue)

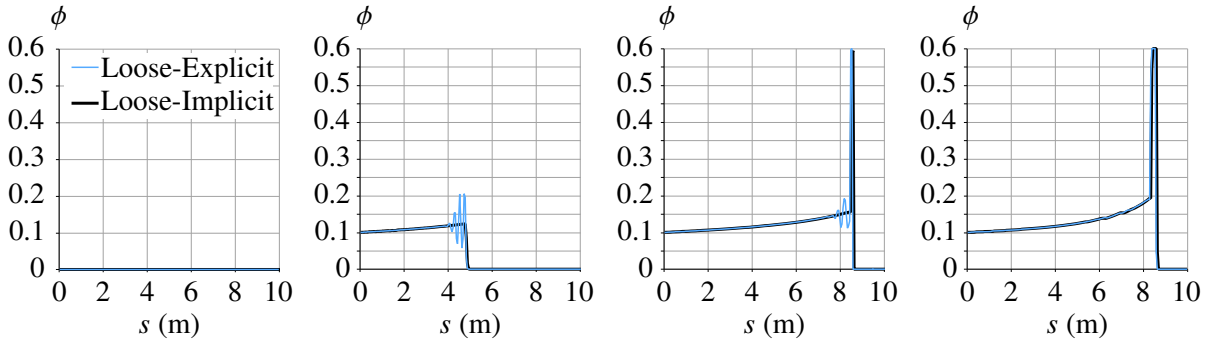

(a) proppant concentration at $t = 3.9$ s

(b) proppant concentration at $t = 6$ s

(c) proppant concentration at $t = 8$ s

(d) proppant concentration at $t = 10$ s

Figure 4.15: Proppant concentration along half of the fracture length over time for the loose coupling scheme. Results are plotted for explicit time integration (blue) and implicit time integration (black)

4.5.3 Non-planar fracture propagation

The propagation of a non-planar fracture is simulated in this section with two examples. In the first example, the propagation of five fractures with varying initial direction is verified. In the second example, a proppant-laden slurry is injected into a non-planar fracture and the results of the monolithic model presented in this chapter are compared with those obtained with a loosely-coupled model. The results of the sequential model are omitted since they are identical to the monolithic model up to the onset of tip screen-out.

A wellbore of 12.7 cm diameter centered in a 20 m by 20 m domain is simulated, as depicted in Figure 4.16a. The domain has minimum and maximum *in-situ* horizontal stresses of 10 MPa and 30 MPa, respectively. Fluid is injected into the wellbore at a rate of 3.5×10^{-4} m^2/s. The outer boundary of the solid domain is restrained from moving in the normal direction. A traction due to the pressure of the injected fluid is applied normal to the wellbore. The rock has a yield strength of 1 MPa and fracture energy of 100 J/m^2. The fracturing fluid has a viscosity of 1 Pa·s and a Carter leak-off coefficient of 1×10^{-4} m/$\sqrt{\text{s}}$.

A mesh of 7,643 quadrilateral elements, depicted in Figure 4.16b, discretizes the solid rock domain. A structured mesh is used near the wellbore which circles a 1 cm radius around the wellbore and extends into the first quadrant a distance of 1.5 m from the center of the wellbore in a 100° arc from the vertical direction. The average element length varies from 2 mm at the wellbore, 4 cm at a distance of 1.5 m from the center of the wellbore, to 3 m at the outer boundary of the domain.

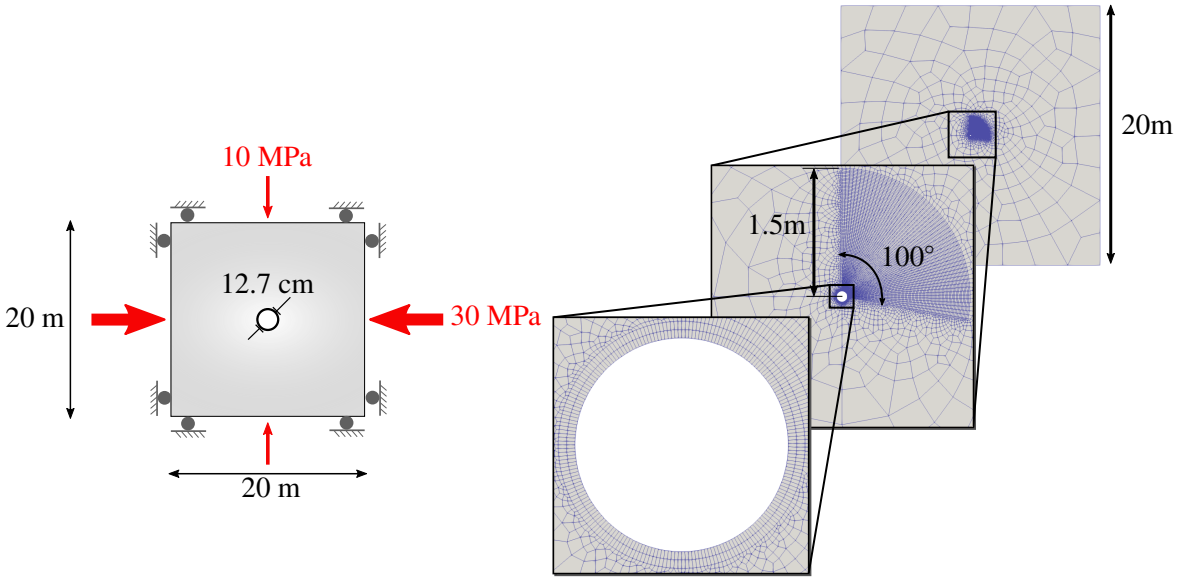

(a) Wellbore schematic (the wellbore is not drawn to scale for clarity)

(b) Numerical mesh

Figure 4.16: Schematic (left) and mesh (right) used to simulate slurry-driven non-planar fracture propagation from a wellbore

Verification of non-planar fracture propagation

In this example, a hydraulic fracture driven by fracturing fluid without proppant is simulated for verification. Pure fracturing fluid is injected into an initial fracture of 2 cm length located along the wellbore at an angle, θ, from the horizontal. The simulation is repeated for fractures of varying initial orientations with $\theta = 0°$, $20°$, $40°$, $60°$, and $80°$. A similar study has been performed in the framework of Linear Elastic Fracture Mechanics (LEFM) by Mogilevskaya *et al.* [135] and Zhang *et al.* [136]. The fracturing fluid is injected into the wellbore for 5 seconds, resulting in the fracture propagation depicted in Figure 4.17. In 5 seconds, the fractures propagate about 24 times the wellbore radius, R_w. The fractures are expected to rotate to propagate in the direction of the maximum principal stress. The propagation direction near the wellbore is affected by the local stresses due to the stress concentration caused by the wellbore and the fluid pressure acting on the wellbore. Away from the wellbore, the simulated fractures propagate in the horizontal direction, as expected.

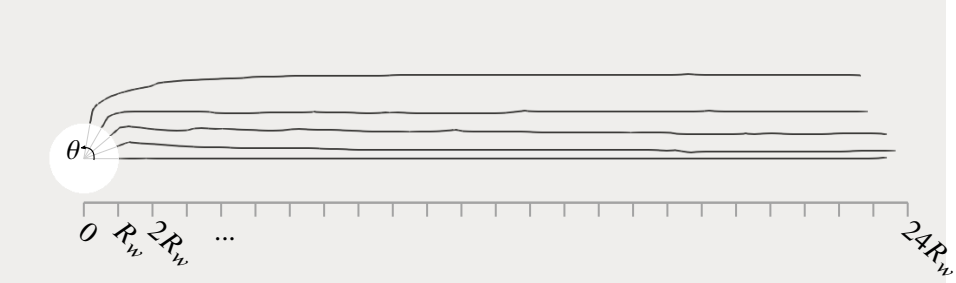

Figure 4.17: Fracture propagation resulting from an initial fracture of 2 cm length oriented at varying angles, θ, of 0°, 20°, 40°, 60°, and 80° from the horizontal

The wellbore aperture, w_0, wellbore pressure, p_w, and fracture length, L, over the simulated time are plotted in Figure 4.18. As expected, the fracture that is initially oriented perpendicular to the minimum principal stress ($\theta = 0°$) has the largest wellbore aperture during the simulation. The aperture at the wellbore is reduced the further the initial fracture alignment is from the horizontal direction, as shown in Figure 4.18a. The breakdown pressure, shown in Figure 4.18b, decreases as the initial fracture orientation moves closer to the horizontal axis because the *in-situ* stress acting normal to the fracture surface is reduced. The fracture lengths are not strongly affected by the orientation of the initial fracture segment, as shown in Figure 4.18c.

When oriented in the direction perpendicular to the minimum principal stress, the fracture undergoes purely Mode I (tensile) propagation. As the fracture orientation deviates from the horizontal direction there is an increase in shear stresses which causes mixed-mode propagation. The result is a smaller aperture along the initial fracture segment due to Mode II (in-plane shearing) behavior. The mixed-mode propagation behavior of the XFEM model has been validated against an experiment by Gee *et al.* [137], in which a PMMA specimen with an initial fracture emanating from a circular hole is compressed to induce mixed-mode fracture propagation. The results from this experiment show a dominant shearing behavior (Mode II) along the initial fracture segment and tensile opening (Mode I) in the remainder of the propagated fracture.

Based on these results, proppant with a diameter of 2 mm is not able to enter any fracture with a wellbore aperture smaller than 6 mm due to proppant bridging. Thus, it is only able to enter the fractures oriented at $\theta = 0°$ and 20° in this example. In a field application, there are many natural fractures oriented in all directions around a wellbore. The results from this study suggest that proppant particles are more likely to enter fractures that are initially oriented perpendicular to the minimum principal stress since their stimulated apertures are larger and less likely to obstruct slurry flow at the inlet than fractures oriented in other directions.

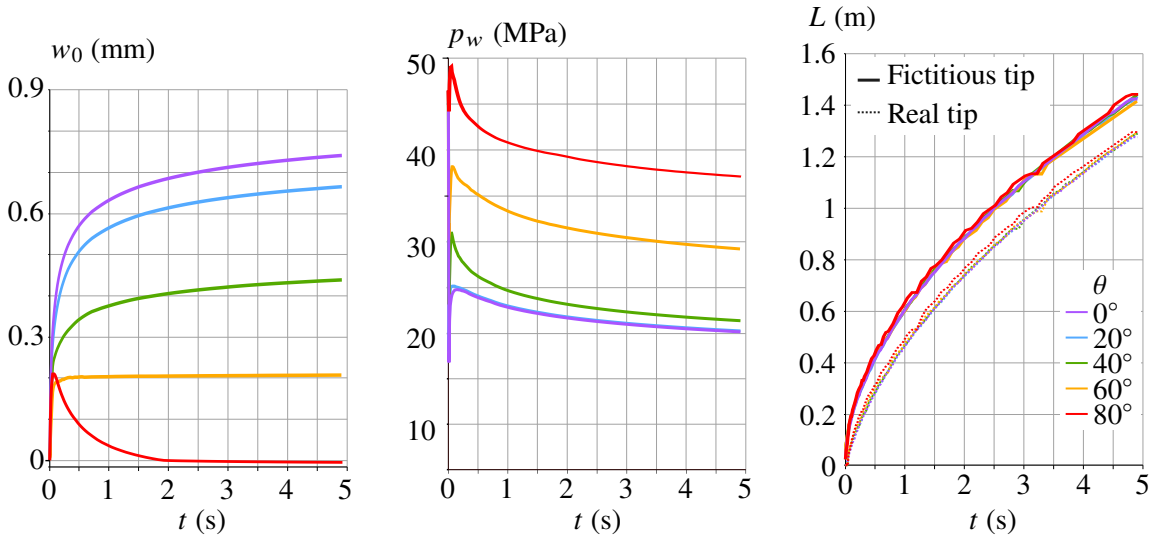

(a) Wellbore aperture over time (b) Wellbore pressure over time (c) Fracture length over time

Figure 4.18: Wellbore aperture, wellbore pressure, and fracture length over time for fractures initially oriented at 0°, 20°, 40°, 60°, and 80° from the horizontal

Slurry flow through non-planar fracture

In this example, a proppant-laden slurry is injected into a fracture oriented 20° from the horizontal using the same mesh and material properties as the previous example. At this initial orientation, there is enough tensile opening of the fracture at the wellbore to allow for proppant injection. Pure fracturing fluid is injected for the first 1.75 seconds of the simulation, followed by a slurry injected with a volumetric proppant concentration of 0.1 for a total simulated time of 7 seconds. A constant injection rate of 3.5×10^{-4} m^2/s is maintained throughout the simulation.

The proppant concentration, fracture aperture, and fluid pressure over the length of the fracture are shown in Figure 4.19 for various times throughout the simulation. The proppant concentration is zero until $t = 1.75$ s when the slurry injection begins. The fracture is injected at a concentration of 0.1 from the inlet and travels through the fracture over time. Due to shearing of the initial fracture segment, the first 2 cm of fracture has a smaller aperture than the rest of the fracture. As time progresses, the fracture propagates and the aperture along the entire fracture increases. The fluid pressure is highest at the inlet and tapers down at the fracture tip, which is characteristic of viscosity-dominated fracture propagation.

When the proppant front reaches roughly 0.9 m into the fracture, proppant bridging occurs since the fracture aperture is three proppant diameters (0.6 mm) wide at this point. The proppant concentration builds up until it reaches the saturation concentration of 0.6 m^3/m^3. A tip screen-out occurs after the proppant concentration becomes saturated.

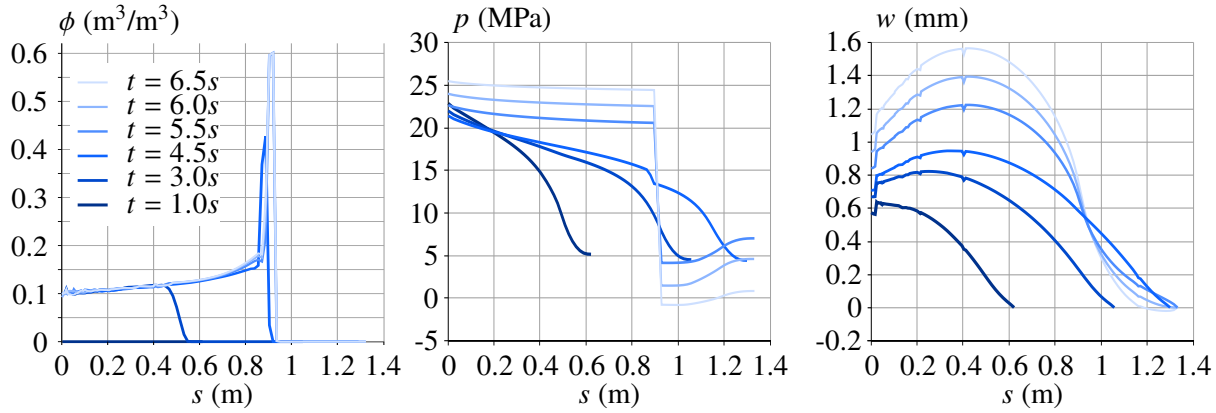

(a) Proppant concentration over the length of the fracture

(b) Fluid pressure over the length of the fracture

(c) Fracture aperture over the length of the fracture

Figure 4.19: Proppant concentration, fluid pressure, and fracture aperture for a non-planar slurry-driven fracture over time

After the onset of the tip screen-out, the pressure profile along the fracture changes drastically (see Figure 4.19b). A jump in the fluid pressure is formed at the proppant front. The pressure upstream of the front increases since the fluid flow through the packed proppant is greatly impeded. The pressure downstream of the front diminishes since the leak-off at the tip exceeds the fluid flowing through the packed proppant. A de-watering of the fracture tip occurs after the screen-out, manifested by an increase in pressure from the proppant front towards the fracture tip. This shows that after the tip screen-out, the fracturing fluid flows from the fracture tip towards the proppant front. This de-watering behavior may be due to the lack of interaction of the fracturing fluid with the reservoir fluid assumed in this model.

Figure 4.19c also shows that the fracture aperture increases upstream of the proppant front after the onset of bridging, creating a fat fracture that does not continue to propagate. Due to the de-watering upstream of the proppant bridge, the fracture aperture also begins to close ahead of the bridge in this model.

The maximum proppant concentration along the fracture and the location of the proppant front over time are shown in Figures 4.20a and 4.20b for both the fully-coupled and loosely-coupled models. The oscillations in Figure 4.20a between $t = 4$ s and $t = 5$ s in the fully-coupled model show that as the proppant is building up there is a cyclical pattern of increasing proppant concentration followed by a subsequent reduction. The proppant concentration builds-up and causes the fracture aperture to increase enough for the proppant front to move forward and subsequently flush through the bridging point. The proppant front reaches another section of narrow aperture and builds up again until the fracture opens enough for it to flush through that bridge and move forward again. Ultimately, the proppant front stops moving and tip screen-out

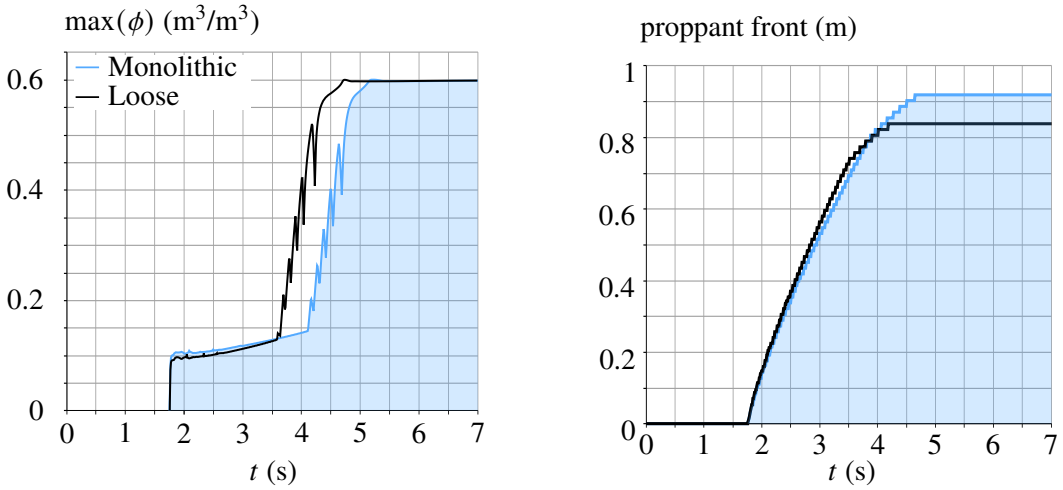

(a) Maximum proppant concentration along the length of the fracture over time

(b) Location of the proppant front along the length of the fracture over time

Figure 4.20: Maximum proppant concentration (left) and proppant front location (right) over time

occurs when the proppant concentration becomes saturated, as shown in Figure 4.20.

In the monolithic coupled model, the proppant front stops moving approximately 4.6 s after the start of the simulation. The loosely-coupled model fails to converge to the same solution as the monolithic model. The results obtained with the loosely-coupled scheme predict that proppant bridging and subsequent tip-screen out occur approximately 0.5 s before the fully-coupled model. A tenfold reduction in time step size was not able to meaningfully change the solution of the loosely-coupled model. This suggests that the loosely coupled model accumulates error in time that cannot be reduced through the use of smaller time steps. This result is expected given that no iterative process is used to ensure that the solution is converged within each time step.

The wellbore aperture, wellbore pressure, and fracture length over time are plotted in Figure 4.21 for the fully-coupled model in blue, loosely-coupled model in black, and the model with no proppant injection in gray. The results of all three models are the same for the first 1.75 s of the simulation before the proppant injection begins. After proppant injection begins, the wellbore aperture and pressure are higher and the fracture length is shorter for the models with proppant. A steeper increase in wellbore pressure and wellbore aperture occurs after the tip screen-out begins. The propagation of the fracture tip ceases since the fluid flow past the proppant pack is impeded. The results of the loosely-coupled model confirm that it is not able to accurately capture proppant transport, resulting in a predicted fracture with a wider aperture and shorter length. The sequentially coupled scheme yields results comparable to those of the monolithically coupled scheme, up to the point of tip screen out, after which the sequential scheme fails to converge

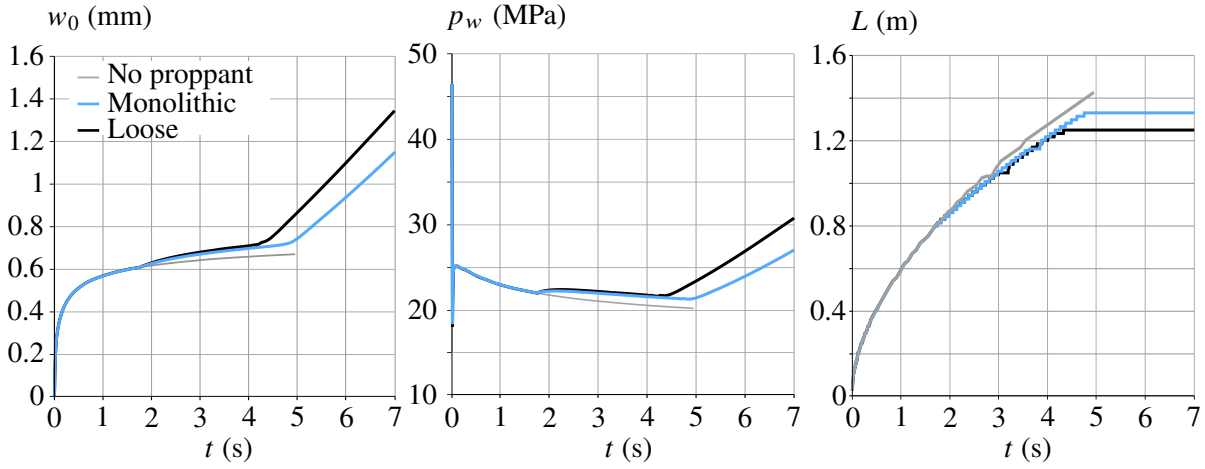

(a) Wellbore aperture over time (b) Wellbore pressure over time (c) Fracture length over time

Figure 4.21: Wellbore aperture, wellbore pressure, and fracture length over time for a fracture initially oriented 20° from the horizontal. Results of the fully-coupled model (blue), loosely-coupled model (black) and model with no proppant injection (gray) are provided.

whereas the monolithic scheme does converge.

The simulation of slurry flow through the non-planar fracture requires approximately 7 hours of CPU time. The main computational bottleneck is the small time step required to meet the CFL stability condition. The time step size over the simulated time is plotted in Figure 4.22. At the start of proppant injection at $t = 1.75$ s the time step size is greatly reduced to accommodate the time step requirements of the CFL condition. The critical time step is a function of the fracture aperture and pressure gradient, meaning that smaller time steps are required as the fracture gets wider and the pressure gradient increases. This leads to longer CPU times, particularly after a tip screen-out occurs. The loose coupling scheme requires a time step smaller than the one strictly required by the CFL condition to converge. The adaptive time stepping described in Section 4.4.4 reduces the time step size until convergence is met. This explains why the time steps used in the monolithic and loose coupling schemes differ.

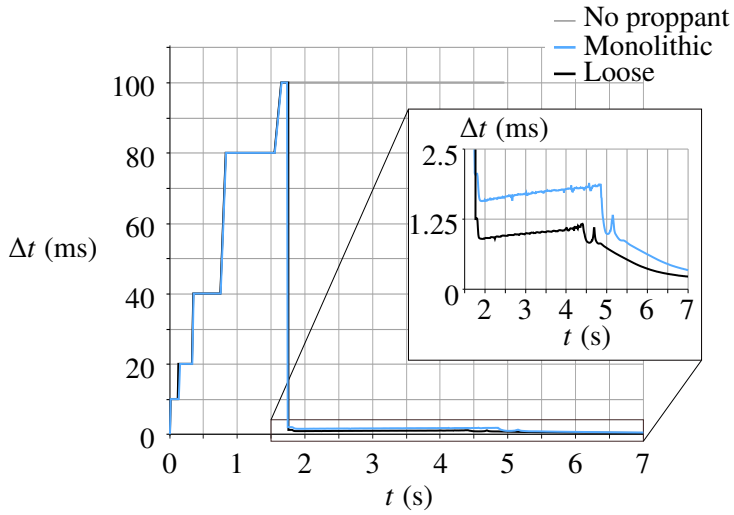

Figure 4.22: Time step size over simulation time

4.6 Discussion

The choice of an optimal solution scheme should consider a) computational efficiency; b) accuracy; and c) robustness. Computational efficiency is often cited as the motivation/justification for loosely coupled over monolithic schemes; however, a close study of the costs of the algorithms suggests that loosely coupled schemes have comparable computational costs to a monolithic scheme. In contrast, sequential schemes are more computationally expensive. This can be illustrated by studying the number of times the Jacobian used in the calculation of the displacements and fluid pressure is assembled and inverted, which is performed multiple times in each time step. This is the most costly part of the algorithm and therefore a good proxy for the total computational cost of the schemes. While the size of the Jacobian is slightly larger for the monolithic scheme, it is similar enough to that of the other schemes to have a negligible effect for the comparison. For the numerical example performed in Section 4.5.2, Figure 4.23 illustrates the number of Jacobian calculations for each scheme. It is clear after the start of proppant injection ($t > 4$ s), the monolithic scheme is just as efficient as the loosely coupled scheme and that the monolithic scheme is much more efficient than the sequential scheme.

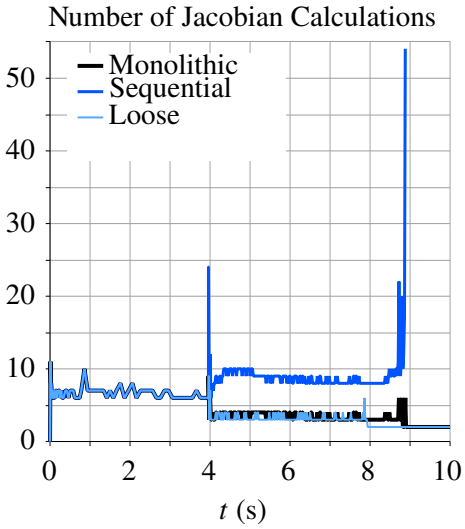

Figure 4.23: Number of Jacobian calculations

The results in Section 4.5.2 call into question the accuracy of solutions obtained using the loosely coupled schemes. It has been shown that the loosely coupled schemes (implicit or explicit) fail to converge to the same solution as the sequential or monolithic schemes, even with time step refinement. This seems a natural outcome of the one-pass update of the proppant concentration. Therefore, while the loosely coupled schemes are modular and easier to incorporate into existing codes, the justification for such approaches is questionable.

In terms of the robustness of the schemes, it has been demonstrated that the solution loop for the sequential scheme fails to converge once proppant packing begins. The loosely coupled scheme conveniently avoids this issue by the nature of its one-pass algorithm in which convergence is not verified. It has often been reported in the literature in the context of examples showing screen-outs that loosely coupled schemes can easily be made more accurate by the introduction of iteration; however, the results presented here suggest that the iterations may not converge.

Thus, the optimal scheme in terms of computational cost, accuracy, and robustness is the monolithic scheme. The sequential scheme can be used with confidence (but with increased cost), so long as the solution loop converges. The loosely coupled schemes should generally be avoided since they yield different solutions than would be obtained with sequential or monolithic schemes and have a computational cost similar to the monolithic scheme. In this work, the XFEM is used to solve for the deformation of the fractured rock mass, but the monolithic scheme is also expected to be the optimal coupling strategy for models that use other numerical methods, such as boundary element methods and standard finite element methods.

Chapter 5

Conclusions

5.1 Concluding remarks

The production of a reservoir is optimized in a hydraulic fracturing treatment by fracture growth, proppant distribution throughout the fracture, and shear dilation in the surrounding fracture network. The three main objectives in this thesis support the simulation of the mechanisms which enhance reservoir productivity. Methods to solve the complex nonlinear and non-smooth system of equations that governs the hydraulic fracturing process were discussed.

The first objective was to develop a numerical model for the simulation of the mechanical deformation and shear dilation of naturally fractured rock masses using the extended finite element method. A model was created to simulate the nonlinear behavior of a Discrete Fracture Network, including contact, cohesion, friction and shear dilation. Coulomb friction was considered on fracture surfaces that are in contact. Shear dilation was incorporated in the model using a linear dilation model, capped by a dilation limiting displacement, which takes into account the average effect of asperities along the interface. An explicit time-integration scheme, with scaled damping and mass matrices through a Dynamic Relaxation algorithm, was employed to solve the semi-discrete equations.

To demonstrate the validity of the contact-dilation constitutive models, multiple direct shear tests were simulated. The results of the simulation show that the shear strength of the specimen is directly proportional to the applied normal stress, and conversely, the average dilation along the interface is inversely proportional to the normal stress applied to the specimen. Under direct shearing, it was also observed that when the normal stress exceeds the unconfined compressional strength of the rock specimen, asperities undergo local shearing and no dilation is seen along the interface.

Simulations of a biaxial test of a DFN verify the proportionality of shear displacement and dilation along fracture sets. The tests also show the convergence of the model with mesh refinement, even

for multiple fractures. Finally, the stability of a DFN rock slope under its gravitational force and a monotonically increasing external compressive load was investigated. Simulations demonstrate the stability of the slope under gravitational forces and subsequent failure of the slope after a critical increase in the external force. The slope becomes unstable through the sliding of a critical fracture located beneath the external force.

The second objective was to develop a numerical model for the simulation of proppant transport through planar fractures. The numerical methodology for solving the nonlinear hyperbolic partial differential equation that describes proppant transport through a hydraulic fracture was presented in this thesis. In many of the hydraulic fracturing models to date, the advection equation is linearized by assuming a constant fluid velocity. The work presented focuses solely on the solution of the proppant transport equation, without assuming a linear form for the proppant flux function. Instead, a nonlinear advection problem was solved in which a constant pressure gradient was assumed rather than a constant flow velocity.

The finite volume method using the Godunov approximation with an entropy fix and a high-resolution correction using slope limiters was used. This methodology is capable of capturing the shock waves in the solution which arise from the spatially-varying fracture width and fluid pressure gradient along the fracture (especially at the fracture tips and inlet), as well as the rarefaction wave that emerges when a proppant build-up disperses into a fracture. A predictor-corrector algorithm was proposed for constraining the concentration within physically allowable limits. Additionally, proppant bridging was simulated by limiting the proppant flux for fracture widths less than a threshold size. A critical time step was derived for proppant transport problems which works for any effective viscosity function used to describe the slurry.

The numerical method was verified by evaluating the rarefaction wave that occurs as proppant is injected at high concentrations into a fracture and the compression wave that occurs as when a proppant plug is formed at a small fracture width. Proppant advection through an elliptical fracture was investigated, in which proppant bridging was observed at the location where the fracture width is too narrow for proppant to pass. Finally, proppant transport through a plane-strain KGD fracture was investigated which shows that a narrow fracture width may cause a plug along the fracture before proppant reaches the tip. Solutions were compared using various functions for effective slurry viscosity and it was observed that the Krieger-Dougherty expression with $\beta = 1$ results in the fastest moving proppant, while $\beta = 3$ results in the slowest moving proppant. The other viscosity functions produce results that lie between those extremes.

The results obtained in this work further the understanding of the nonlinear advection of proppant through a fracture. It is of particular importance in grasping the limitations of mixture models where linear proppant advection is performed as a separate step after coupling the rock deformation and slurry flow. The model presented provides a numerical foundation for simulating the complexities of nonlinear proppant transport.

The final objective of the thesis was to develop a numerical model for the simulation of proppant

transport through propagating non-planar fractures. The first monolithic model for the simulation of hydraulic fracturing incorporating the mechanisms of rock deformation, fluid flow, and proppant transport was presented. The model was used to simulate a tip screen-out, in which a high degree of physical coupling is present. Simulations were performed for both planar and non-planar fracture propagation and the results of the monolithic scheme were compared with sequential and loose coupling algorithms.

All hydraulic fracturing models in the current literature that consider proppant transport solve for the rock deformation and slurry pressure first, followed by a loosely-coupled update of the proppant concentration at the end of a time step. In this work, it was demonstrated that a loosely-coupled model converges to different solutions than monolithic and sequential coupling schemes, even with refinement in time step size. The computational cost of the monolithic scheme was shown to be comparable to that of a loose coupling strategy and more efficient than the sequential algorithm. Finally, the sequential scheme was shown to lack robustness at the onset of a tip screen-out where the solution loop fails to converge. Through this comparison, it is clear that the monolithic scheme is the optimal scheme in terms of computational cost, accuracy, and robustness. In addition to this finding, a new algorithm was described for optimizing the iterative scheme used in simulating injection rate controlled hydraulic fracturing via global mass conservation.

Simulation of hydraulic fracturing is a challenging problem due to the complex coupled physics involved. There is no fracture model currently available that rigorously incorporates all of the mechanisms which lead to enhanced reservoir production due to a hydraulic fracturing treatment. Hence, questions remain unanswered such as: what is the geometry of the fracture network? how much permeability enhancement will a treatment provide? and what are the stimulated reservoir volume and the effective propped volume? A numerical model that can simulate fracture growth, proppant transport, and shear dilation would be a valuable tool for petroleum engineers in making operational decisions. The work presented in this thesis supports the creation of such a model by addressing the numerical challenges posed by the highly nonlinear coupled mechanisms that take place in hydraulic fracturing treatments. The shear dilation model presented tackles the challenge of non-smooth interface constitutive laws to lay the groundwork for quantifying the stimulated reservoir volume. The proppant model presented addresses the nonlinear transport and forms a foundation for understanding the effective propped volume of a treatment. Finally, the work done to couple hydraulic fracturing models with proppant transport provides a way to simulate how the proppant affects fracture growth during a tip screen-out.

5.2 Significant contributions

In the process of accomplishing the objectives of this thesis, research contributions that expand the knowledge currently available in the literature were produced. The significant contributions

are disseminated in peer-reviewed journals and summarized below.

The first objective of the thesis is to develop a numerical model for the simulation of the mechanical deformation and shear dilation of a naturally fractured rock mass. This work is disseminated in

Rivas, E. *et al.*, A two-dimensional extended finite element method model of discrete fracture networks, *International Journal for Numerical Methods in Engineering*, vol. 117, no. 13, pp. 1263–1282, 2019

Rivas, E. and Gracie, R., Shear Dilation Using the Extended Finite Element Method, en, in *24th International Congress of Theoretical and Applied Mechanics*, Montreal, Canada, 2016

Rivas, E. and Gracie, R., An Extended Finite Element Model for Studying Shear Dilation in a Pressurized Medium, in *14th U.S. National Congress on Computational Mechanics*, Montreal, Canada, 2017

The key contributions of this work are summarized below:

- This work investigates the failure of fractured rock masses under compressive regimes in which Mode II fracture, shear dilation, and frictional contact are all simultaneously active.
- The mechanics of shear dilation is simulated for the first time with the extended finite element method (XFEM).
- The simulation of a discrete fracture network (DFN) in this study differs from the current XFEM literature, which has primarily focused on the simulation of single fracture problems.

The second objective of the thesis is to develop a numerical model for the simulation of slurry flow through a planar fracture. This work is disseminated in

Rivas, E. and Gracie, R., Numerical considerations for the simulation of proppant transport through fractures, *Journal of Petroleum Science and Engineering*, 2019

The key contributions of this work are summarized below:

- Solution of the nonlinear heterogeneous hyperbolic advection equation that governs proppant transport is studied in this work. This study differs from current hydraulic fracture models in the literature, which have mainly focused on solving linearized forms of the advection equation.
- A predictor-corrector algorithm for constraining proppant concentrations within the physically admissible range is presented for the first time in this work.
- A critical time step suitable for all proppant problems independently of the proppant concentration is derived.

The third objective of the thesis is to develop a numerical model for the simulation of slurry flow through a propagating non-planar fracture. This work is disseminated in

Rivas, E. and Gracie, R., A monolithic coupled hydraulic fracture model with proppant transport, *Manuscript submitted for publication*, 2020

The key contributions of this work are summarized below:

- A hydraulic fracture model in which proppant transport is monolithically coupled is presented for the first time to address the gap in loose coupling methods where convergence is not soundly defined.
- The model presented is used to investigate the behavior of non-planar fracture propagation during a tip screen-out. This phenomenon highlights how the rock deformation, fluid flow, proppant transport, and fracture propagation directly affect each other and the need for a rigorous coupling methodology.
- A monolithic coupling scheme is shown to be the optimal scheme in comparison to sequential and loose coupling schemes in terms of computational efficiency, robustness, and accuracy.
- An injection-rate controlled simulation is implemented using an iterative loop to solve global mass conservation. A robust algorithm for approximating the slope of the wellbore pressure-injection rate curve is developed to increase the convergence rate of the iterative scheme.

5.3 Directions for future study

Throughout the course of research for this thesis, many ideas for improvement and continuation of the work were uncovered. Possible directions for future work to continue to enhance the field of hydraulic fracturing simulation are summarized below:

Validation: Validation of numerical models remains one of the greatest challenges in hydraulic fracturing simulations. Due to the complex interaction of mechanisms at various scales which are difficult and/or deterrently expensive to replicate in the lab, the uncertainty in field data, and the absence of meaningful measurement tools to analyze field response, there are limited experimental results with which to validate models. Nevertheless, validation is of great importance to ensure the reliability of the model results. Some experimental data exist for laboratory-scale problems without proppant transport which can be used to validate components of the model. Further design and implementation of experimental testing, even at the laboratory scale, is recommended to validate other components of the numerical model presented. Although there are many

components of the model that require validation, of particular interest is proppant transport through a variable-width aperture to study the interaction with proppant build-up and fracture deformation.

Application: The numerical models proposed in this thesis can be used to simulate other scenarios of interest in hydraulic fracturing. The model can be applied to the simulation of a full Tip Screen-Out (TSO) design including flushing of proppant with pure fracturing fluid to clear the proppant pack. Additionally, it can be used to simulate proppant transport in a fracture network to study the pathways proppant is most likely to travel. However, computational tractability remains a challenge since the numerical simulation of a full-scale hydraulic fracturing treatment could take on the order of years to complete with the methodology proposed.

Fracture closure: Various interactions between rock deformation, fluid flow, and proppant transport have been studied in this work. One that remains to be studied is the effect of proppant on the fracture aperture after shut-in as the fracture closes. This interaction is expected to follow a similar numerical form in the constitutive model of the fracture interface as shear dilation. However, determination of the correct closure aperture is a topic for future work.

Unified coupling: The coupled model developed in this thesis incorporates rock deformation, fluid flow, proppant transport, and fracture propagation. A numerical model that also incorporates shear dilation and fracture closure in a fracture network is of interest as it enables a study of permeability enhancement in a hydraulic fracturing treatment. The main challenge with incorporated the physics of shear dilation into the coupled model is the computational difficulties of obtaining a converged solution due to the non-smoothness of the dilation problem. If this challenge can be overcome, the model can be used to perform a sensitivity analysis of the various factors that affect the permeability to enhance the understanding of the principal factors driving the efficacy of the treatment. The study would also require the definition of a measure of effective permeability in the reservoir.

Extension to three dimensions: A two-dimensional model of hydraulic fracturing is a useful tool for exploring the qualitative trends in reservoir behavior. However, the simplification to two dimensions reduces the scope of applicable mechanisms, which affects the accuracy of the simulation results. For instance, fracture growth along the height of the fracture and settling of proppant due to gravity are not captured in a two-dimensional model. An extension of the model to a three-dimensional form would allow for more realistic results.

References

[1] Rivas, E., Parchei-Esfahani, M., and Gracie, R., A two-dimensional extended finite element method model of discrete fracture networks, *International Journal for Numerical Methods in Engineering*, vol. 117, no. 13, pp. 1263–1282, 2019.

[2] Rivas, E. and Gracie, R., Numerical considerations for the simulation of proppant transport through fractures, *Journal of Petroleum Science and Engineering*, 2019.

[3] Rivas, E. and Gracie, R., A monolithic coupled hydraulic fracture model with proppant transport, *Manuscript submitted for publication*, 2020.

[4] Economides, M. J. and Nolte, K. G., *Reservoir stimulation*, 3rd ed. Prentice Hall Englewood Cliffs, NJ, 2000.

[5] Kazemi, A. R., Mahbaz, S. B., Dehghani-Sanij, A. R., Dusseault, M. B., and Fraser, R., Performance Evaluation of an Enhanced Geothermal System in the Western Canada Sedimentary Basin, *Renewable and Sustainable Energy Reviews*, vol. 113, p. 109 278, 2019.

[6] Spence, D. A. and Turcotte, D. L., Magma-driven propagation of cracks, *Journal of Geophysical Research: Solid Earth*, vol. 90, no. B1, pp. 575–580, 1985.

[7] US Department of Energy, *U.S. Dry Natural Gas Production*, 2016.

[8] Dusseault, M., "Hydraulic Fracture Processes in Fractured Carbonates, Shale gas, and Solid waste disposal," Lecture, Waterloo, Ontario, 2015.

[9] Goodman, R. E., *Introduction to Rock Mechanics*, 2nd ed. New York: John Wiley & Sons, 1989.

[10] Mayerhofer, M. J., Lolon, E., Warpinski, N. R., Cipolla, C. L., Walser, D. W., and Rightmire, C. M., What Is Stimulated Reservoir Volume? *SPE Production & Operations*, vol. 25, no. 01, pp. 89–98, 2010.

[11] Khristianovic, S. and Zheltov, Y., Formation of Vertical Fractures by Means of Highly Viscous Liquid, World Petroleum Congress, 1955.

[12] Perkins, T. and Kern, L., Widths of Hydraulic Fractures, *Journal of Petroleum Technology*, vol. 13, no. 09, pp. 937–949, 1961.

[13] Nordgren, R., Propagation of a Vertical Hydraulic Fracture, *Society of Petroleum Engineers*, vol. 12, no. 04, pp. 306–314, 1972.

[14] Sneddon, I. N., The Distribution of Stress in the Neighbourhood of a Crack in an Elastic Solid, *Proceedings of the Royal Society of London A: Mathematical, Physical and Engineering Sciences*, vol. 187, no. 1009, pp. 229–260, 1946.

[15] Adachi, J., Siebrits, E., Peirce, A., and Desroches, J., Computer simulation of hydraulic fractures, *International Journal of Rock Mechanics and Mining Sciences*, vol. 44, no. 5, pp. 739–757, 2007.

[16] Dusseault, M. B., Danyluk, P. G., and Bilak, R. A., Slurry Fracture Injection of Solid and Liquid Heavy Oil Wastes, Society of Petroleum Engineers, 1998.

[17] Goodman, R. E., *Methods of geological engineering in discontinuous rocks*. St. Paul: West Pub. Co, 1976.

[18] Rahman, M. K., Hossain, M. M., and Rahman, S. S., A shear-dilation-based model for evaluation of hydraulically stimulated naturally fractured reservoirs, *International Journal for Numerical and Analytical Methods in Geomechanics*, vol. 26, no. 5, pp. 469–497, 2002.

[19] Barton, N., Bandis, S., and Bakhtar, K., Strength, deformation and conductivity coupling of rock joints, *International Journal of Rock Mechanics and Mining Sciences & Geomechanics Abstracts*, vol. 22, no. 3, pp. 121–140, 1985.

[20] Goldstein, M., Goosev, B., Pvrogovsky, N., Tulinov, R., Turovskaya, A., *et al.*, Investigation of mechanical properties of cracked rock, in *1st ISRM Congress*, International Society for Rock Mechanics, 1966.

[21] Patton, F. D., Multiple Modes of Shear Failure In Rock, International Society for Rock Mechanics, 1966.

[22] Newland, P. L. and Allely, B. H., Volume Changes in Drained Triaxial Tests on Granular Materials, *Géotechnique*, vol. 7, no. 1, pp. 17–34, 1957.

[23] Willis-Richards, J., Watanabe, K., and Takahashi, H., Progress toward a stochastic rock mechanics model of engineered geothermal systems, *Journal of Geophysical Research: Solid Earth*, vol. 101, no. B8, pp. 17 481–17 496, 1996.

[24] Yin, S., Towler, B. F., Dusseault, M. B., and Rothenburg, L., Numerical experiments on oil sands shear dilation and permeability enhancement in a multiphase thermoporoelastoplasticity framework, *Journal of Petroleum Science and Engineering*, vol. 69, no. 3, pp. 219–226, 2009.

[25] Hobbs, B. E. and Ord, A., Numerical simulation of shear band formation in a frictional-dilational material, *Ingenieur-Archiv*, vol. 59, no. 3, pp. 209–220, 1988.

[26] Rutqvist, J., Wu, Y.-S., Tsang, C.-F., and Bodvarsson, G., A modeling approach for analysis of coupled multiphase fluid flow, heat transfer, and deformation in fractured porous rock, *International Journal of Rock Mechanics and Mining Sciences*, Numerical Methods in Rock Mechanics, vol. 39, no. 4, pp. 429–442, 2002.

[27] Koh, J., Roshan, H., and Rahman, S. S., A numerical study on the long term thermo-poroelastic effects of cold water injection into naturally fractured geothermal reservoirs, *Computers and Geotechnics*, vol. 38, no. 5, pp. 669–682, 2011.

[28] Tao, Q., Ghassemi, A., and Ehlig-Economides, C. A., A fully coupled method to model fracture permeability change in naturally fractured reservoirs, *International Journal of Rock Mechanics and Mining Sciences*, vol. 48, no. 2, pp. 259–268, 2011.

[29] Gu, S., Liu, Y., and Chen, Z., Numerical study of dynamic fracture aperture during production of pressure-sensitive reservoirs, *International Journal of Rock Mechanics and Mining Sciences*, vol. 70, pp. 229–239, 2014.

[30] Cundall, P. A. and Strack, O. D. L., A discrete numerical model for granular assemblies, *Géotechnique*, vol. 29, no. 1, pp. 47–65, 1979.

[31] Min, K.-B., Rutqvist, J., Tsang, C.-F., and Jing, L., Stress-dependent permeability of fractured rock masses: A numerical study, *International Journal of Rock Mechanics and Mining Sciences*, vol. 41, no. 7, pp. 1191–1210, 2004.

[32] Bidgoli, M. N., Zhao, Z., and Jing, L., Numerical evaluation of strength and deformability of fractured rocks, *Journal of Rock Mechanics and Geotechnical Engineering*, vol. 5, no. 6, pp. 419–430, 2013.

[33] Belytschko, T. and Black, T., Elastic crack growth in finite elements with minimal remeshing, *International Journal for Numerical Methods in Engineering*, vol. 45, no. 5, pp. 601–620, 1999.

[34] Moës, N., Dolbow, J., and Belytschko, T., A finite element method for crack growth without remeshing, *International Journal for Numerical Methods in Engineering*, vol. 46, no. 1, pp. 131–150, 1999.

[35] Sukumar, N., Moës, N., Moran, B., and Belytschko, T., Extended finite element method for three-dimensional crack modelling, *International Journal for Numerical Methods in Engineering*, vol. 48, no. 11, pp. 1549–1570, 2000.

[36] Duarte, C. A., Hamzeh, O. N., Liszka, T. J., and Tworzydlo, W. W., A generalized finite element method for the simulation of three-dimensional dynamic crack propagation, *Computer Methods in Applied Mechanics and Engineering*, vol. 190, no. 15, pp. 2227–2262, 2001.

[37] Gravouil, A., Moës, N., and Belytschko, T., Non-planar 3D crack growth by the extended finite element and level sets—Part II: Level set update, *International Journal for Numerical Methods in Engineering*, vol. 53, no. 11, pp. 2569–2586, 2002.

[38] Zi, G., Song, J.-H., Budyn, E., Lee, S.-H., and Belytschko, T., A method for growing multiple cracks without remeshing and its application to fatigue crack growth, *Modelling and Simulation in Materials Science and Engineering*, vol. 12, no. 5, p. 901, 2004.

[39] Areias, P. M. A. and Belytschko, T., Analysis of three-dimensional crack initiation and propagation using the extended finite element method, *International Journal for Numerical Methods in Engineering*, vol. 63, no. 5, pp. 760–788, 2005.

[40] Gupta, P. and Duarte, C. A., Simulation of non-planar three-dimensional hydraulic fracture propagation, *International Journal for Numerical and Analytical Methods in Geomechanics*, vol. 38, no. 13, pp. 1397–1430, 2014.

[41] Gupta, P. and Duarte, C. A., Coupled formulation and algorithms for the simulation of non-planar three-dimensional hydraulic fractures using the generalized finite element method, *International Journal for Numerical and Analytical Methods in Geomechanics*, vol. 40, no. 10, pp. 1402–1437, 2016.

[42] Remij, E. W., Fluid driven and mechanically induced fracture propagation: Theory and numerical simulations, 2017.

[43] Karihaloo, B. L. and Xiao, Q. Z., Modelling of stationary and growing cracks in FE framework without remeshing: A state-of-the-art review, *Computers & Structures*, vol. 81, no. 3, pp. 119–129, 2003.

[44] Abdelaziz, Y. and Hamouine, A., A survey of the extended finite element, *Computers & Structures*, vol. 86, no. 11-12, pp. 1141–1151, 2008.

[45] Mohammadi, S., *Extended Finite Element Method: for Fracture Analysis of Structures*. John Wiley & Sons, 2008.

[46] Belytschko, T., Gracie, R., and Ventura, G., A review of extended/generalized finite element methods for material modeling, *Modelling and Simulation in Materials Science and Engineering*, vol. 17, no. 4, 2009.

[47] Rabczuk, T., Bordas, S., and Zi, G., On three-dimensional modelling of crack growth using partition of unity methods, *Computers & structures*, vol. 88, no. 23, pp. 1391–1411, 2010.

[48] Fries, T.-P. and Belytschko, T., The extended/generalized finite element method: An overview of the method and its applications, *International Journal for Numerical Methods in Engineering*, vol. 84, no. 3, pp. 253–304, 2010.

[49] Khoei, A. R., *Extended Finite Element Method: Theory and Applications*. Chichester, UK: John Wiley & Sons, Ltd, 2014.

[50] Dolbow, J., Moës, N., and Belytschko, T., Discontinuous enrichment in finite elements with a partition of unity method, *Finite Elements in Analysis and Design*, vol. 36, no. 3–4, pp. 235–260, 2000.

[51] Fries, T.-P. and Baydoun, M., Crack propagation with the extended finite element method and a hybrid explicit–implicit crack description, *International Journal for Numerical Methods in Engineering*, vol. 89, no. 12, pp. 1527–1558, 2012.

[52] Moës, N. and Belytschko, T., Extended finite element method for cohesive crack growth, *Engineering Fracture Mechanics*, vol. 69, no. 7, pp. 813–833, 2002.

[53] Réthoré, J., Borst, R. de, and Abellan, M.-A., A discrete model for the dynamic propagation of shear bands in a fluid-saturated medium, *International Journal for Numerical and Analytical Methods in Geomechanics*, vol. 31, no. 2, pp. 347–370, 2007.

[54] Areias, P. M. A. and Belytschko, T., Two-scale shear band evolution by local partition of unity, *International Journal for Numerical Methods in Engineering*, vol. 66, no. 5, pp. 878–910, 2006, _eprint: https://onlinelibrary.wiley.com/doi/pdf/10.1002/nme.1589.

[55] Samaniego, E. and Belytschko, T., Continuum–discontinuum modelling of shear bands, *International Journal for Numerical Methods in Engineering*, vol. 62, no. 13, pp. 1857–1872, 2005, _eprint: https://onlinelibrary.wiley.com/doi/pdf/10.1002/nme.1256.

[56] Song, J.-H., Areias, P. M. A., and Belytschko, T., A method for dynamic crack and shear band propagation with phantom nodes, *International Journal for Numerical Methods in Engineering*, vol. 67, no. 6, pp. 868–893, 2006.

[57] Dolbow, J., Moës, N., and Belytschko, T., An extended finite element method for modeling crack growth with frictional contact, *Computer Methods in Applied Mechanics and Engineering*, vol. 190, no. 51–52, pp. 6825–6846, 2001.

[58] Liu, F. and Borja, R. I., A contact algorithm for frictional crack propagation with the extended finite element method, *International Journal for Numerical Methods in Engineering*, vol. 76, no. 10, pp. 1489–1512, 2008.

[59] Elguedj, T., Gravouil, A., and Combescure, A., A mixed augmented Lagrangian-extended finite element method for modelling elastic–plastic fatigue crack growth with unilateral contact, *International Journal for Numerical Methods in Engineering*, vol. 71, no. 13, pp. 1569–1597, 2007.

[60] Hirmand, M., Vahab, M., and Khoei, A. R., An augmented Lagrangian contact formulation for frictional discontinuities with the extended finite element method, *Finite Elements in Analysis and Design*, vol. 107, pp. 28–43, 2015.

[61] Sanders, J. D., Dolbow, J. E., and Laursen, T. A., On methods for stabilizing constraints over enriched interfaces in elasticity, *International Journal for Numerical Methods in Engineering*, vol. 78, no. 9, pp. 1009–1036, 2009.

[62] Smith, M. B. and Montgomery, C., *Hydraulic Fracturing*. Boca Raton: CRC Press, 2015.

[63] Detournay, E., Mechanics of Hydraulic Fractures, *Annual Review of Fluid Mechanics*, vol. 48, no. 1, pp. 311–339, 2016.

[64] Hattori, G., Trevelyan, J., Augarde, C. E., Coombs, W. M., and Aplin, A. C., Numerical Simulation of Fracking in Shale Rocks: Current State and Future Approaches, *Archives of Computational Methods in Engineering*, 2016.

[65] Lecampion, B., Bunger, A., and Zhang, X., Numerical methods for hydraulic fracture propagation: A review of recent trends, *Journal of Natural Gas Science and Engineering*, vol. 49, pp. 66–83, 2018.

[66] Osiptsov, A. A., Fluid mechanics of hydraulic fracturing: A review, *Journal of Petroleum Science and Engineering*, 2017.

[67] Novotny, E., Proppant Transport, in *SPE Annual Fall Technical Conference and Exhibition*, Denver, Colorado: Society of Petroleum Engineers, 1977.

[68] Daneshy, A., Numerical Solution of Sand Transport in Hydraulic Fracturing, *Journal of Petroleum Technology*, vol. 30, no. 01, pp. 132–140, 1978.

[69] Gadde, P. B., Liu, Y., Norman, J., Bonnecaze, R., and Sharma, M. M., Modeling Proppant Settling in Water-Fracs, Society of Petroleum Engineers, 2004.

[70] Zhou, L., Hou, M. Z., Gou, Y., and Li, M., Numerical investigation of a low-efficient hydraulic fracturing operation in a tight gas reservoir in the North German Basin, *Journal of Petroleum Science and Engineering*, vol. 120, pp. 119–129, 2014.

[71] Shiozawa, S. and McClure, M., Simulation of proppant transport with gravitational settling and fracture closure in a three-dimensional hydraulic fracturing simulator, *Journal of Petroleum Science and Engineering*, vol. 138, pp. 298–314, 2016.

[72] Vahab, M. and Khalili, N., An X-FEM Formulation for the Optimized Graded Proppant Injection into Hydro-fractures Within Saturated Porous Media, *Transport in Porous Media*, vol. 121, no. 2, pp. 289–314, 2018.

[73] Dontsov, E. V. and Peirce, A. P., Slurry flow, gravitational settling and a proppant transport model for hydraulic fractures, *Journal of Fluid Mechanics*, vol. 760, pp. 567–590, 2014.

[74] Boronin, S. A. and Osiptsov, A. A., Effects of particle migration on suspension flow in a hydraulic fracture, *Fluid Dynamics*, vol. 49, no. 2, pp. 208–221, 2014.

[75] Dontsov, E. V. and Peirce, A. P., Proppant transport in hydraulic fracturing: Crack tip screen-out in KGD and P3D models, *International Journal of Solids and Structures*, vol. 63, pp. 206–218, 2015.

[76] Detournay, C., Lemos, J., and Zhang, F., Development of a proppant transport logic in 3DEC, *Applied Numerical Modeling in Geomechanics*, p. 13, 2016.

[77] Roostaei, M., Nouri, A., Fattahpour, V., and Chan, D., Numerical simulation of proppant transport in hydraulic fractures, *Journal of Petroleum Science and Engineering*, vol. 163, pp. 119–138, 2018.

[78] Kong, B., Fathi, E., and Ameri, S., Coupled 3-D numerical simulation of proppant distribution and hydraulic fracturing performance optimization in Marcellus shale reservoirs, *International Journal of Coal Geology*, vol. 147–148, pp. 35–45, 2015.

[79] Dontsov, E. V. and Peirce, A. P., A Lagrangian Approach to Modelling Proppant Transport with Tip Screen-Out in KGD Hydraulic Fractures, *Rock Mechanics and Rock Engineering*, vol. 48, no. 6, pp. 2541–2550, 2015.

[80] Varadarajan, P. A. and Hammond, P., Numerical scheme for accurately capturing gas migration described by 1D multiphase drift flux model, *International Journal of Multiphase Flow*, vol. 73, pp. 57–70, 2015.

[81] Lorentzen, R. J. and Fjelde, K. K., Use of slopelimiter techniques in traditional numerical methods for multi-phase flow in pipelines and wells, *International Journal for Numerical Methods in Fluids*, vol. 48, no. 7, pp. 723–745, 2005.

[82] Smith, M., Miller, W., and Haga, J., Tip Screenout Fracturing: A Technique for Soft, Unstable Formations, *SPE Production Engineering*, vol. 2, no. 02, pp. 95–103, 1987.

[83] Shi, F., Wang, X., Liu, C., Liu, H., and Wu, H., A coupled extended finite element approach for modeling hydraulic fracturing in consideration of proppant, *Journal of Natural Gas Science and Engineering*, vol. 33, pp. 885–897, 2016.

[84] Zienkiewicz, O. C. and Chan, A. H. C., "Coupled Problems and Their Numerical Solution," in *Advances in Computational Nonlinear Mechanics*, ser. International Centre for Mechanical Sciences, Springer, Vienna, 1989, pp. 139–176.

[85] Gordeliy, E. and Peirce, A., Coupling schemes for modeling hydraulic fracture propagation using the XFEM, *Computer Methods in Applied Mechanics and Engineering*, vol. 253, pp. 305–322, 2013.

[86] Parchei Esfahani, M. and Gracie, R., On the undrained and drained hydraulic fracture splits, *International Journal for Numerical Methods in Engineering*, 2019.

[87] Lecampion, B., An extended finite element method for hydraulic fracture problems, *Communications in Numerical Methods in Engineering*, vol. 25, no. 2, pp. 121–133, 2009.

[88] Gordeliy, E. and Peirce, A., Implicit level set schemes for modeling hydraulic fractures using the XFEM, *Computer Methods in Applied Mechanics and Engineering*, vol. 266, pp. 125–143, 2013.

[89] Wang, H., Numerical modeling of non-planar hydraulic fracture propagation in brittle and ductile rocks using XFEM with cohesive zone method, *Journal of Petroleum Science and Engineering*, vol. 135, pp. 127–140, 2015.

[90] Wriggers, P., *Computational Contact Mechanics*, 2nd ed. Berlin, Heidelberg: Springer Berlin Heidelberg, 2006.

[91] Nour-Omid, B. and Wriggers, P., A note on the optimum choice for penalty parameters, *Communications in Applied Numerical Methods*, vol. 3, no. 6, pp. 581–585, 1987.

[92] Hallquist, J. O., "LS-Dyna3D Theoretical Manual," Livermore, CA, Tech. Rep. 1018, 2006.

[93] Geubelle, P. H. and Baylor, J. S., Impact-induced delamination of composites: A 2D simulation, *Composites Part B: Engineering*, vol. 29, no. 5, pp. 589–602, 1998.

[94] Ladanyi, B. and Archambault, G., Simulation Of Shear Behavior Of A Jointed Rock Mass, American Rock Mechanics Association, 1969.

[95] Watanabe, K. and Takahashi, H., Fractal geometry characterization of geothermal reservoir fracture networks, *Journal of Geophysical Research: Solid Earth*, vol. 100, no. B1, pp. 521–528, 1995.

[96] Jing, Z., Willis-Richards, J., Watanabe, K., and Hashida, T., A three-dimensional stochastic rock mechanics model of engineered geothermal systems in fractured crystalline rock, *Journal of Geophysical Research: Solid Earth*, vol. 105, no. B10, pp. 23 663–23 679, 2000.

[97] Daux, C., Moës, N., Dolbow, J., Sukumar, N., and Belytschko, T., Arbitrary branched and intersecting cracks with the extended finite element method, *International Journal for Numerical Methods in Engineering*, vol. 48, no. 12, pp. 1741–1760, 2000.

[98] Belytschko, T., Liu, W. K., Moran, B., and Elkhodary, K., "Chapter 11: Extended Finite Element Method (XFEM)," in *Nonlinear Finite Elements for Continua and Structures*, John Wiley & Sons, 2014.

[99] Oakley, D. R. and Knight, N. F., Adaptive dynamic relaxation algorithm for non-linear hyperelastic structures Part I. Formulation, *Computer Methods in Applied Mechanics and Engineering*, vol. 126, no. 1, pp. 67–89, 1995.

[100] Sauve, R. and Metzger, D., Advances in Dynamic Relaxation Techniques for Nonlinear Finite Element Analysis, *Journal of Pressure Vessel Technology*, vol. 117, no. 2, pp. 170–176, 1995.

[101] Hammond, P. S., Settling and slumping in a Newtonian slurry, and implications for proppant placement during hydraulic fracturing of gas wells, *Chemical Engineering Science*, vol. 50, no. 20, pp. 3247–3260, 1995.

[102] Einstein, A., Eine neue Bestimmung der Moleküldimensionen, *Annalen der Physik*, vol. 324, no. 2, pp. 289–306, 1906.

[103] Stickel, J. J. and Powell, R. L., Fluid Mechanics and Rheology of Dense Suspensions, *Annual Review of Fluid Mechanics*, vol. 37, no. 1, pp. 129–149, 2005.

[104] Clifton, R. and Wang, J.-J., Multiple Fluids, Proppant Transport, and Thermal Effects in Three-Dimensional Simulation of Hydraulic Fracturing, Society of Petroleum Engineers, 1988.

[105] Mueller, S., Llewellin, E. W., and Mader, H. M., The rheology of suspensions of solid particles, *Proceedings of the Royal Society A: Mathematical, Physical and Engineering Sciences*, vol. 466, no. 2116, pp. 1201–1228, 2010.

[106] Batchelor, G. K., The effect of Brownian motion on the bulk stress in a suspension of spherical particles, *Journal of Fluid Mechanics*, vol. 83, no. 01, p. 97, 1977.

[107] Eskin, D. and Miller, M. J., A model of non-Newtonian slurry flow in a fracture, *Powder Technology*, vol. 182, no. 2, pp. 313–322, 2008.

[108] Eilers, H., Die Viskosität von Emulsionen hochviskoser Stoffe als Funktion der Konzentration, *Kolloid-Zeitschrift*, vol. 97, no. 3, pp. 313–321, 1941.

[109] Krieger, I. M. and Dougherty, T. J., A Mechanism for Non-Newtonian Flow in Suspensions of Rigid Spheres, *Transactions of the Society of Rheology*, vol. 3, no. 1, pp. 137–152, 1959.

[110] Thomas, D. G., Transport characteristics of suspension: VIII. A note on the viscosity of Newtonian suspensions of uniform spherical particles, *Journal of Colloid Science*, vol. 20, no. 3, pp. 267–277, 1965.

[111] Nicodemo, L., Nicolais, L., and Landel, R., Shear rate dependent viscosity of suspensions in newtonian and non-newtonian liquids, *Chemical Engineering Science*, vol. 29, no. 3, pp. 729–735, 1974.

[112] Maron, S. H. and Pierce, P. E., Application of Ree-eyring Generalized Flow Theory to Suspensions of Spherical Particles, *Journal of Colloid Science*, vol. 11, pp. 80–95, 1956.

[113] Barree, R. and Conway, M., Experimental and Numerical Modeling of Convective Proppant Transport, Society of Petroleum Engineers, 1995.

[114] Krieger, I. M., Rheology of monodisperse latices, *Advances in Colloid and Interface Science*, vol. 3, no. 2, pp. 111–136, 1972.

[115] Scott, K. J., *Hindered settling of a suspension of spheres: critical evaluation of equations relating settling rate to mean particle diamter and suspension concentration*. Pretoria: Chemical Engineering Research Group, CSIR, 1984, OCLC: 254046774.

[116] Garagash, I., Osiptsov, A., and Boronin, S., Dynamic bridging of proppant particles in a hydraulic fracture, *International Journal of Engineering Science*, vol. 135, pp. 86–101, 2019.

[117] LeVeque, R. J., *Finite Volume Methods for Hyperbolic Problems*. Cambridge: Cambridge University Press, 2002.

[118] Bale, D. S., LeVeque, R. J., Mitran, S., and Rossmanith, J. A., A Wave Propagation Method for Conservation Laws and Balance Laws with Spatially Varying Flux Functions, *SIAM Journal on Scientific Computing*, vol. 24, no. 3, pp. 955–978, 2003.

[119] Dontsov, E. V., An approximate solution for a plane strain hydraulic fracture that accounts for fracture toughness, fluid viscosity, and leak-off, *International Journal of Fracture*, vol. 205, no. 2, pp. 221–237, 2017.

[120] Mohammadnejad, T. and Khoei, A. R., An extended finite element method for hydraulic fracture propagation in deformable porous media with the cohesive crack model, *Finite Elements in Analysis and Design*, vol. 73, pp. 77–95, 2013.

[121] Gracie, R. and Parchei Esfahani, M., Hydraulic Fracture Simulation - Coupling Strategies and Pressure Pulsing, in *VI International Conference on Computational Modeling of Fracture and Failure of Materials and Structures*, Braunschweig, Germany, 2019.

[122] Khoei, A. R., Hirmand, M., Vahab, M., and Bazargan, M., An enriched FEM technique for modeling hydraulically driven cohesive fracture propagation in impermeable media with frictional natural faults: Numerical and experimental investigations, *International Journal for Numerical Methods in Engineering*, vol. 104, no. 6, pp. 439–468, 2015.

[123] Parchei Esfahani, M., Advances in Hydraulic Fracture Simulation - Dynamic and Quasi-static Analysis, Doctoral dissertation, University of Waterloo, Waterloo, Ontario, 2019.

[124] Belytschko, T., Liu, W. K., Moran, B., and Elkhodary, K., *Nonlinear Finite Elements for Continua and Structures*. John Wiley & Sons, 2000.

[125] Park, K. and Paulino, G. H., Cohesive Zone Models: A Critical Review of Traction-Separation Relationships Across Fracture Surfaces, *Applied Mechanics Reviews*, vol. 64, no. 6, p. 060 802, 2013.

[126] Howard, G. C. and Fast, C. R., Optimum Fluid Characteristics for Fracture Extension, American Petroleum Institute, 1957.

[127] Carman, P., Fluid flow through granular beds, *Chemical Engineering Research and Design*, vol. 75, S32–S48, 1997.

[128] Kozeny, J., *Über kapillare Leitung des Wassers im Boden: (Aufstieg, Versickerung u. Anwendung auf die Bewässerg) ; Gedr. mit Unterstützg aus d. Jerome u. Margaret Stonborsugh-Fonds*. Hölder-Pichler-Tempsky, 1927.

[129] Hu, J. and Garagash, D. I., Plane-Strain Propagation of a Fluid-Driven Crack in a Permeable Rock with Fracture Toughness, *Journal of Engineering Mechanics*, vol. 136, no. 9, pp. 1152–1166, 2010.

[130] Bunger, A. P., Detournay, E., and Garagash, D. I., Toughness-dominated Hydraulic Fracture with Leak-off, *International Journal of Fracture*, vol. 134, no. 2, pp. 175–190, 2005.

[131] Adachi, J. I. and Detournay, E., Plane strain propagation of a hydraulic fracture in a permeable rock, *Engineering Fracture Mechanics*, vol. 75, no. 16, pp. 4666–4694, 2008.

[132] Barenblatt, G. I., The formation of equilibrium cracks during brittle fracture. General ideas and hypotheses. Axially-symmetric cracks, *Journal of Applied Mathematics and Mechanics*, vol. 23, no. 3, pp. 622–636, 1959.

[133] Dugdale, D. S., Yielding of steel sheets containing slits, *Journal of the Mechanics and Physics of Solids*, vol. 8, no. 2, pp. 100–104, 1960.

[134] Erdogan, F. and Sih, G. C., On the Crack Extension in Plates Under Plane Loading and Transverse Shear, *Journal of Basic Engineering*, vol. 85, no. 4, pp. 519–525, 1963.

[135] Mogilevskaya, S., Rothenburg, L., and Dusseault, M., Growth of Pressure-Induced Fractures in the Vicinity of a Wellbore, *International Journal of Fracture*, vol. 104, no. 4, pp. 23–30, 2000.

[136] Zhang, X., Jeffrey, R. G., Bunger, A. P., and Thiercelin, M., Initiation and growth of a hydraulic fracture from a circular wellbore, *International Journal of Rock Mechanics and Mining Sciences*, vol. 48, no. 6, pp. 984–995, 2011.

[137] Gee, B., Parchei-Esfahani, M., and Gracie, R., XFEM simulation of a mixed-mode fracture experiment in PMMA, *Engineering Fracture Mechanics*, vol. 229, p. 106 945, 2020.

[138] Rivas, E. and Gracie, R., Shear Dilation Using the Extended Finite Element Method, in *24th International Congress of Theoretical and Applied Mechanics*, Montreal, Canada, 2016.

[139] Rivas, E. and Gracie, R., An Extended Finite Element Model for Studying Shear Dilation in a Pressurized Medium, in *14th U.S. National Congress on Computational Mechanics*, Montreal, Canada, 2017.

Appendices

Appendix A

Verification of planar fracture propagation

In this section, the propagation of planar fractures is verified by comparing the numerical results with analytical solutions. First, two examples of hydraulic fractures propagated with a pure fracturing fluid (no proppant) are provided. The material properties and injection rates are selected such that the fracture lies in two asymptotic tip conditions: toughness-dominated regime and viscosity-dominated regime. In the third example, a proppant-laden slurry is injected into a propagating planar fracture. The proppant concentration along the fracture length is compared to the results by Shi *et al.* [83]. The importance of a conservative form of the proppant advection equation id demonstrated in this example.

Half of the physical domain is modeled in each of the examples provided by taking advantage of the symmetry so that only half of the fracture is simulated. The material properties that are common to all simulations in this section are provided in Table 4.1. These values are representative of water-based fracturing fluid with a sand-based proppant injected into a shale reservoir. The material properties selected for each of these examples are listed in Table A.1.

A 20 m by 40 m domain is simulated, with an initial horizontal fracture of 20 cm length located at the centerline of the fracture, as shown in Figure A.1. The mesh used to discretize the solid

Table A.1: Material properties for planar fracture propagation simulations

	Toughness-dominated Section A.1	Viscosity-dominated Section A.2	Slurry-driven Section A.3
Yield Strength, f_u	5 MPa	3 MPa	1.25 MPa
Fracture Energy, G_{Ic}	1000 J/m^2	0.5 J/m^2	0.48 J/m^2
Fluid Viscosity, μ	0.001 Pa·s	1 Pa·s	0.1 Pa·s
Carter Leak-off Coefficient, c_L	0 m/$\sqrt{\text{s}}$	0 m/$\sqrt{\text{s}}$	1×10^{-5} m/$\sqrt{\text{s}}$

rock domain in all three examples is the same as the mesh used in Section 4.5.1. The initial fracture is discretized by four fluid elements and four proppant elements. In all cases, an *in-situ* compression stress of 10 MPa is applied in the horizontal direction and the fluid is injected at a rate of 0.001 m^2/s.

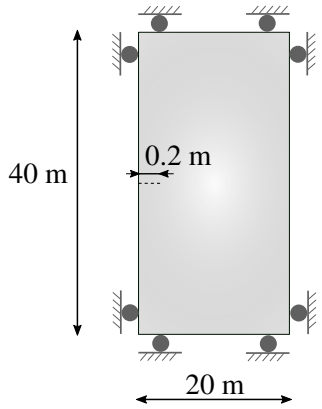

Figure A.1: Schematic of domain for model of planar fracture propagation

A.1 Toughness-dominated planar fracture propagation

Curves showing the wellbore aperture, w_0, wellbore pressure, p_w, and fracture half-length, L, over time for a fracture under toughness-dominated tip conditions are plotted in Figure A.2. The results are compared to analytical solutions by Bunger *et al.* [130], which are plotted with a dashed line. The numerical results match the analytical solutions well, as can be seen by visual comparison of the plots in Figure A.2.

The wellbore aperture and fracture half-length increase over time in a nonlinear form, as expected. The wellbore pressure decreases drastically at the beginning of the simulation and has a shallower decreasing slope for the rest of the simulation. Two fracture half-lengths are plotted, one for the fictitious tip at the end of the fracture process zone and one for the real-tip at the location of fracture opening. The two tip locations are depicted in Figure 4.11a. A material with higher tensile strength would exhibit a smaller cohesive zone, represented by a curve for the fictitious tip that is closer to the curve for the real tip. The analytical solutions are based on Linear Elastic Fracture Mechanics (LEFM), which does not consider a fracture process zone at the tip of the fracture. The LEFM fracture tip lies somewhere between the real tip and fictitious tip plotted in Figure A.2c, but the exact location is unknown.

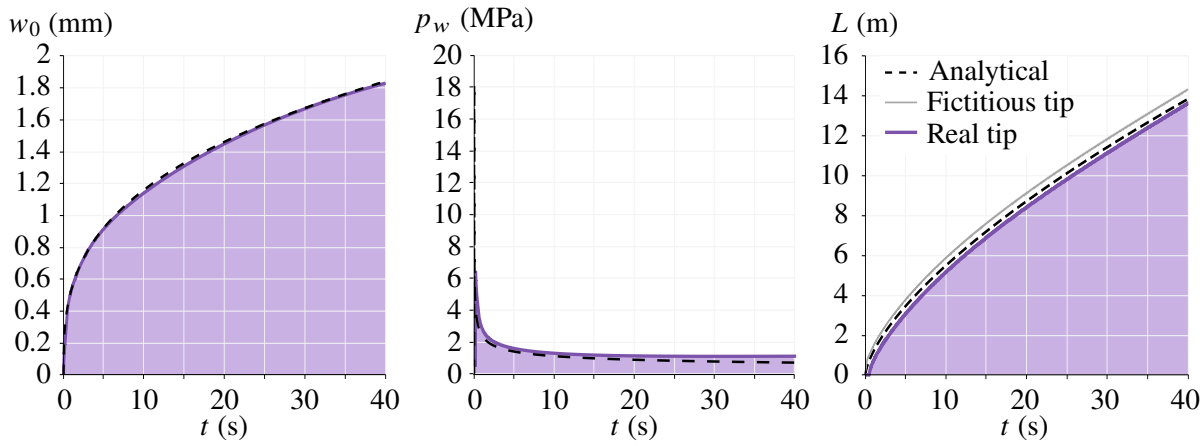

(a) Wellbore aperture (b) Wellbore pressure (c) Fracture half-length

Figure A.2: Wellbore aperture, wellbore pressure, and fracture half-length over time for a fracture propagating in the toughness-dominated regime. Numerical results are shown with solid lines and analytical results with dashed lines

A.2 Viscosity-dominated planar fracture propagation

For a fracture under viscosity-dominated tip conditions, the curves showing the wellbore aperture, wellbore pressure, and fracture half-length over time are plotted in Figure A.3. The analytical solutions derived by Adachi and Detournay [131] are plotted with a dashed line on the figures for comparison. The numerical results match the analytical results well. The differences between the numerical and analytical solutions may be attributed to the finite fracture toughness since the analytical solutions are derived under the assumption of zero toughness. The fracture energy in the numerical results is 0.5 J/m^2, which is equivalent to a fracture toughness of 0.1 MPa through Irwin's relationship under plane strain conditions, $G_{Ic} = K_{IC}^2(1-\nu^2)/E$.

A.3 Slurry-driven planar fracture propagation

The simulation of a planar fracture driven by an injected proppant-laden slurry is discussed in this section. The proppant concentration of the injected slurry increases from 0.1 to 0.4 over a span of 30 seconds, as shown in Figure A.4, with the proppant injection beginning at $t = 10$ s.

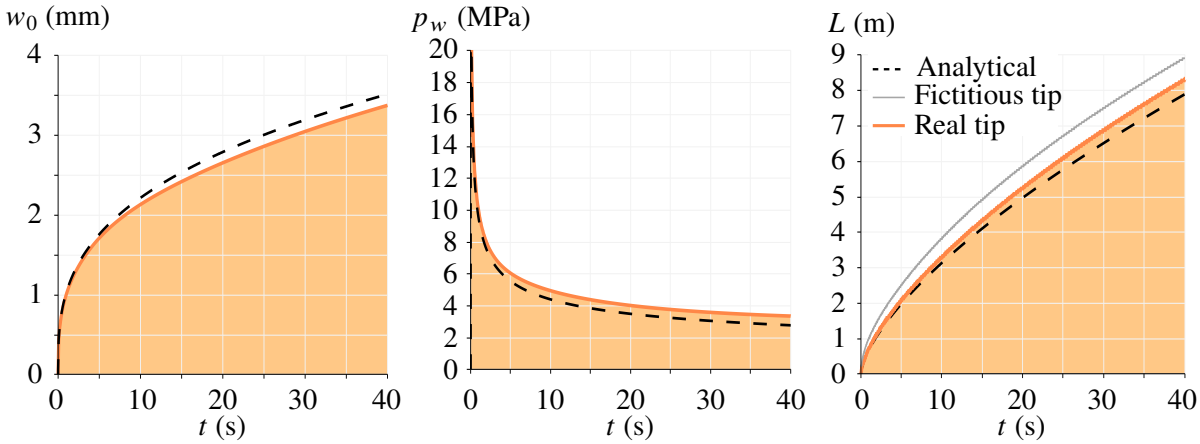

(a) Wellbore aperture (b) Wellbore pressure (c) Fracture half-length

Figure A.3: Wellbore aperture, wellbore pressure, and fracture half-length over time for a fracture propagating in the viscosity-dominated regime. Numerical results are shown with solid lines and analytical results with dashed lines

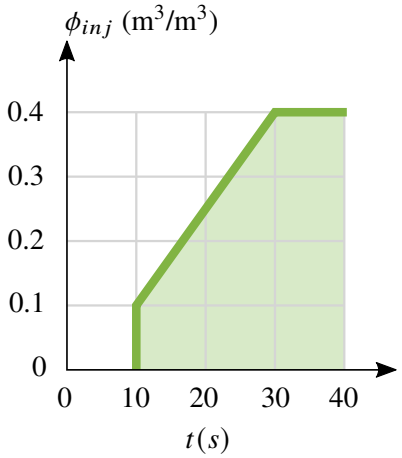

Figure A.4: Proppant concentration of injected slurry over time

A plot of the proppant concentration along the length of the fracture is provided in Figure A.5 for times t = 12.7, 23.8, and 39.5 seconds. The proppant concentration at the injection point (s = 0) is equal to the injected proppant concentration shown in Figure A.4 for the given times. The clearly defined proppant front moves towards the right of the domain over time. The curve of the proppant concentration profile has a section that is linearly increasing (from the fracture tip to inlet of the fracture), which is due to the linearly increasing injection concentration.

The numerical results are compared with the results given by Shi *et al.* [83], shown in Figure A.5

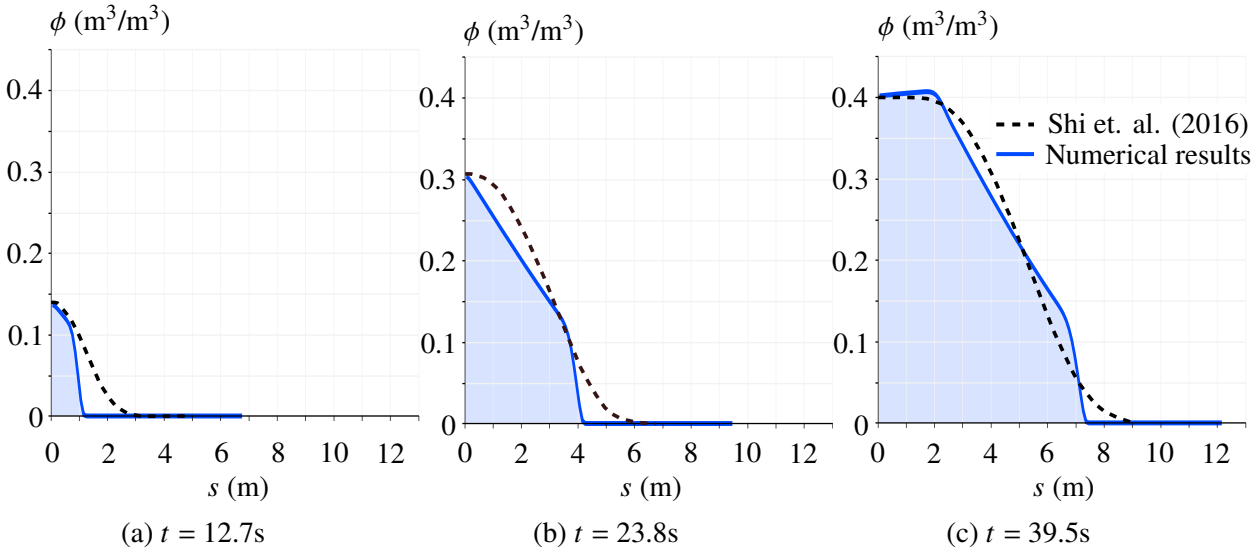

(a) t = 12.7s (b) t = 23.8s (c) t = 39.5s

Figure A.5: Proppant concentration along the fracture for t = 12.7 s, 23.8 s, and 39.5 s. Numerical results in solid lines, and results from Shi *et al.* [83] in dashed lines

with a dashed line. In the work by Shi *et al.* [83], the proppant concentration is calculated at the end of each time step as an update after the solution of the fracture width and fluid pressure have converged. In their work, a non-conservative form of the advection equation is presented which uses the slurry velocity from the converged solution in the time step, in the form $\phi_{,t} + v\phi_{,s} = 0$. The solution of a non-conservative advection equation does not converge to a weak solution of the conservation law when there is a shock in the solution [117], such as the one represented by the proppant front in this example. The approximations in the work by Shi *et al.* [83] lead to a diffused concentration curve with a proppant front that is not well defined. The concentration at the injection point is correctly computed in their model, but the jump in concentration at the proppant front due to an initial injection concentration of 0.1 is not visible. The incorrect approximation of the proppant front could lead, for example, to a premature tip screen-out in a narrow fracture. This example shows the importance of using a conservative form of the proppant advection equation in obtaining a converged solution.

The wellbore aperture, wellbore pressure, and half-length of the fracture are plotted in Figure A.6. The results are compared to a fracture with the same material properties driven by a fluid with no proppant, shown in the figure with a dashed line. The slurry-driven fracture is shorter and wider than the fluid-driven fracture. The proppant concentration leads to a slurry with higher effective viscosity and consequently higher fluid pressure. The differences in the two models are more pronounced at later times in the simulation, as the proppant has spread through the fracture.

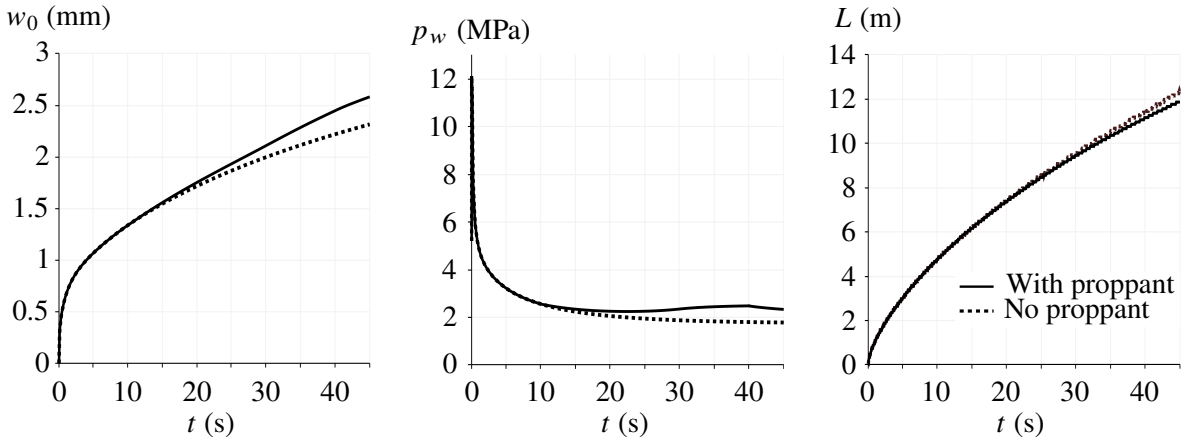

(a) Wellbore aperture (b) Wellbore pressure (c) Fracture half-length

Figure A.6: Wellbore aperture, wellbore pressure, and fracture half-length for planar fracture propagation driven by a proppant-laden slurry (solid) and by pure fracturing fluid (dashed)